Volume 93, Number 1, January–February 1988
Journal of Research of the National Bureau of Standards

In This Issue:

Departments

News Briefs and Reports

Conferences/Events

Volume 93, Number 1, January–February 1988
Journal of Research of the National Bureau of Standards

Articles

Volume 93, Number 1, January–February 1988
Journal of Research of the National Bureau of Standards

News Briefs and Reports

Developments

GROUND BROKEN FOR NBS COLD NEUTRON RESEARCH FACILITY

Ground was broken at NBS on November 20 for the construction of one of the few cold neutron research facilities in the world. The new laboratory will make cold neutron research easily available to U.S. scientists working in such fields as materials science, chemistry, and biology.

Typical areas of application include the design of high-temperature, high-strength ceramics for engines; the study of improved semiconductor devices; the development of new magnetic alloys for more efficient electric motors; the creation of new chemical catalysts; and the precise measurement of newly engineered biomolecules.

The $25-million facility will be housed in a specially designed research hall to be built at the NBS research nuclear reactor. A recently installed "cold source" supplies the low-energy neutrons.

Initial instrumentation will include: a high-resolution small-angle neutron scattering (SANS) spectrometer, one of the fundamental tools of neutron analysis, and an instrument which will rank with the best of its kind in the world; the best neutron depth-profiling instrument in the world; and two temporary facilities, a second SANS instrument and time-of-flight spectrometer. Ultimately, the center will include 15 experimental stations; 10 will be instrumented and operated by NBS and five will be instrumented and operated by outside groups.

These outside groups, Participating Research Teams (PRTs), will come from industrial, academic, or government research institutions and will fully instrument and maintain their stations in return for exclusive use of two-thirds of the available research time. The high-resolution SANS spectrometer is being constructed by a PRT consisting of NBS and Exxon Research and Engineering.

An external advisory committee will be set up to handle the allocation of research time, which will be made available to all U.S. users. The first experimental stations should become available late in 1989.

For further information, contact Michael Rowe at the National Bureau of Standards, Gaithersburg, MD 20899.

DETAILS NOW AVAILABLE ON SUPERCONDUCTING CONTACTS

The high resistance that usually occurs where external leads are attached to ceramic superconductors is an obstacle to both measurements and practical applications of the newly developed high-critical-temperature superconductors. Work by NBS and the Westinghouse Research and Development Center, Pittsburgh, Pennsylvania, has produced a new method for making low-resistance electrical contacts on ceramic superconductors.

The researchers developed the new method after noticing that there was a correlation between the ages of many superconductor samples and their contact resistivities. The new method involves three parts, which work together to produce low contact resistivity: minimizing the air exposure time minimizes the degradation of the superconductor surface that occurs before making the contacts; sputter etching the surface removes the degraded layer; and depositing a thin layer of a noble metal—silver and gold were used—protects the surface and minimizes further degradation of the superconductor surface.

When the method was tried on old samples exposed to air for over 2 months, the contact resistivity was about 10 times higher than that for

contacts formed on fresh samples only an hour old. A deeper sputter etch may be necessary for superconductors having long exposure to air.

For the particular superconductor tested, bulk $YBa_2Cu_3O_7$, the sample was etched to a depth of 20 to 50 nanometers at 1.25 kV rms in 3-Pa argon for about 3 minutes. A 1- to 6-micrometer-thick contact pad was immediately sputtered onto the surface (4.2 kV rms, no applied bias), also under an argon atmosphere. The superconductor temperature was held to less than 100 °C with a water-cooled sample holder.

For further information, contact: Jack Ekin, Electromagnetic Technology Division, National Bureau of Standards, Boulder, CO 80303, or call 303/497-5448.

NBS TESTIFIES ON SUPERCONDUCTIVITY LEGISLATION

On October 7, NBS Deputy Director Raymond Kammer testified before a joint meeting of two House subcommittees considering pending legislation on high-temperature superconductivity research.

Noting that much of the nation's expertise in superconductivity research lies in the national laboratories like NBS, Kammer said, "It is our belief that these technical resources and those of other federal laboratories should be made available to our private industry without exerting the degree of government control that appears to be typical in many other nations." Kammer opposed the creation of additional levels of management to oversee the government's superconductivity research.

NEW ACOUSTIC TECHNIQUE PROMISES BETTER WAY TO EVALUATE INSTALLATION OF HOME THERMAL INSULATION

NBS researchers are completing testing of a new measurement technique, based on acoustics, that shows considerable promise for quality control in the manufacture of insulation and could also be the basis for efficient, low-cost tools for evaluating loose-fill attic insulation after it is installed.

NBS researchers—funded by the Mineral Insulation Manufacturers Association, the U.S. Department of Energy, and NBS—have developed a high-speed method for indirectly measuring either the coverage or the R-value of certain types of loose-fill insulation by passing sound waves through a sample of material and measuring the sound insertion loss (i.e., the decrease in sound level) caused by the insulation at various frequencies.

In the laboratory system developed at NBS, pulses of sound containing energy in the frequency range of 2.5 to 25 kilohertz are projected through a sample of insulating material. The samples of insulation are contained in individual baskets which have acoustically transparent bottoms and are supported inside a specially designed test chamber.

The sound insertion loss of loose-fill insulations has been found, for a given insulating material, to correlate quite well with the coverage (mass per unit area) of the material, particularly for fiberglass materials. Predicting coverage of rock wool insulation is somewhat problematic, according to researchers, because of the presence of fused material (shot).

Researchers say that a version of the laboratory apparatus used at NBS could be useful to insulation manufacturers for quality control. The acoustic test apparatus collects and analyzes data in a few minutes and yields results that would require several hours to obtain using thermal measurement procedures. Moreover, they say, the principles could be applied to field instrumentation for characterizing insulation installed in attics by using acoustic probes either suspended over the insulation, or inserted into the insulation through holes bored in the ceiling. Two NBS researchers, Gerald V. Blessing and Daniel R. Flynn, recently were granted a patent for various design concepts for a field instrument utilizing these ideas.

The results of the NBS experiments have been presented to ASTM Committee C16 on Thermal Insulation, which is interested in the acoustic technique as a possible ASTM test method. In addition, ASTM has agreed to coordinate an effort to raise the funds needed to develop a practical field instrument based on acoustic measurements of installed loose-fill insulation.

For further information, contact Gerald Blessing, A147 Sound Building, National Bureau of Standards, Gaithersburg, MD 20899, or call 301/975-6627.

NBS REPORTS TO CONGRESS ON STRUCTURAL DAMAGE IN RECENT CALIFORNIA QUAKE

The biggest share of the structural damage from the October earthquake in California was sustained by older, unreinforced masonry buildings that were not designed to absorb an earthquake's energy or were not connected firmly to their foundations. That assessment was made by John W. Lyons, director of the NBS National Engineering Laboratory in testimony on November 10 before the U.S. House Subcommittee on Science, Research and Technology.

Most of these observations reflect lessons already learned from previous quakes and research, said Lyons, but they are important because in many earthquake-susceptible parts of the country such structures are still being built.

In a report released at the hearings, H. S. Lew, head of the NBS structural evaluation program, also noted that light fixtures and suspended ceilings which were not properly secured fell during the earthquake. In addition, he said, walls with large windows provided little stiffness to the structure and, in many cases, window glass fractured into large pieces and fell on sidewalks.

Lew, who was in California when the quake struck, found only one highway bridge that sustained significant damage. Most bridges had been repaired or strengthened to increase their earthquake resistance after the 1971 San Fernando earthquake in which five bridges collapsed and 42 others were damaged significantly.

As part of the National Earthquake Hazards Reduction Program, NBS conducts research and provides technical support to the private sector and government agencies which are working to improve the performance of buildings and other structures subjected to earthquakes.

Last month, NBS researchers completed a series of laboratory tests on full-scale, reinforced concrete bridge columns under simulated earthquake conditions. This work, partially sponsored by the California Department of Transportation, will help determine the effectiveness of current California design criteria. It also will be used to determine whether small-scale tests and computer models can accurately predict seismic performance of full-scale bridge structures.

NBS also is conducting laboratory studies on the performance of reinforced concrete masonry under earthquake loadings. In addition, Lew and his staff are conducting research on strengthening methods for reinforced concrete structures.

NBS does not issue or enforce standards or regulations. The results of Bureau research will go to groups that do set and enforce such standards and regulations and will provide the basis for safer, more economical design practices.

Lyons said that although this earthquake was modest, it cost three lives directly and more than $200 million in property damages. "It is a warning of the importance of the earthquake threat to the United States," he concluded.

For further information, contact H. S. Lew at the National Bureau of Standards, Gaithersburg, MD 20899.

NBS/GCA JOINT PROGRAM ON "MOLECULAR MEASUREMENT MACHINE"

NBS and GCA Corporation of Andover, Massachusetts, have begun a joint research program in support of an NBS project to develop a prototype measuring machine that will be capable of measuring surface features over an area approximately 5 centimeters square with a resolution of a single atom. The "Molecular Measurement Machine," under design by the NBS, will make use of extremely high-resolution probes, such as a tunneling microscope probe or atomic force probe, and will be able to make surface roughness measurements accurate to a tenth of an angstrom. Stanley Stone of GCA will work with NBS on the design and development of the machine structure, slideways, motor drives, interferometers, and associated control system needed for this new generation of measurement machines.

For further information, contact Clayton Teague at the National Bureau of Standards, Gaithersburg, MD 20899.

POLYMER COMPOSITE PROCESSING RESEARCH NEEDS IDENTIFIED

Two dozen companies met at NBS October 7 to address processing methods and barriers for polymer composites. These composites now are used in defense and specialty products, but other markets are expected to open up if processing methods can be improved.

The session at NBS, which was cochaired by representatives from Ford and NBS, identified a variety of scientific and engineering needs for improved processing methods which are expected to be of most interest to industry during the next 10 to 15 years. This information will be used to develop specific projects at NBS to aid industry in developing and applying these innovative materials.

NBS plans to pursue cooperative projects with industry where appropriate. A report on the workshop will be available in several months.

For further information, contact Donald Hunston at the National Bureau of Standards, Gaithersburg, MD 20899.

NBS PROPOSES FEDERAL STANDARD FOR OSI

NBS is asking for comments on a proposed Federal Information Processing Standard (FIPS) which adopts the Government Open Systems Interconnection Profile (GOSIP). (FIPS are developed by NBS for use by the Federal government.)

GOSIP defines a common set of data communication protocols which enables computer systems

developed by different vendors to communicate and allows the users of different applications on these systems to exchange information. It was developed by the Government OSI Users Committee, a group of Federal government agencies. GOSIP adopts international standards which enable information processing devices to communicate with one another in a network. GOSIP is based on agreements reached by vendors and computer users in NBS-sponsored workshops.

For a copy, contact Standards Processing Coordinator (ADP), Institute for Computer Sciences and Technology, B64 Technology Building, National Bureau of Standards, Gaithersburg, MD 20899, or call 301/975-2816.

Comments on the proposed Federal standard should be sent to Director, Institute for Computer Sciences and Technology, Attn: GOSIP, B154 Technology Building, at the above address.

For technical information, contact Gerard F. Mulvenna, B217 Technology Building, National Bureau of Standards, Gaithersburg, MD 20899, or call 301/975-3631.

MEASURING FAULTS IN PARALLEL PROCESSORS

In a recent study for the Defense Advanced Research Projects Agency, NBS researchers investigated a number of measurement techniques that can be used to detect and recover from hardware faults in parallel processors.

"Fault-tolerance" is particularly important in computer systems used, for example, to solve large problems such as weather forecasting and to control aircraft and spacecraft. The researchers looked at ways to detect transmission and data storage errors and faults in processors, controllers, computer components, and input/output systems.

A report, *On the Measurement of Fault-Tolerant Parallel Processors* (NBSIR 87-3568), is available from the National Technical Information Service, Springfield, VA 22161 for $11.95 prepaid. Order by PB #87-208328/AS.

This work is part of an ongoing research effort to develop techniques and tools to measure the performance of parallel processors.

RESEARCH DETECTS NUCLEAR REACTOR BURN-UP OF USSR CRAFT

A study that examines the 1983 burn-up of a nuclear reactor from the Soviet reconnaissance satellite Cosmos-1402 is the subject of a just-published report. The satellite reactor, which normally would have been boosted into a long-lived orbit, fell into the Earth's atmosphere and disintegrated because of a malfunction.

To examine this event more closely, researchers from the Department of Energy's Environmental Measurements Laboratory (EML) collaborated with NBS scientists to identify reactor particles by analyzing stratospheric filter samples for their ratio of the radioactive isotopes uranium 235 and 238. The project was undertaken because officials from EML—which investigates radioactive injections into the stratosphere—suspected that the reactor burn-up had occurred but had no direct evidence.

The team analyzed atmospheric samples in the NBS inorganic mass spectrometry laboratory, a custom facility well-suited for determining isotopic ratios. The samples, which were collected by special balloons at altitudes of 16 to 23 miles (27 to 39 kilometers), indicated large excesses of U-235. The researchers say this appears to indicate that the reactor did burn up in the stratosphere and that radioactive particles from the event will continue to spread out and dilute, posing no danger on Earth.

The research team's report is in the October 23, 1987, issue of Science.

NBS REPORTS CAUSE OF FATAL BUILDING COLLAPSE

The failure of a key component of the system for lifting concrete floor slabs in the L'Ambiance Plaza apartment building was the most probable cause for the building's April 23, 1987, collapse, said Charles Culver, chief of the NBS Structures Division, at a press briefing on October 22.

Specifically, the collapse probably began when a jack rod supporting three concrete floor slabs slipped out of a U-shaped opening in a steel bracket. NBS researchers pinpointed the location where the jacking system used to lift the slabs into final position most likely failed. They investigated a variety of possible causes of failure, but concluded that only the lifting system failure played a significant role in initiating the collapse in which 28 construction workers died.

NBS was asked by the U.S. Occupational Safety and Health Administration to determine the cause of the collapse.

For information on ordering the NBS report, *Investigation of L'Ambiance Plaza Building Collapse in Bridgeport, Connecticut* (NBSIR 87-3640), contact the Structures Division, B268 Building Research Building, National Bureau of Standards, Gaithersburg, MD 20899, or call 301/975-6048.

GOOD ATRIUM DESIGN CAN SAVE ENERGY

Atrium spaces using large amounts of glass to let in daylight are aesthetic. But are they energy efficient?

Using computer-simulation to evaluate atrium design in eight areas of the United States, NBS researchers found that savings ranging from about five percent in the Madison, Wisconsin, area up to 20 percent in Los Angeles are possible. However, total energy usage for areas like Madison were greater, so the actual dollar savings may be similar.

The researchers looked at several atrium designs and the effects of a variety of options such as solar shading, heat storage, and single- and double-pane glazings. The best-performing options seem to be the double-pane glazing combined with heat storage, but double-pane glazing alone also did well. Single-pane glazing is not effective, particularly in cold climates, and, surprisingly, say the researchers, the solar shading was not beneficial.

A report, *Fenestration Design for Building Atria* (NBSIR 87-3594), can be ordered for $13.95 prepaid from the National Technical Information Service, Springfield, VA 22161. Order by title and PB #87-171427.

NEW WAY TO TEST SETTING TIME, STRENGTH OF CONCRETE

NBS researchers are experimenting with a new test method for measuring the setting time and strength of concrete. The technique, called "impact-echo," uses sound waves and originally was developed by NBS researchers to detect flaws in concrete.

Currently, no standard field or laboratory test is available for measuring the setting time of concrete which may not accurately reflect environmental conditions at the site.

With the impact-echo method, the increase in the speed of sound through concrete is measured and correlated with setting time and subsequent strength development of the concrete.

A report on the method, *Measurement of the Setting Time and Strength of Concrete by the Impact-Echo Method* (NBSIR 87-3575), is available from the National Technical Information Service, Springfield, VA 22161, for $18.95 prepaid. Order by PB #88-111851.

Standard Reference Materials

IMPROVING N-PAH MEASUREMENTS IS AIM OF NEW MATERIAL

Analytical laboratories that measure environmental samples for their concentration of certain nitrated polycyclic aromatic hydrocarbons (N-PAHs) will find a new NBS standard primarily for use in calibrating the chromatographic instruments used to measure these compounds. The new SRM, besides functioning as a calibration tool, also can be used to "spike" laboratory samples with known amounts of N-PAHs for research purposes.

The SRM has certified concentrations of four N-PAH compounds—1-nitropyrene, 1,3-dinitropyrene, 1,6-dinitropyrene, and 1,8-dinitropyrene—in a solution of methylene chloride. Packaged in a kit containing five vials of the certified solution, the new material, Dinitropyrene Isomers and 1-Nitropyrene in Methylene Chloride (SRM 1596), is available for $281.

NBS, E. FJELD CO. PROGRAM ON SUBMICROMETER LINE STANDARDS

The E. Fjeld Company of North Billerica, Massachusetts, a manufacturer of custom apparatus for scanning electron microscopes (SEMs), has started a joint program with the NBS to aid in the development of the next generation of NBS measurement standards for integrated circuit (IC) manufacturers.

E. Fjeld will work with NBS on combining a diamond turning instrument with an SEM for in-process viewing of machining and on the design and development of a special SEM stage linked to a laser interferometer. These instruments will be used for the precision fabrication and measurement of typical IC structures with dimensions below one micrometer on opaque substrates. Such structures may be the basis for a new series of NBS standard reference materials for the measurement of submicrometer IC structures.

NBS Services

NBS, NSA SETTING UP RISK MANAGEMENT LABORATORY

NBS and the National Security Agency's National Computer Security Center are planning to establish a risk management research laboratory at NBS headquarters in Gaithersburg, MD. Risk management involves analyzing information assets, threats, and vulnerabilities; determining a measure of risk; then selecting cost-effective safeguards for reducing that risk.

The laboratory will be used to conduct research and provide the tools, techniques, and guidance needed to conduct this process. Other planned uses

include helping Federal agencies select and use commercial risk management software and providing a clearinghouse for information on risk analysis and management for the Federal government.

For further information, contact Dennis Steinauer, B266 Technology Building, National Bureau of Standards, Gaithersburg, MD 20899, or call 301/975-3357.

NBS ANNOUNCES ACCREDITATION PROGRAM FOR LABORATORIES TESTING ASBESTOS IN SCHOOLS

An accreditation program for laboratories that test for asbestos in schools has been established by NBS under the National Voluntary Laboratory Accreditation Program (NVLAP) to meet the requirements of the Asbestos Hazard Emergency Response Act of 1986. The law requires the Environmental Protection Agency (EPA) to develop a program for the inspection, management, and abatement of asbestos in the nation's schools.

Under the law, NBS will accredit laboratories that perform analysis for asbestos content in samples of bulk insulation and building materials, and analyze airborne particulates collected during school inspections and asbestos abatement projects. The evaluation of laboratories that apply for asbestos bulk testing will commence about October 1988. The first group of laboratories to be evaluated for accreditation will be those applying by December 28, 1987. Those applying after that date will be evaluated on a first-come first-served basis.

Accreditation for testing for airborne asbestos will begin in mid-1989.

For information on the new asbestos program, contact: Harvey W. Berger, Manager, National Voluntary Laboratory Accreditation Program, A531 Administration Building, National Bureau of Standards, Gaithersburg, MD 20899, or call 301/975-4016.

Volume 93, Number 1, January–February 1988
Journal of Research of the National Bureau of Standards

The NBS Scale of Spectral Irradiance

Volume 93 Number 1 January–February 1988

James H. Walker,
Robert D. Saunders,
John K. Jackson, and
Donald A. McSparron

National Bureau of Standards
Gaithersburg, MD 20899

This paper describes the measurement methods and the instrumentation used in the realization and transfer of the NBS scale of spectral irradiance. The basic measurement equation for the irradiance realization is derived. The spectral responsivity function, linearity of response, and "size of source" effect of the spectroradiometer are described. The analysis of sources of error and the estimates of uncertainty are described. The assigned uncertainties (3σ level) in spectral irradiance range from 2.2% at 250 nm to 1.0% at 654.6 nm to 6.5% at 2400 nm.

Key words: blackbody; calibrations; radiometry; response linearity; slit-scattering function; spectral irradiance; standards.

Accepted: September 10, 1987

1. Introduction

Spectral irradiance, denoted E_λ, is defined as the radiant flux of wavelength λ incident on a surface per unit wavelength interval and per unit area on the surface. Mathematically

$$E_\lambda = d^2\Phi/d\lambda \cdot dA, \quad (1)$$

where $d^2\Phi$ is the element of incident flux and $d\lambda$ and dA are the elements of wavelength and area respectively.

The National Bureau of Standards (NBS) presently issues two types of spectral irradiance standards. Type FEL (ANSI designation) lamps, modified to a medium bipost base, are calibrated as standards of spectral irradiance at 31 wavelengths over the spectral range 250 to 2400 nm. Deuterium lamp standards of spectral irradiance are calibrated at 16 wavelengths over the spectral range 200 to 350 nm and at a lower accuracy than the type FEL lamps. Both these lamp standards are designated in NBS Special Publication 250 [1].

In 1963, NBS established a scale of spectral irradiance [2]. In the early 1970's an improved scale was developed [3] with uncertainties about 1/3 those of the earlier scale. The detailed techniques for realizing this scale have undergone several evolutionary changes in the past decade. This paper is a description of the current process of realization of the NBS spectral irradiance scale and of the current procedures for the routine spectral irradiance calibrations.

Modified type FEL lamps are routinely calibrated from 250 to 2400 nm. Deuterium lamps are routinely calibrated from 200 to 350 nm. The spectral irradiance values transferred to the deuterium lamps in the spectral range 200 to 250 nm are based on the hydrogen and blackbody line arcs developed primarily for use in the vacuum ultraviolet [4]. From 250 to 350 nm the reported spectral irradiance values are transferred from the modified type FEL lamps. The equipment used for the deuterium lamp calibrations is identical to that used for the modified type FEL lamp calibrations, and the

measurement procedures are very similar. The body of this paper will be limited to a description of the calibration of the modified type FEL lamps. Detailed information on the calibration services appears in a separate document [5].

2. Scale Derivation and Transfer

The NBS scale of spectral irradiance is derived from the NBS scale of spectral radiance [6] which is based on a realization of the International Practical Temperature Scale (IPTS-68) starting with a gold-point blackbody [7]. The average spectral radiance over the exit aperture of a special integrating sphere source is determined and then the flux from the sphere source which enters the receiving aperture of the spectroradiometer is calculated. This technique is used to determine the spectral irradiance at the detector receiving aperture and thus establishes a spectral irradiance scale. As a matter of convenience the scale is transferred to a group of four, 1000 W, quartz-halogen lamp primary working standards using an averaging sphere-monochromator combination designed for spectral irradiance measurements. These lamps are used to maintain the NBS scale of spectral irradiance. The lamps are recalibrated every 50 to 100 burning hours.

Figure 1 shows the setup used to measure the spectral radiance of the special integrating sphere source. Figure 2 shows the setup used to transfer the spectral irradiance scale to a group of primary working standards.

The geometry used for the spectral irradiance determination is shown in figure 3. The following method is used to determine the spectral irradiance at the receiving aperture of the spectroradiometer produced by the integrating sphere source. The spectral irradiance, E_λ, at the receiving aperture due to the spectral radiance, L_λ, at any point on the source aperture is

$$E_\lambda = \int_\omega L_\lambda \cdot d\omega, \tag{2}$$

where ω is the solid angle defined by the receiving aperture and a point on the source aperture. To calculate the flux at the receiving aperture due to the entire source aperture, it is necessary to integrate over the entire projected area of the source aperture

$$\Phi_\lambda = \int_A \int_\omega L_\lambda \cdot d\omega \cdot dA, \tag{3}$$

where $dA = dx \cdot dy \cdot \cos\theta$. L_λ is a function of θ, ϕ, x, and y so that

$$\Phi_\lambda = \int_A \int_\omega L_\lambda(\theta, \phi, x, y) \cdot \cos\theta \cdot d\omega \cdot dx \cdot dy, \tag{4}$$

where:

θ is the angle between the normal to the surfaces of the apertures and a line connecting a single point on each aperture,

ϕ is the azimuthal angle,

x is the horizontal location of a point on the source aperture,

y is the vertical location of a point on the source aperture.

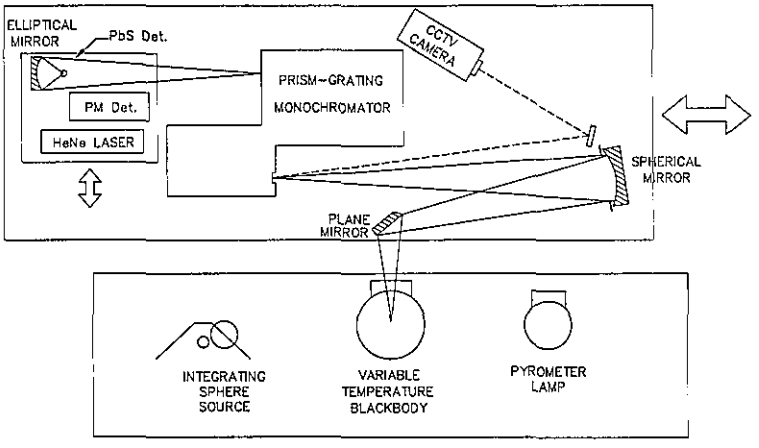

Figure 1. Spectral radiance measurement setup.

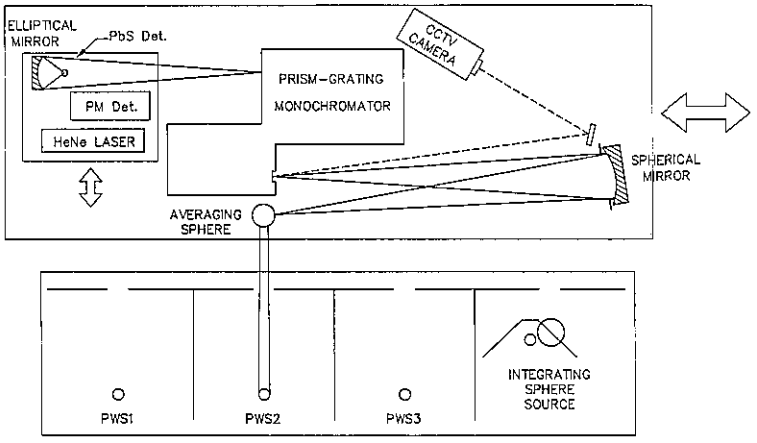

Figure 2. Spectral irradiance measurement setup.

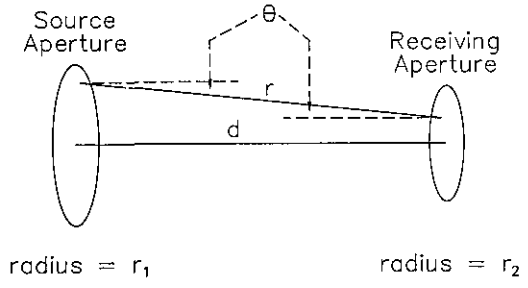

Figure 3. Irradiance calculation geometry.

Assuming that the source is Lambertian and nearly uniform, $L_\lambda(\theta, \phi, x, y)$ can be replaced by an average radiance $\bar{L}_\lambda$ to give

$$\Phi_\lambda = \bar{L}_\lambda \cdot \int_A \int_\omega \cos\theta \cdot d\omega \cdot dx \cdot dy, \quad (5)$$

where:

$d\omega = \cos\theta / r^2 \cdot dx' dy'$,
x', y' is a point on the receiving aperture,
r is the slant distance from x', y' to x, y.

This gives

$$\Phi_\lambda = \bar{L}_\lambda \cdot \int_{A_{SA}} \int_{A_{RA}} \cos^2\theta / r^2 \cdot dx' \cdot dy' \cdot dx \cdot dy, \quad (6)$$

where:

A_{SA} is the area of the source aperture,
A_{RA} is the area of the receiving aperture.

For circular, coaxial source and receiving apertures, this integral evaluates to

$$\Phi_\lambda = \bar{L}_\lambda \cdot \pi^2/2 \cdot [R^2 - (R^4 - 4 \cdot r_1^2 \cdot r_2^2)^{1/2}], \quad (7)$$

where:

$R^2 = d^2 + r_1^2 + r_2^2$,
d is the normal distance between source and receiving apertures,
r_1 is the radius of the source aperture,
r_2 is the radius of the receiving aperture.

A more convenient expression is

$$\Phi_\lambda = \bar{L}_\lambda \cdot (\pi \cdot r_1^2) \cdot (\pi \cdot r_2^2) / R^2 \cdot [1 + \delta + 2 \cdot \delta^2 + 5 \cdot \delta^3 + \ldots], \quad (8)$$

where $\delta = (r_1^2 \cdot r_2^2)/R^4$. Finally,

$$E_\lambda = \Phi_\lambda / A_{RA} = \bar{L}_\lambda \cdot (\pi \cdot r_1^2)/R^2 \cdot [1 + \delta + \ldots]. \quad (8a)$$

The final step is to compare the spectroradiometer outputs produced by the integrating sphere source and each working standard.

Once the primary working standards have been calibrated, they are used to measure the spectral irradiance of test lamps. Modified type FEL test lamps are calibrated in groups of twelve.

3. Measurement Apparatus

Spectral radiance and spectral irradiance calibrations are performed on the NBS Facility for Automated Spectroradiometric Calibrations (FASCAL) [8]. Block diagrams of the measurement apparatus are shown in figures 1 and 2. The principal components are:

1. Variable-Temperature Blackbody
2. Sources

Pyrometer Lamp
Special Integrating Sphere Source
Spectral Irradiance Primary Working Standards
Test Lamps
3. Spectroradiometer
Fore-optics
Avenging Sphere
Mirrors and Entrance Slit Masks
Monochromator
Detectors
4. Control and Data Acquisition System

3.1 Variable-Temperature Blackbody

The variable-temperature blackbody is used over a temperature range from about 800 °C to about 2400 °C.

A schematic cross section of the variable-temperature blackbody is shown in figure 4. The blackbody cavity is located in the central portion of a high density graphite tube, which is resistively heated in an argon atmosphere. Electric current is supplied to the graphite tube through water-cooled electrical connections at each end of the tube. The tube is surrounded by a double-walled graphite radiation shield, with carbon black fill between the walls. This assembly is surrounded by a water-cooled metal housing, with an observation port which can be sealed during evacuation of the atmosphere within the housing prior to flushing with argon. A window is provided at the top of the housing for visual pyrometer observation of the temperatures along the tube interior. A second window at the rear of the housing allows radiation from the rear wall of the graphite tube to fall on a silicon photodiode. The photodiode provides a signal for automatic control of the saturable-reactor power supply for the tube. A germanium photodiode, whose response extends further into the infrared region, replaces the silicon cell for operation at temperatures below 1000 °C. The blackbody mounting provides adjustment in two angular and three translational degrees of freedom, allowing for precise positioning and radiometric scanning over the target area and the beam solid angle.

The graphite tube is about 200 mm long, with an inner diameter of about 11 mm. The outer surface is tapered to improve temperature uniformity along its length. The wall is about 4 mm thick at mid-length where a 2 mm diameter hole in the wall allows for observation of the emitted flux. The tube is partitioned into small cylindrical sections by a series of thin graphite disks separated by thin graphite cylinders located at intervals along the bore. Holes in the graphite disks permit measurement of the temperatures in the middle and upper sections with a visual pyrometer. The holes vary in diameter from 6 mm for the uppermost disk to 0.75 mm for the disk below the central section. The central cylindrical section, which provides the observed flux, is 9 mm high and 10 mm in diameter. The inside wall is threaded to reduce its partial reflectivity [9,10]. Figure 5 shows a cross-sectional view of the central section.

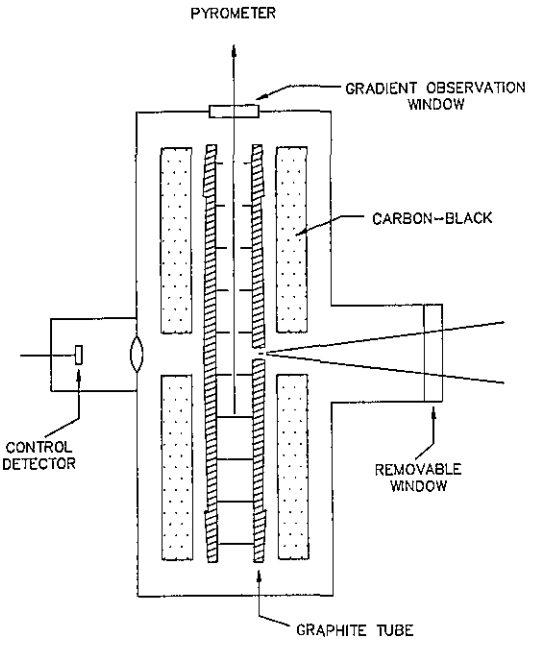

Figure 4. Variable-temperature blackbody schematic.

The blackbody emissivity has been assessed by measurements of the solid angle subtended by the cavity opening, the partial reflectivity of the graphite material [9], the temperature gradients, and the absorption by gases [10]. The solid angle subtended at the rear wall of the cavity by the inner edge of the observation hole is about 0.03 sr. The measured partial reflectivity of the graphite is 0.02 sr^{-1}. The measured temperature gradient over the length of the viewing cavity is less than 1 K. Experimental investigations of possible absorption of radiation by gases has disclosed only weak absorption lines at 589 and 589.6 nm (Na) and at 766.5 nm (K). The resulting estimate of emissivity is 0.9990 ± 0.0005.

3.2 Sources

3.2.1 Pyrometer Lamp This lamp is used as a secondary standard for realizing the spectral radiance

scale. It is a highly stable vacuum tungsten-strip lamp which is operated at a single current to produce a spectral radiance of about eight times that of a gold-point blackbody at 654.6 nm (about 1530 K radiance temperature). The lamp drift rate is less than 0.02% per 100 hours when operated at a single current level.

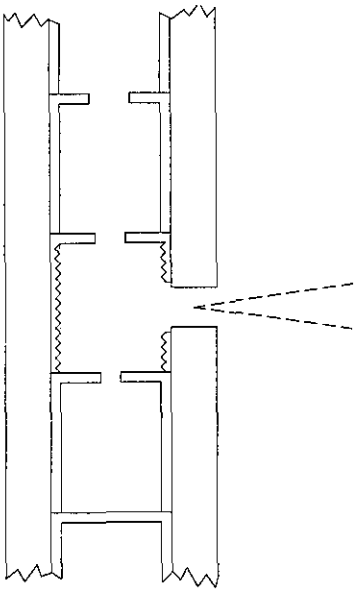

Figure 5. Central section of variable-temperature blackbody.

3.2.2 Special Integrating Sphere Source This source has been specially constructed to be unpolarized and to have high output in the IR part of its spectrum. It consists of a heat-sinked, water-cooled integrating sphere with a 1000 W quartz-halogen, modified type FEL lamp mounted next to the entrance port. The integrating sphere is 5.0 cm in diameter with a 23 mm diameter entrance port and a 20 mm diameter exit port located about 100° from the entrance port. The inside sphere wall is coated with pressed high purity polytetrafluoroethylene (PTFE) [18] to give high reflectivity in the IR. A modified type FEL lamp is mounted with its envelope about 3 mm from the entrance port of the sphere and located so that it does not directly irradiate the inside wall of the sphere opposite the exit port. The sphere itself is made of copper and is mounted in a heat-sinking copper plate. Copper tubing is soldered to the sphere and plate and the entire assembly is water-cooled to prevent the source from overheating. A precision circular aperture whose area has been accurately measured is attached at the exit port.

Because of the multiple reflections in the integrating sphere, entering radiation is randomized, producing a uniform, depolarized radiant flux at the exit port. The uniformity is verified when the exit port aperture is mapped during the irradiance realization procedure (fig. 6 shows a typical mapping profile). Depolarization was tested at 650 nm using an unpolarized source and a linear polarizer and found to be complete within the measurement precision of 0.1% (3σ level).

3.2.3 Spectral Irradiance Primary Working Standards Four 1000 W quartz-halogen, modified type FEL lamps were selected as primary working standards. This type lamp has a clear bulb and a tungsten coiled-coil filament (CC-8) and has a rated life of 500 hours at 120 V. Before calibration, the lamp base is converted to a medium bipost base and the base structure is encapsulated in an epoxy-ceramic compound. The posts that form the bipost base are 6.35 mm (1/4 in) diameter cylindrical stainless steel rods that extend 20.64 mm (13/16 in) from the bottom of the epoxy-ceramic block. The posts are spaced 22.23 mm (7/8 in) between centers. A metal plate bearing the lamp identification number and indicating the electrical polarity is attached to the rear surface (side away from the spectroradiometer) of the epoxy-ceramic block.

3.2.4 Test Lamps The test lamps are also modified type FEL lamps. A lamp screening process is used to select test lamps suitable for calibration. Lamps are annealed and then are checked for stability, emission lines or absorption bands, and for variations in goniometric output.

3.3 Spectroradiometer

3.3.1 Fore-optics

Averaging Sphere The averaging sphere is 2.5 cm in diameter with a 1 cm^2 area precision circular entrance port and a 3×12 mm exit port located about 100° from the entrance port. The inside sphere wall is coated with pressed high purity PTFE. This material has been found to fluoresce at certain wavelengths under certain conditions [19], but when the sources being compared have approximately the same spectral distribution, fluorescence is not a problem. The radiation entering the sphere is randomized by multiple reflections in the sphere, thus producing uniform, depolarized radiant flux at the exit port. This uniformity was verified to within the measurement precision of 0.1% (3σ level) by radiometrically scanning the exit port of the sphere. Depolarization was tested at 500 nm and 650 nm using an unpolarized source and a linear polarizer and found to be complete within the measurement precision of 0.1% (3σ level).

						0.22	0.30	0.31							
				0.28	0.28	0.23	0.21	0.28	0.31	0.30	0.31	0.44			
			0.45	0.25	0.14	0.13	0.15	0.21	0.28	0.36	0.43	0.48	0.46		
		0.42	0.21	0.08	0.03	0.06	0.09	0.15	0.20	0.31	0.42	0.48	0.53	0.61	
	-0.10	0.25	0.06	-0.04	-0.04	0.03	0.12	0.16	0.18	0.24	0.37	0.43	0.55	0.67	0.75
	0.32	0.11	-0.05	-0.11	-0.07	0.04	0.11	0.13	0.14	0.21	0.31	0.40	0.53	0.67	0.79
-0.44	0.21	-0.00	-0.15	-0.18	-0.13	-0.02	0.05	0.10	0.11	0.15	0.22	0.33	0.49	0.66	0.80	0.86
0.46	0.15	-0.07	-0.21	-0.22	-0.14	-0.05	-0.01	0.06	0.08	0.13	0.18	0.25	0.42	0.61	0.80	0.88
0.40	0.11	-0.12	-0.26	-0.26	-0.21	-0.14	-0.08	0.00	0.05	0.08	0.13	0.24	0.38	0.60	0.84	0.95
0.43	0.14	-0.11	-0.29	-0.29	-0.24	-0.18	-0.12	-0.05	-0.00	0.06	0.14	0.26	0.44	0.67	0.93	1.08
-0.21	0.15	-0.10	-0.32	-0.34	-0.31	-0.25	-0.19	-0.14	-0.10	-0.00	0.12	0.28	0.46	0.68	0.94	1.09
	0.12	-0.13	-0.36	-0.42	-0.41	-0.35	-0.30	-0.22	-0.16	-0.01	0.15	0.30	0.47	0.67	0.93	
	0.07	-0.12	-0.34	-0.43	-0.43	-0.37	-0.33	-0.27	-0.20	-0.02	0.15	0.32	0.50	0.69	0.90	
		-0.14	-0.35	-0.45	-0.47	-0.42	-0.37	-0.30	-0.20	-0.03	0.16	0.36	0.52	0.68		
			-0.29	-0.40	-0.44	-0.40	-0.34	-0.27	-0.16	0.00	0.17	0.35	0.50			
				-0.41	-0.41	-0.38	-0.29	-0.21	-0.10	0.05	0.23	0.29				
							-0.27	-0.19	-0.08							

Values are % difference from central value
Wavelength = 654.6 nm
Target area = 0.6 nm wide by 0.8 nm high
X Increment = 1.06 nm
Y Increment = 1.06 nm
Overall mapping correction = +0.14%

Figure 6. Mapping profile of integrating sphere aperture.

The difference in the solid angle of irradiation for the irradiance lamp and the integrating sphere source is only a problem when the reflectance of the averaging sphere wall is not uniform. This high purity, 3 mm thick PTFE sphere coating provides this uniformity, and it was verified by determining the spectral irradiance of a lamp mirror-system [3] whose solid angle could be varied. Negligible difference (<0.1%) in the results was observed over the range of solid angles viewed (the conical full angle was varied from 1.85° to 10°).

Mirrors and Entrance Slit Masks In the radiance measurement mode, the radiance source is imaged with unit magnification onto a polished stainless steel mask placed directly in front of the entrance slit of the monochromator. In the irradiance measurement mode, the exit port of the averaging sphere is imaged with unit magnification onto a different polished stainless steel mask. The mask determines the height of the system field stop (source target area) and the entrance slit determines the width. In the radiance mode the stop dimensions are 0.6 mm wide by 0.8 mm high. Also, in this mode the optic axis lies within 1.5° of the axis of the spherical mirror to minimize aberration [11]. In the irradiance mode the stop dimensions are approximately 2 mm wide by 10 mm high. In this mode the off-axis angle is slightly larger, but in this case the image quality is less important because of the homogeneity of the flux exiting the averaging sphere.

3.3.2 Monochromator A prism-grating double monochromator is employed to minimize spectral scattering and to avoid multiple orders. It is used over the wavelength range of 200 to 2400 nm. The dispersion varies with wavelength from about 1 to 4 nm/mm. The entrance aperture (solid angle) is rectangular in shape, with a vertical angle of 7° and a horizontal angle of 3.5°. The wavelength setting is calibrated against Hg line standards from 250 to 580 nm and against Th line standards from 800 to 2400 nm. (See reference [5] for specific lines.) The wavelength calibration is repeatable to within 0.05 nm. The entrance, intermediate, and exit slits are

adjustable together as a unit from 0.01 to 3.0 mm, resulting in a nearly triangular-shaped spectral bandpass.

3.3.3 Detectors Two interchangeable detectors are used to cover the wavelength range of the spectroradiometer. For the 200 to 850 nm range, an end-on 11-stage photomultiplier with quartz window and S-20 spectral response is placed behind the exit slit. The detector is cooled to 258 K with a thermoelectric cooler. The anode current is amplified and converted to a 0 to 10 V signal by a programmable dc amplifier. To ensure linearity of response, the high voltage applied to the detector is normally selected to restrict the detector current to 500 nA or less.

A lead sulfide detector, cooled to 240 K by a thermoelectric cooler, is used for the 800 to 2400 nm range. The detector and the exit slit are placed at the foci of an ellipsoidal mirror, which images the exit slit upon the detector with a demagnification of about 7. The detector output is amplified and converted to a 0 to 1 V signal by a phase-sensitive lock-in voltmeter, which is keyed to a 78 Hz sector disk placed just before the plane mirror in the radiance mode or just after the exit port of the averaging sphere in the irradiance mode.

The signal from either detector-amplifier combination is fed to a 5 1/2 digit voltmeter, capable of integration times ranging from one second to several minutes. To facilitate alignment of optics or sources, a HeNe laser is placed at the detector position, so that its beam passes through the monochromator and fore-optics in the reverse direction.

3.4 Control and Data Acquisition System

After initial alignment, the FASCAL system permits control of the entire measurement process from a remote operator console. Component positions, instrument settings, sequence of operations, and data collection are effected by either stored computer programs, operator commands, or a combination of the two.

The system is directed by a microcomputer equipped with a CRT terminal and keyboard and a high-speed disk system for program and data storage. A modular interface controller [12] provides the link between instruments and computer. All measurement signals are multiplexed into the digital voltmeter through the interface scanner, and the instruments are remotely programmed and controlled through interface modules. All instrument settings and signal outputs are printed and stored on disk for later analysis.

The spectroradiometer (fore-optics, monochromator, and detectors), a closed-circuit TV camera, and a photoelectric pyrometer are mounted on a carriage. The carriage can be moved by remote command along a linear track, to position the spectroradiometer in front of any of the sources mounted at fixed stations along the track. The average move time between stations is a few seconds, and positions are repeatable to about 0.1 mm. The TV camera presents a highly magnified image of the monochromator entrance slit mask to video displays at the spectroradiometer and at the operator console for initial source alignment and subsequent monitoring. The pyrometer is used for the initial setting of the variable-temperature blackbody to its approximate temperature.

4. Measurement of Instrument and Source Parameters

4.1 Spectral Responsivity Function

The relative spectral responsivity function of the spectroradiometer is determined by an indirect method [13]. In this method, the relative responsivity function is treated as the product of two terms, the responsivity factor and the slit-scattering function, where the responsivity factor depends only upon the wavelength of the observed flux and the slit-scattering function depends only upon the difference between the wavelength setting of the monochromator and the wavelength of the flux. This factorization of the spectral responsivity function is valid if the instrument dispersion, aberrations, scattering, and diffraction are constant over the wavelength region of interest. This assumption is valid in the central portion of the relative responsivity function, but values for the distant wings are subject to error due primarily to changes in scattering and dispersion.

The responsivity factor is obtained by spectrally scanning a continuous source standard of spectral radiance using narrow (0.1 mm) slits. To determine the slit-scattering function, an integrating sphere irradiated by a high-powered laser is spectrally scanned by the spectroradiometer, with the slit widths set at the 0.6 mm width used in the scale realization and transfer. The plot of the output signal versus wavelength is the mirror image of the plot of the slit-scattering function versus wavelength. For a 647 nm Kr laser, the function is nearly triangular in shape with a width at half-height of 2.5 nm. Relative to the peak value, the measured values decrease to about 10^{-3} at 3 nm, 10^{-4} at 15 nm, and 10^{-7} at 70 nm from the central

wavelength. At 150 nm from the central wavelength, the value decreases to 10^{-8} in the short-wavelength wing and to 10^{-9} in the long-wavelength wing. Scans with 488 nm (Ar), 514 nm (Ar), and 676 nm (Kr) yield similar results. These values were confirmed over the central and near wing portions of the function by measurements with the direct method, using a dye laser tuned through a series of wavelengths with the spectroradiometer set at a fixed wavelength [14].

The measurement at 647 nm yielded the slit-scattering function used for 654.6 nm, where the spectral distribution mismatch of a variable-temperature blackbody and a gold-point blackbody requires an accurate determination of the relative responsivity function. However, the measurements in the visible cannot be applied with confidence to the short-wavelength region, since the dispersion varies by about a factor of 2.5. For this region, the central portion and near wings of the slit-scattering function are determined by scans of a spectral line discharge source, and values in the distant long-wavelength wing are deduced from a measurement of the integrated spectrally-scattered radiation. With the wavelength set at a selected value in the 200 to 250 nm region, the signal from a calibrated lamp (radiance temperature 2475 K at 654.6 nm) is recorded. A glass filter which blocks all radiation in the vicinity of the wavelength setting and passes about 90% of the radiation at longer wavelengths is inserted into the beam. The ratio of signals with and without filter is taken as the fractional contribution of spectrally scattered radiation to the signal. A second (identical) filter is added to insure that only scattered light is being observed in the filtered beam. Results with filters of different cutoff wavelengths (Corning filters CS 0-56 and CS 0-52) both indicate an integrated scattered light contribution of less than 0.2% at 225 nm. The slit scattering function calculated from this result and the known source distributions and responsivity factor are less than 10^{-9} at wavelengths greater than 200 nm from the central wavelength, in good agreement with the values measured in the visible.

4.2 Linearity of Response

The degree of linearity of the spectroradiometer response is determined with an automated beam conjoiner [15,16]. A beam from a constant source is split into two branches whose fluxes are independently attenuated or blocked before recombination and further attenuation. The flux from both branches measured together should equal the sum of the fluxes from each branch when measured separately (additivity). The device provides 96 levels of flux ranging over a factor of about 500. The levels are presented in random order to avoid systematic errors and are interspersed with 29 zero flux levels. A microcomputer controls the attenuating filters and records the filter positions and radiometer signals. The data is least-squares fitted to a polynomial response function to determine a correction factor by which the radiometer output signal must be multiplied to obtain a quantity proportional to radiant flux.

The response function of the spectroradiometer is dependent upon the detector-amplifier employed. With the photomultiplier tube in place (spectral range 200 to 850 nm), the instrument response at all wavelengths is linear to within 0.2% for a range of anode currents from 1 to 500 nA. Linearity measurements were performed at 900, 600, 300, and 250 nm. For currents much less than 1 nA, the signal is limited by noise. For currents greater than 1 μA the correction increases rapidly, rising to 3% at 7 μA. The anode current is restricted to less than 500 nA during measurements by selection of appropriate photomultiplier tube voltage. Correction factors for the amplifier ranges are determined from the measurement of a known electrical current and combined with the linearity correction factor.

Linearity tests of two PbS detectors resulted in a correction factor which is a linear function of the signal over the range 1 to 280 mV. The correction varies from 0.1% at 3 mV to about 9% at 300 mV. To avoid relying on large corrections, sources are typically operated at near equality in the PbS spectral region.

4.3 Size of Source

The "size of source" effect (signal contribution due to flux which originates outside the target area and is scattered into the measured beam by the fore-optics) is determined by observing the change in signal from a 0.6 by 0.8 mm area of a uniform diffuse source while placing various size masks on the diffuse source. The masks expose source areas which closely approximate the radiant areas of the lamp, the blackbody and the integrating sphere source used in the scale realization. As a check, the effect is also evaluated by observing changes in the near-zero signal from a "black hole" (an absorbing cavity slightly larger than the 0.6 by 0.8 mm field stop) as the various surrounding area masks are positioned. The observed differences are used to apply a correction to the signals observed in source

comparisons. The effect is measured at wavelengths of 654.6 and 350 nm, and values for other wavelengths are estimated from the assumption of an inverse wavelength dependence. The correction varies from 0.04% to 0.1% at 654.6 nm depending upon the elapsed time since the last mirror recoating.

4.4 Polarization

The polarization properties of the spectroradiometer and the sources do not play a significant role in the spectral irradiance realization and will not be discussed here. A discussion of polarization properties can be found in reference [6].

5. Process of Spectral Irradiance Realization

The spectral radiance of the special integrating sphere source is determined so that it can be used as a transfer standard for determining spectral irradiance. The spectral radiance output from the center point of the integrating sphere aperture is compared to the spectral radiance output from a variable-temperature blackbody. The temperature of the blackbody is determined by comparing it at 654.6 nm to a high stability vacuum pyrometer lamp calibrated for a single temperature (about 1530 K). The spectral radiance of the integrating sphere source is determined at 31 different wavelengths from 250 to 2400 nm. The aperture of the integrating sphere is mapped at 2000, 1050, 654.6 and 300 nm and its average spectral radiance is computed for each wavelength. Figure 6 shows a typical mapping profile of the integrating sphere aperture. The mapping correction varied less than 0.1% over the range of wavelengths measured.

The spectroradiometer is changed from the spectral radiance mode to the spectral irradiance mode (see figs. 1 and 2) and the spectral irradiances from the NBS primary working standards (PWS) are compared to the spectral irradiance from the integrating sphere source (ISS). Appropriate partitions and baffles are erected to reduce scattered light to less than 0.1%. The comparisons are done at the same 31 wavelengths at which the integrating sphere source was calibrated for spectral radiance. Two separate determinations are performed on each primary working standard. The spectral irradiance of a primary working standard is determined using the relationship

$$E_\lambda(\mathrm{PWS}) = L_\lambda \cdot (\pi \cdot r_1^2)/R^2 \cdot S_{\mathrm{PWS}}/S_{\mathrm{ISS}}, \qquad (9)$$

where $S_{\mathrm{PWS}}/S_{\mathrm{ISS}}$ is the ratio of the irradiance signal from the primary working standard to the irradiance signal from the integrating sphere source. The first part of the expression comes from eq (8a) where $\delta \approx 2 \cdot 10^{-16}$.

The absolute output from the integrating sphere source is monitored at six wavelengths (2000, 1600, 1050, 800, 600, and 400 nm) during the 30 to 40 operating hours necessary to calibrate the primary working standards. Finally, the blackbody is used again to perform an abbreviated spectral radiance calibration of the integrating sphere source. Spectral radiance drift corrections, linear with time, for the integrating sphere source can then be made if necessary.

The measurement of the spectral radiance or spectral irradiance at a single wavelength takes from about 4 to 8 minutes, so it is only necessary for our detectors to have good short term stability.

6. Process of Spectral Irradiance Transfer

The four modified FEL primary working standards are used to perform spectral irradiance calibrations on test lamps. For a selected group of 12 test lamps, each lamp is measured four times, once in each of the four source positions and once against each of the four primary working standards. The screening and selection of test lamps can take several weeks and the calibration procedure for 12 test lamps takes from 2 to 3 weeks. Details of the routine spectral irradiance calibrations appears in a separate document [5].

7. Scale Realization Data Analysis

The spectral irradiance scale is generally realized at the following 31 wavelengths:

250 nm	600 nm
260	654.6
270	700
280	800
290	900
300	1050
310	1150
320	1200
330	1300
340	1540
350	1600
400	1700
450	2000
500	2100
555	2300
	2400

Certain wavelength regions in the IR are skipped (around 1400 nm and 1800 to 1980 nm) in order to avoid atmospheric absorption bands.

Since the total operating time for each primary working standard during a complete scale realization is relatively short (8 to 12 hours), no effort is made to account for irradiance lamp drift. The final assignment of spectral irradiance is simply attributed to the lamp as of the midpoint of the burning time. Between scale realizations when the group of four primary working standards is being used as a basis for calibrating additional lamps, their drifts are taken into account. Various empirical drift models have been used [3]. The present drift equation is

$$E_\lambda = A + B \cdot t, \tag{10}$$

where:

t is time in burning hours,
A and B are constants determined by fitting.

The fitting is performed independently at each wavelength.

Drift of the spectral radiance of the integrating sphere source is taken into account by simple linear interpolation in time between the initial and final spectral radiance values.

An interpolation equation was developed for calculating the spectral irradiance of tungsten halogen lamps at wavelengths between the 31 calibrated wavelengths. This equation is

$$E_\lambda = (A_0 + A_1 \cdot \lambda + \ldots + A_n \cdot \lambda^n) \cdot \lambda^{-5} \cdot \exp(a + b/\lambda). \tag{11}$$

Setting the polynomial equal to 1, multiplying both sides by λ^5, and taking the log of both sides gives $\ln(E_\lambda \cdot \lambda^5) = a + b/\lambda$, in which it will be recognized that $\exp(a)$ is an effective gray-body emissivity and b is closely related to the reciprocal of the distribution temperature. A least squares fitting using a weighting of 1 is performed to determine a and b. With a and b thus fixed, eq (11) is least squares fitted using a weighting of $1/E_\lambda^2$ (assuming constant percentage measurement error) to determine $A_0, A_1, \ldots A_n$. In practice it has been found that the final fit is considerably improved if the spectrum is broken into two spectral regions, 250 to 400 nm and 350 to 1600 nm, for separate fitting. See reference [3] for examples of fitting eq (11) to lamp data. This method is only valid for the continuous spectrum and does not predict emission lines and absorption bands. Spectral irradiance values predicted using eq (11) have an uncertainty of about 0.5%.

8. Uncertainty Estimation

The spectral irradiance scale uncertainty analysis is broken down into three parts. First, the uncertainty in the spectral radiance of the integrating sphere source is determined. Second, the uncertainty in the transfer to the spectral irradiance primary working standards is determined. Third, the uncertainty in the transfer from the primary working standards to the irradiance test lamps is determined. The overall uncertainty in the primary working standards is determined by combining in quadrature the first and second parts. The overall uncertainty in a group of test lamps is determined by combining in quadrature all three parts. All uncertainties are estimated at the 3σ level.

8.1 Integrating Sphere Source Spectral Radiance Uncertainty

The uncertainties in the spectral radiance values assigned to the integrating sphere source are obtained from the observed precision of the measurements and the estimated systematic error in both the measured and the provided quantities (e.g., temperature of melting gold). Uncertainties obtained from the observed precision and from the published values of the physical constants are based upon three standard deviations. Uncertainties of systematic errors are estimated at the equivalent of three standard deviations.

In order to examine the contributions of the various errors to the uncertainty in the spectral radiance of the integrating sphere source, an approximate equation for the complete measurement process was derived by using the Wien approximation to the Planck relation. The details of the derivation are described in reference [6]. The resulting equation is

$$L_\lambda \cong (s_\lambda \cdot \epsilon_B \cdot d \cdot M_\lambda)\left[c_1/[\pi \cdot \lambda^5 \cdot (e^{c_2/\lambda \cdot T_{Au}})]\right] \cdot (s_r \cdot f_r \cdot M_r/\epsilon_B)^{\lambda_r/\lambda}, \tag{12}$$

where, with VTBB denoting the variable-temperature blackbody and GPBB denoting the gold-point blackbody, the definitions of the quantities are:

M_λ, signal ratio of the VTBB-integrating sphere source comparison,
M_r, signal ratio of the GPBB-VTBB comparison,
s_λ, size-of-source correction for the VTBB-integrating sphere source comparison,

ϵ_B, effective emissivity of the VTBB,

d, correction for integrating sphere source drift during calibration,

s_r, size-of-source correction for the GPBB-VTBB comparison,

f_r, linearity-range factor correction,

T_{AU}, IPTS-68 temperature of melting gold,

c_1, first radiation constant,

c_2, second radiation constant,

λ, wavelength of the VTBB-integrating sphere source comparison,

λ_r, wavelength of the GPBB-VTBB comparison, 654.6 nm.

Spectral radiance uncertainties due to the factors of eq (12) are obtained from the partial derivative with respect to those factors and the estimated uncertainty in the factor. Differences between errors calculated by eq (12) and those calculated by the exact Planck relation are negligible. Note that for the wavelengths λ and λ_r this process yields the error due to inserting the wrong wavelength in the spectral radiance calculation, not the error due to an incorrect wavelength setting.

In addition to the factors which appear explicitly in eq (12), uncertainties in the ratios M_λ and M_r arise from errors in the wavelength settings λ (0.1 nm) and λ_r (0.05 nm), in the current measurements of the vacuum pyrometer lamps (0.2 mA) and the integrating sphere source lamp (0.3 mA), and in the measured spectral responsivity function. The uncertainties in the ratios due to wavelength setting and electric current are assessed at a number of wavelengths by measurement of the change in signal ratio when varying these quantities. This technique for determining the effect upon the signal ratios due to the uncertainties in the measured spectral responsivity function is derived in reference [20]. The spectral radiance uncertainties due to these factors are then deduced from the ratio uncertainties as before. The signal ratio, lamp current, and wavelength setting errors are considered random; the remaining errors are systematic.

Table 1 lists the uncertainties obtained by this process. The calculated uncertainties, in percent of spectral radiance, are tabulated for a number of wavelengths over the calibration range. The individual values are combined in quadrature to yield the combined uncertainty for each wavelength. These uncertainties apply to the spectral radiances values of the integrating sphere source.

Table 1. Integrating sphere source spectral radiance uncertainty (3σ) in percent

	Wavelength (nm)							
Source of error	250	350	654.6	900	1300	1600	2000	2400
T_{Au} (s)	1.29	0.92	0.49	0.36	0.25	0.20	0.16	0.13
M_r (r)	0.16	0.11	0.08	0.20	0.17	0.12	0.09	0.36
M_λ (r)	0.25	0.18	0.08	0.20	0.22	0.33	0.66	1.08
s_r (s)	0.26	0.19	0.10	0.07	0.05	0.04	0.03	0.03
s_λ (s)	0.10	0.10	0.10	0.10	0.10	0.10	0.10	0.10
f_r (s)	0.26	0.19	0.10	0.07	0.05	0.04	0.03	0.03
d (s)	0.10	0.10	0.10	0.10	0.10	0.10	0.10	0.10
ϵ_B (s)	0.16	0.09	0.00	0.03	0.05	0.06	0.07	0.07
λ_r setting (r)	0.15	0.08	0.04	0.02	0.01	0.00	0.01	0.01
λ setting (r)	0.03	0.04	0.03	0.01	0.02	0.01	0.01	0.01
c_1 (s)	0.00	0.00	0.00	0.00	0.00	0.00	0.00	0.00
c_2 (s)	0.13	0.10	0.05	0.04	0.03	0.02	0.02	0.01
Lamp currents:								
Quinn-Lee (r)	0.11	0.08	0.04	0.03	0.02	0.02	0.01	0.01
1530 K (r)	0.05	0.04	0.02	0.02	0.01	0.01	0.01	0.01
ISS (r)	0.08	0.06	0.03	0.02	0.02	0.01	0.01	0.01
Spect. resp. (s)	0.08	0.06	0.03	0.02	0.02	0.02	0.01	0.01
Quadrature sum	1.41	1.01	0.55	0.49	0.41	0.44	0.70	1.16
Quadrature sum without T_{Au}	0.58	0.42	0.25	0.34	0.33	0.39	0.69	1.15

Notes: Random errors denoted by (r), systematic errors by (s).
Sources of error described in section 8.1.

8.2 Radiance to Irradiance Transfer Uncertainty

The uncertainty in the transfer from the integrating sphere source to the spectral irradiance primary working standards is obtained from examining the contributions of the various errors in the following measurement equation,

$$E_\lambda(\mathrm{PWS}) = m \cdot d_1 f \cdot (S_{\mathrm{PWS}}/S_{\mathrm{ISS}}) \cdot L_\lambda(\mathrm{ISS}) \cdot [(\pi \cdot r_1^2)/R^2], \quad (13)$$

where:

E_λ(PWS), spectral irradiance of a primary working standard,

m, mapping correction for the average spectral radiance of the integrating sphere source,

d_1, integrating sphere source drift correction,

f, linearity-range factor correction,

$S_{\mathrm{PWS}}/S_{\mathrm{ISS}}$, signal ratio of the primary working standard-integrating sphere source comparison,

L_λ(ISS), spectral radiance of the integrating sphere source,

$(\pi \cdot r_1^2)/R^2$, geometric factor in the irradiance calculation [see eqs (7), (8a), and (9)]

In addition to the factors which appear explicitly in eq (13), uncertainties in the ratio $S_{\mathrm{PWS}}/S_{\mathrm{ISS}}$ arise from errors in the wavelength settings and in the electrical current measurements of the sources. There are also uncertainties due to spectral scattering, stray light, and averaging sphere responsivity. All these uncertainties have been evaluated and are listed in table 2.

8.3 Test Lamp Irradiance Transfer Uncertainty

The uncertainty in the transfer from the spectral irradiance primary working standards to a group of irradiance test lamps is obtained from examining the contributions of the various errors in the following measurement equation,

$$E_\lambda(\mathrm{TL}) = f \cdot (S_{\mathrm{TL}}/S_{\mathrm{PWS}}) \cdot E_\lambda(\mathrm{PWS}), \quad (14)$$

where:

E_λ(TL), spectral irradiance of a test lamp,

f, linearity-range factor correction,

$S_{\mathrm{TL}}/S_{\mathrm{PWS}}$, signal ratio of the test lamp-primary working standard comparison,

E_λ(PWS), spectral irradiance of a primary working standard.

Table 2. Radiance to irradiance transfer uncertainty (3σ) in percent

	Wavelength (nm)							
Source of error	250	350	654.6	900	1300	1600	2000	2400
$S_{\mathrm{PWS}}/S_{\mathrm{ISS}}$ (r)	0.42	0.08	0.06	0.84	0.86	1.46	2.60	5.73
f (s)	0.26	0.19	0.10	0.07	0.05	0.04	0.03	0.03
m (s)	0.10	0.10	0.10	0.10	0.10	0.10	0.10	0.10
d_1 (s)	0.10	0.10	0.10	0.10	0.10	0.10	0.10	0.10
λ (r)	0.02	0.02	0.02	0.02	0.02	0.02	0.02	0.02
Lamp currents:								
ISS (r)	0.08	0.06	0.03	0.02	0.02	0.01	0.01	0.01
PWS (r)	0.08	0.06	0.03	0.02	0.02	0.01	0.01	0.01
Geom. Factor (s)	0.20	0.20	0.20	0.20	0.20	0.20	0.20	0.20
Spec. Scat. (s)	0.05	0.05	0.05	0.05	0.05	0.05	0.05	0.05
Stray Light (s)	0.02	0.02	0.02	0.02	0.02	0.02	0.02	0.02
Av. Sph. Resp. (s)	0.01	0.01	0.01	0.01	0.01	0.01	0.01	0.01
Systematic error	0.36	0.31	0.27	0.26	0.26	0.25	0.25	0.25
Random error	0.43	0.11	0.08	0.84	0.86	1.46	2.60	5.73
Quadrature sum	0.57	0.33	0.28	0.88	0.90	1.48	2.61	5.74

Notes: Random errors denoted by (r), systematic errors by (s).
Sources of error described in section 8.2.

In addition to the factors which appear explicitly in eq (14), uncertainties in the ratio S_{TL}/S_{PWS} arise from errors in the wavelength settings and in the electrical current measurements of the sources. All these uncertainties have been evaluated and are listed in table 3.

8.4 Overall Uncertainty of the Primary Working Standards

Table 4 lists the overall uncertainties of the primary working standards. It is made up by combining the results of tables 1 and 2. The differences between lines 1a and 1b (and between 3a and 3b) are caused by the systematic uncertainty introduced by an assumed uncertainty of 0.4 K in the gold-point temperature.

8.5 Overall Uncertainty of a Group of Test Lamps

Table 5 lists the overall uncertainties of a group of test lamps. It is made up by combining the results of tables 1, 2, and 3 and adding a model error. The model error is necessary because the primary working standards drift with time. A time drift model is applied for each of the primary working standards [see eq (10)] but the possibility that this drift may be wrong introduces an additional uncertainty in table 5, but not included in table 2 or table 4. This uncertainty was obtained by comparing the calculated extrapolated spectral irradiance with further scale realizations. When the primary working standards are used between scale realizations, this additional uncertainty must be combined in quadrature with the other uncertainties.

Table 3. Test lamp irradiance transfer uncertainty (3σ) in percent

	Wavelength (nm)							
Source of error	250	350	654.6	900	1300	1600	2000	2400
S_{TL}/S_{PWS} (r)	0.87	0.21	0.15	0.42	0.68	0.72	1.59	2.60
f (s)	0.01	0.01	0.01	0.01	0.01	0.01	0.01	0.01
Lamp currents:								
PWS (r)	0.08	0.06	0.03	0.02	0.02	0.01	0.01	0.01
TL (r)	0.08	0.06	0.03	0.02	0.02	0.01	0.01	0.01
Systematic error	0.01	0.01	0.01	0.01	0.01	0.01	0.01	0.01
Random error	0.88	0.22	0.16	0.42	0.68	0.72	1.59	2.60
Quadrature sum	0.88	0.22	0.16	0.42	0.68	0.72	1.59	2.60

Notes: Random errors denoted by (r), systematic errors by (s).
Sources of error described in section 8.3.

Table 4. 1986 spectral irradiance scale uncertainty (3σ) in percent (derived from tables 1 and 2)

	250 nm	350 nm	654.6 nm	900 nm	1300 nm	1600 nm	2000 nm	2400 nm
1. NBS spectral radiance scale								
a. Absolute error (with respect to SI units)	1.41	1.01	0.55	0.49	0.41	0.44	0.70	1.16
b. NBS long term reproducibility (without T_{AU}, see table 1)	0.58	0.42	0.25	0.34	0.33	0.39	0.69	1.15
2. Radiance to irradiance transfer								
a. Systematic errors	0.36	0.31	0.27	0.26	0.26	0.25	0.25	0.25
b. Random errors (3σ precision)	0.43	0.11	0.08	0.84	0.86	1.46	2.60	5.73
3. Spectral irradiance scale uncertainty (quadrature sum)								
a. With respect to SI units	1.52	1.06	0.62	1.01	0.99	1.55	2.71	5.85
b. NBS long term reproducibility	0.81	0.53	0.38	0.94	0.96	1.53	2.70	5.85

Table 5. 1986 spectral irradiance scale transfer uncertainty (3σ) in percent (derived from tables 1, 2, and 3)

	250 nm	350 nm	654.6 nm	900 nm	1300 nm	1600 nm	2000 nm	2400 nm
1. NBS spectral radiance scale								
a. Absolute error (with respect to SI units)	1.41	1.01	0.55	0.49	0.41	0.44	0.70	1.16
b. NBS long term reproducibility	0.58	0.42	0.25	0.34	0.33	0.39	0.69	1.15
2. Radiance to irradiance transfer								
a. Systematic errors	0.36	0.31	0.27	0.26	0.26	0.25	0.25	0.25
b. Random errors (3σ precision)	0.43	0.11	0.08	0.84	0.86	1.46	2.60	5.73
c. Model error	1.38	0.80	0.78	0.77	0.77	0.82	1.00	1.20
3. Test lamp irradiance transfer								
a. Systematic errors	0.01	0.01	0.01	0.01	0.01	0.01	0.01	0.01
b. Random errors (3σ precision)	0.88	0.22	0.16	0.42	0.68	0.72	1.59	2.60
4. Uncertainty of reported values (quadrature sum)								
a. With respect to SI units	2.23	1.35	1.01	1.34	1.42	1.89	3.29	6.51
b. NBS long term reproducibility	1.83	0.99	0.88	1.29	1.40	1.88	3.29	6.51

The differences between lines 1a and 1b (and between 4a and 4b) are again caused by the systematic uncertainty introduced by an assumed uncertainty of 0.4 K in the gold-point temperature.

About the authors: James H. Walker, Robert D. Saunders, John K. Jackson, and Donald A. McSparron are members of the Radiometric Physics Division of the NBS Center for Radiation Research.

References

[1] Uriano, G. A., Garner, E. L., Kirby, R. K., and Reed, W. P., eds., NBS Calibration Services Users Guide 1986-88, Natl. Bur. Stand. (U.S.) Spec. Publ. 250 (July 1986).
[2] Stair, R., Schneider, W. E., and Jackson, J. K., A New Standard of Spectral Irradiance, Appl. Opt. 2, 1151-1154 (1963).
[3] Saunders, R. D., and Shumaker, J. B., The 1973 NBS Scale of Spectral Irradiance, Natl. Bur. Stand. (U.S.) Tech. Note 594-13 (Apr. 1977).
[4] Klose, J. Z., and Bridges, J. M., NBS Measurement Services: Radiometric Standards in the Vacuum Ultraviolet, Natl. Bur. Stand. (U.S.) Spec. Publ. 250-3 (June 1987).
[5] Walker, J. H., Saunders, R. D., Jackson, J. K. and McSparron, D. M., NBS Measurement Services: Spectral Irradiance Calibrations, Natl. Bur. Stand. (U.S.) Spec. Publ. 250-20 (Sept. 1987).
[6] Walker, J. H., Saunders, R. D., and Hattenburg, A. T., NBS Measurement Services: Spectral Radiance Calibrations, Natl. Bur. Stand. (U.S.) Spec. Publ. 250-1 (January 1987). Also see by same authors, The NBS Scale of Spectral Radiance, Metrologia 24 (to be published 1987).
[7] Waters, W. R., Walker, J. H., and Hattenburg, A. T., NBS Measurement Services: Radiance Temperature Calibrations, Natl. Bur. Stand. (U.S.) Spec. Publ. 250-7 (Oct. 1987). Also see by same authors, The NBS Scale of Radiance Temperature, J. Res. Natl. Bur. Stand., 92, 17 (1987).
[8] NBS Optical Radiation News No. 18, November 1976.
[9] De Vos, J. C., Evaluation of the Quality of a Blackbody, Physica 20, 669-689 (1954).
[10] Kostkowski, H. J., Erminy, D. E., and Hattenburg, A. T., High Accuracy Spectral Radiance Calibration of Tungsten-Strip Lamps, Advances in Geophysics 14, New York, NY, Academic Press, Inc., 111-127 (1970).
[11] Wilkinson, F. J., Astigmatism Errors in Radiance Measurements, Metrologia 20, 11-18 (1984).
[12] Popenoe, C. H., and Campbell, M. S., MIDAS Modular Interactive Data Acquisition System—Description and Specification, Natl. Bur. Stand. (U.S.) Tech. Note 790, (Aug. 1973).
[13] Kostkowski, H. J., The Relative Spectral Responsivity and Slit-Scattering Function of a Spectroradiometer, Chapter 7 of Self-Study Manual on Optical Radiation Measurements: Part I—Concepts, Natl. Bur. Stand. (U.S.) Tech. Note 910-4, 2-34 (June 1979).
[14] Saunders, R. D., and Shumaker, J. B., Apparatus Function of a Prism-Grating Double Monochromator. (submitted to Applied Optics.)
[15] Saunders, R. D., and Shumaker, J. B., Automated Radiometric Linearity Tester, Appl. Opt. 23, 3504-3506 (1984).
[16] Coslovi, L., and Righini, F., Fast Determination of the Nonlinearity of Photodetectors, Appl. Opt. 19, 3200-3203 (1980).
[17] The International Practical Temperature Scale of 1968, Metrologia 5, 35-44 (1969).
[18] Weidner, V. R., and Hsia, J. J., Reflection Properties of Pressed Polytetrafluoroethylene Powder, J. Opt. Soc. Amer. 71 (1981).
[19] Saunders, R. D., and Ott, W. R., Spectral Irradiance Measurements: Effect of UV Produced Fluorescence in Integrating Spheres, Appl. Opt. 15, 827 (1976).
[20] Kostkowski, H. J., and Nicodemus, F. E., An Introduction to the Measurement Equation, Chapter 5 of Self-Study Manual on Optical Radiation Measurements: Part I—Concepts, Natl. Bur. Stand. (U.S.) Tech. Note 910-2, 58-92 (Feb. 1978).

Volume 93, Number 1, January–February 1988
Journal of Research of the National Bureau of Standards

Radiometric Calibrations of Portable Sources in the Vacuum Ultraviolet

Volume 93 Number 1 January–February 1988

Jules Z. Klose, J. Mervin Bridges, and William R. Ott

National Bureau of Standards
Gaithersburg, MD 20899

The radiometric calibration program carried out by the vacuum ultraviolet radiometry group in the Atomic and Plasma Radiation Division of the National Bureau of Standards is presented in brief. Descriptions are given of the primary standards, which are the hydrogen arc and the blackbody line arc, and the secondary standards, which are the argon mini- and maxi-arcs and the deuterium arc lamp. The calibration methods involving both spectral radiance and irradiance are then discussed along with their uncertainties. Finally, the calibration services are delineated in an appendix.

Key words: arc (argon); arc (blackbody); arc (hydrogen); irradiance; lamp (deuterium); radiance; radiometry; Standards (radiometric); ultraviolet; vacuum ultraviolet.

Accepted: October 2, 1987

1. Introduction

The vacuum ultraviolet (VUV) region of the spectrum has become important in several areas of research and development. These include space-based astronomy and astrophysics, thermonuclear fusion research, ultraviolet laser development, and general atomic physics research. Applications of VUV radiation in chemical, biophysical, and medical fields are widespread. Many applications require knowledge of not only the wavelength of the radiation involved but also the intensity or flux of radiation. This implies a calibration of some type. The calibration may be based upon a standard source, i.e., one whose output is known, or a standard detector, i.e., one whose response to a given radiation level is known. Two general cases can be distinguished. In the first case one wishes to determine how much radiation a source such as the sun or a plasma device is emitting at a given wavelength. Usually, the source is not monochromatic, so a monochromator must be used to select the desired wavelength. In this case the most direct procedure is to employ a standard source. The source to be investigated as well as the standard source are set up in turn so that radiation from each source passes through the same monochromator and optical elements. The calibration is performed essentially by a direct substitution of the standard source for the one to be calibrated.

The second case occurs when one wishes to know the flux in a monochromatic beam of radiation, such as the flux emerging from the exit slit of a monochromator. For this determination a standard detector is more appropriate; the flux is determined by simply measuring the signal when the detector is irradiated with the beam to be calibrated. If one were to attempt to perform the calibration in the first case above using a standard detector or in the second case using a standard source, one would in both cases need to know the spectral efficiency of the monochromator used in the measurement. This would require an additional measurement using a second monochromator and

would introduce additional uncertainties and complexities. Therefore, a need exists for both standard sources and standard detectors.

Standard sources may be divided into primary standards and secondary or transfer standards. Primary standards are ones whose output is known from basic principles. The primary standards of VUV radiation include plasma sources, especially the wall-stabilized hydrogen and blackbody line arcs, and electron storage rings emitting synchrotron radiation.

There are storage rings at several laboratories, including NBS, which are used as primary VUV radiation standard sources. They produce highly-polarized continuum radiation for wavelengths $\gtrsim$0.03 nm. Limited access to storage rings and problems with the emitted polarized light, however, make it desirable to have available other standard VUV sources. The wall-stabilized hydrogen and blackbody line arcs were developed to provide alternative primary standard sources. These sources, however, are also not able to be easily used for calibrations. Hence, secondary or transfer standards which are relatively easy to apply have been developed. These include the deuterium lamp and the argon mini-arc. These sources are more readily available and make possible relatively inexpensive and convenient calibrations. Also for researchers having access to a storage ring, the secondary standards are useful in making possible more frequent calibrations. Finally, the secondary standards possess some useful properties not characteristic of the available primary standards such as, for example, emission over a relatively large solid angle.

The two principal radiometric quantities which are measured and calibrated are *radiance* and *irradiance*. For an object or source which emits radiation, the *radiance* is the radiant power emitted per area per solid angle, $L=(\mathrm{W\,cm^{-2}\,sr^{-1}})$. If the source emits a continuum, i.e., emits radiation at all wavelengths near a particular wavelength, the *spectral radiance* is the radiance per wavelength interval or bandpass, $L_\lambda=(\mathrm{W\,cm^{-2}\,sr^{-1}\,nm^{-1}})$. The radiance will in general vary over the source area, the direction, and the wavelength. The definition assumes that the area, solid angle, and wavelength band are small enough that the radiance does not vary greatly within these quantities. Irradiance is the radiant power incident upon a target per area, $E=(\mathrm{W\,cm^{-2}})$, and *spectral irradiance* is the radiant power incident upon a target per area per wavelength band, $E_\lambda=(\mathrm{W\,cm^{-2}\,nm^{-1}})$. A source of radiation may serve as a standard source of irradiance by operating it at a given distance from the target area. Some sources may be used as either standard radiance or standard irradiance sources. A separate calibration must be performed, however, for each quantity.

The services performed by the Atomic and Plasma Radiation Division of the National Bureau of Standards include tests and calibrations of portable secondary VUV standard radiance and irradiance sources. These are usually rare-gas dimer lamps, which emit continuum radiation over limited wavelength ranges, and hollow cathode lamps, which emit spectral lines in the wavelength range from the VUV through the visible. All sources are generally supplied by customers. The main groups of customers have included those in the fields of space-based astronomy and solar physics who have used standard sources to calibrate satellite, rocket, or balloon-borne spectrometers. Other customers have needed calibrations in the 100–300 nm range for plasma radiation studies.

2. Apparatus

2.1 Primary Standards

2.1.1 The Hydrogen Arc A high temperature wall-stabilized steady-state hydrogen arc has been developed as our primary standard of spectral radiance [1]. This type of arc lends itself to such a use because at sufficiently high temperatures it yields absolute intensities independent of other radiometric standards or of the accuracy of any plasma diagnostics. Previous efforts at lower powers were hindered by large uncertainties in plasma diagnostics, a difficulty that has been overcome in the high temperature arc. Figure 1 illustrates the UV spectrum of several of the more common standard sources, including that part of the hydrogen arc spectrum that is the subject of this paper.

The method depends upon the phenomenon that the continuum emission coefficient for a strongly ionized hydrogen plasma which is in or close to the condition of local thermodynamic equilibrium (LTE) is calculable to within one percent [2]. This follows from the fact that the essential spectroscopic constants, i.e., the continuum absorption coefficients and transition probabilities, are exactly known for atomic hydrogen. The continuum intensities emitted from a typical pure hydrogen wall-stabilized arc discharge in the spectral region above 91.5 nm are optically thin and a function of the electron density and temperature [3,4]. In the low power hydrogen arc the electron density

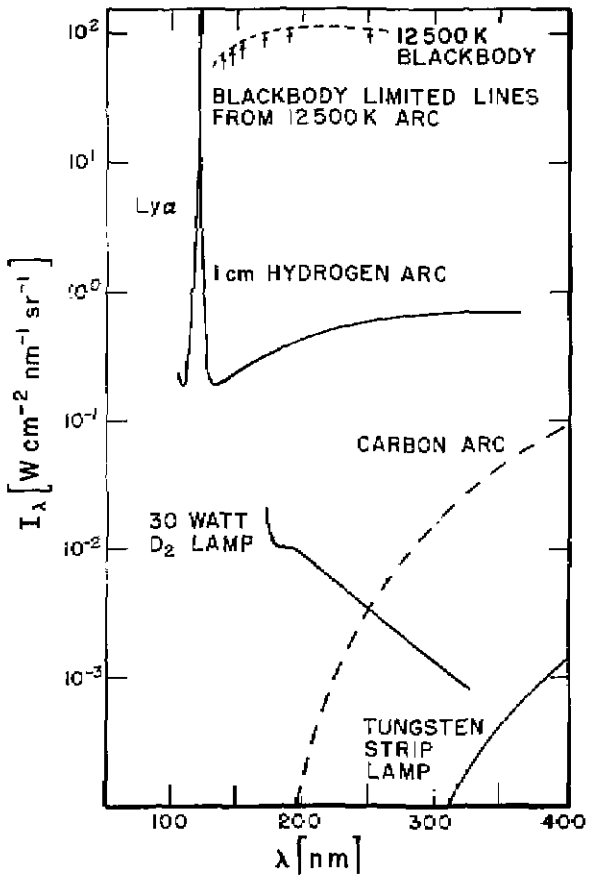

Figure 1. Comparisons of spectral radiances for far UV sources. The output of the hydrogen arc is given for the temperature of maximum continuum emission; the outputs of the other sources are at typical operating conditions.

and temperature are determined from plasma diagnostics in the visible spectral region using available radiometric standards [3]. These quantities are then used to calculate the continuum intensities in the VUV. There are known to be significant uncertainties in the plasma diagnostics, and as a result we have adopted as our primary standard a higher power hydrogen arc which operates such that a 2-mm diameter wall-stabilized discharge reaches a temperature of about 20,000 K. For these conditions the continuum emission coefficient as a function of temperature shows a broad maximum which shifts with wavelength as is shown in figure 2. This optimum condition is brought about essentially by the compensating effects of an increase in the ionization fraction and a decrease in the total number density as the temperature is increased in a constant 1-atm pressure operating environment. Beyond this maximum [5,6] the ionization is practically complete, and any further increase in arc temperature results only in a gradual decrease in intensity because of the decrease in the number density. The weak wavelength dependence of this maximum seen in figure 2 occurs because of the change in the energy distribution of the equilibrated electrons as the electron temperature is varied.

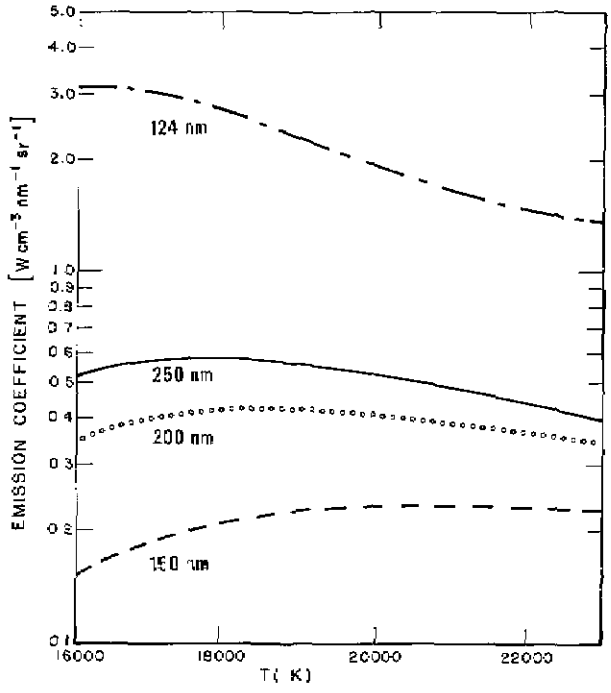

Figure 2. The emission coefficient for a 1-atm hydrogen plasma in LTE as a function of temperature for several wavelengths: 250 nm (——); 200 nm (oooo); 150 nm (- - - -); and 124 nm (— - — -).

Figure 3 shows the measured radial dependence of the hydrogen continuum emission coefficient at 190 nm and the corresponding calculated LTE temperature [2] for an arc current of 80 A. Because the maximum in the coefficient is broad and the absolute magnitude of the peak intensity is not very sensitive to the electron temperature, the emission characteristics of the plasma are nearly homogeneous over its central region which extends to about 0.6 mm from the arc axis. This is especially significant if only a small sample of the region is observed as indicated in the figure. First, it means that the alignment precision, which was responsible for much of the uncertainty in the low power arc method, is not critical here. Second, it means that the arc current necessary to obtain the maximum emission coefficient is also not critical.

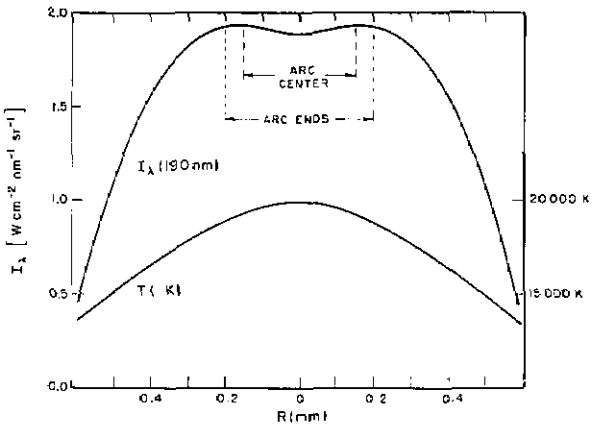

Figure 3. Radial dependence of the continuum intensity and arc temperature for a 2-mm wall-stabilized hydrogen arc operating at 80 A. The dashed lines define the dimensions of the plasma that is observed by spectrometers.

Additional advantages of operating the hydrogen arc under such conditions are (1) the H_2 Lyman band molecular emission, which limited the low power hydrogen arc to wavelengths longer than 165 nm, is negligible; (2) the assumption of LTE appears to be very closely fulfilled as shown by experimental consistency checks and theoretical validity criteria [7]; and (3) the hydrogen arc as it is described here constitutes a true primary standard of spectral radiance in that except for the minor uncertainties associated with the theoretical model for the plasma, knowledge of the absolute continuum intensities does not depend on any other standards of calibration or sophisticated plasma diagnostics and requires only a measurement of the ambient pressure ($\approx$1 atm) and the arc length. The procedure for applying the arc as a radiometric standard involves only adjusting the arc current for maximum signal at the wavelength of interest. The overall system efficiency is given then by the ratio of the detector response to the hydrogen arc spectral radiance calculated using the maximum LTE emission coefficient at 1-atm pressure and the actual physical length of the discharge.

Figure 1 shows the wavelength dependence of the maximum emission coefficient of the hydrogen arc plasma, and table 1 lists the values of the same quantity obtained through a calculation of the hydrogen continuum [2]. The Stark broadened wing of the Lyman α line at 122 nm has been included in these calculations and, as can be seen from the table, becomes significant at wavelengths below 140 nm [8]. The uncertainty in the calculated continuum emission coefficient is estimated to be about 2%, due mostly to uncertainties in the high density plasma corrections [2]. Combining this uncertainty in quadrature with the uncertainties in the Stark broadening calculations, the uncertainty in the total emission coefficient comes out to be 2% above 140 nm, 8% at 130 nm, and 13% at 124 nm. These uncertainties and all those succeeding unless stated otherwise are taken to be 2 standard deviations (2σ), i.e., as having a confidence limit of about 95%.

Table 1. Maximum emission coefficient from a 1-atm hydrogen plasma in LTE calculated as a function of wavelength[a]

λ(nm)	ϵ(W cm^{-3} nm^{-1} sr^{-1})	T(K)	$\frac{\text{Ly }\alpha}{\epsilon}$ (%)
350	0.73	17,000	0
300	0.68	17,000	0
250	0.59	17,500	0.01
200	0.424	18,500	0.07
190	0.386	18,800	0.11
180	0.347	19,200	0.20
170	0.308	19,500	0.34
160	0.269	20,000	0.65
150	0.232	21,000	1.3
140	0.200	21,700	4
130	0.245	17,500	54
128	0.372	16,500	77
126	0.79	16,500	90
124	3.22	16,000	98

[a] The percentage of this emission due to Ly α and the arc temperature required for maximum emission are also listed.

Three factors are of special concern in applying the high power hydrogen arc standard: the arc length, spatial resolution, and off-axis H_2 emission. Figure 4 is a schematic of the hydrogen arc [1,4,9]. The arc is struck between a set of four tungsten anodes and four tungsten cathodes that are symmetrically located and share the current load equally. At each end of the 2-mm diameter channel formed by the 20 water-cooled stacked copper plates, the discharge expands and separates into four smaller arcs terminating at each of the electrode tips. The length of this inhomogeneous region is made small compared to the total length of the arc, and the emission coefficient and temperatures are lower than in the channel. Therefore, its contribution to the total arc signal obtained in an end-on measurement along the axis of the discharge is small but not precisely known. The minimum possible length of the arc is 5.05 cm, the total length of the channel formed by the 20 arc plates, and the maximum length is 5.5 cm, the total distance between the electrodes. The estimated length

of the homogeneous hydrogen arc plasma was thus taken to be 5.3 cm with an uncertainty of 5% (2σ).

Spatial resolution is not much of a problem for the high power arc since the emission characteristics are nearly uniform in the vicinity of the arc axis. The regions of the arc that fall into the cone of observation determined by the f/200 aperture and the 0.30 mm field stop of the observing optics are illustrated in figure 3. Thus, knowledge of the emission coefficient as a function of radial position allows the calculation of the effect of spatial averaging. The main result is that the integrated emission coefficient $\bar{\epsilon}$ has a maximum about 1% lower than ϵ_{max} from a truly homogeneous plasma with an axis temperature $T(\bar{\epsilon})$ slightly higher than $T(\epsilon_{max})$. The arc plasma is cylindrically symmetric, and because the area of the differential shells increases as $2\pi r\Delta r$, the off axis regions are weighted more than the axis region. Therefore, when one obtains maximum signal, the current has been adjusted so that the temperature maximum occurs slightly off-axis as seen in figure 3.

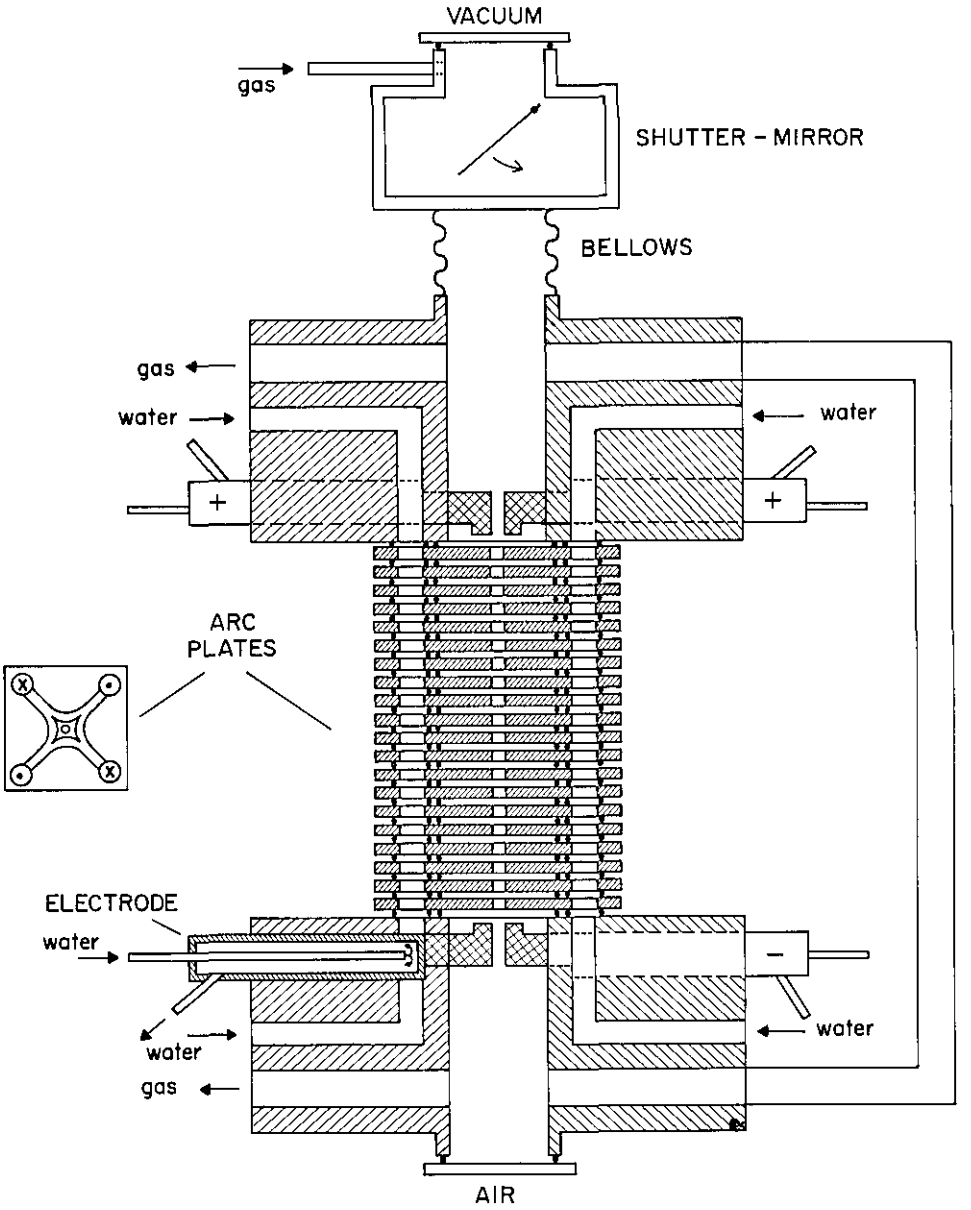

Figure 4. Schematic of the hydrogen wall-stabilized arc. A cutaway top view drawing of one of the arc plates illustrates the flow of cooling water through specially machined channels within each plate. The symbols in the four corners show the direction of water flow.

Below 165 nm the Lyman bands of H_2 are emitted from low temperature off-axis regions. Figure 5 shows a radial scan of the arc at a wavelength where one of the stronger H_2 features can be observed. The off-axis line peak is about 100 times larger than the on-axis hydrogen continuum, but clearly if the observation column is restricted to no more than the central 0.5 mm diameter plasma, H_2 lines should not be observed. Molecular emission from the inhomogeneous end regions also is a possibility. However, none is observed since the arc terminates at points that are out of the line of observation (the cooler plasma regions are off-axis) and the end-layer on-axis temperature gradient is quite sharp (the length of the cool plasma is therefore very short).

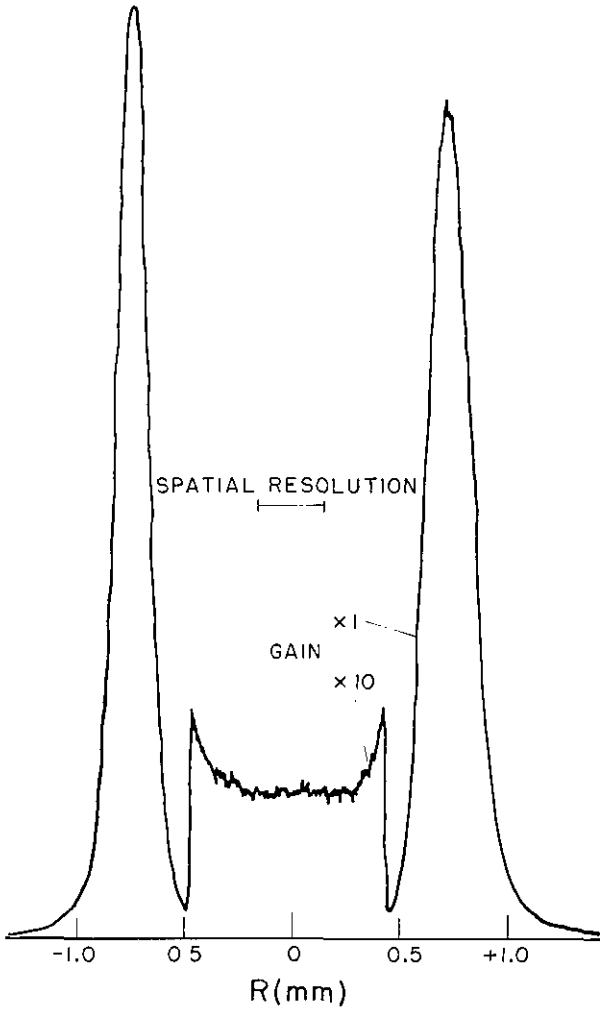

Figure 5. The radial dependence of the hydrogen arc spectral radiance at 160.6 nm for an arc axis temperature of about 19,500 K. The intense off-axis radiation is due to Lyman band molecular emission. The nearly uniform radiation in the vicinity of the axis contains no molecular contributions, but is due to the hydrogen continuum that is being used as a spectral radiance standard.

In figure 6 the calculated spectral radiance of the high power hydrogen arc is compared with calibrations of that arc made with several other standard sources [1]. The theoretical spectral radiance is the product of the theoretical maximum hydrogen plasma emission coefficient and the arc length. This quantity is graphed as a shaded area which represents the rms uncertainty due to the previously described uncertainties in both the calculated emission coefficient and the arc length. The solid and open circles represent the measured continuum intensities using, respectively, a calibrated tungsten strip lamp [10] and blackbody limited lines from another arc for spectral radiance normalization. The crosses represent the measured intensities using the low power hydrogen-arc standard. The error bars attached to the data points represent uncertainties associated not with the hydrogen arc but with the various standards used to calibrate the spectral radiance. The discontinuity in the wavelength scale is due to the interruption of the hydrogen spectrum by the Balmer line series of atomic hydrogen, which dominates the high temperature arc spectrum above 360 nm except for a small region around 560 nm between H_α and H_β. Inspection of figure 6 leads us to conclude that the various standards are consistent with one another over the entire range of comparison.

In summary, a high power atmospheric pressure hydrogen arc capable of operating at temperatures on the order of 20,000 K has been examined theoretically and experimentally and found to be suitable as a primary radiometric standard in the VUV. The experimental investigations have shown that at such temperatures molecular hydrogen emission at wavelengths shorter than 165 nm is negligible, and the hydrogen plasma continuum emission coefficient can be measured throughout the 124–360 nm spectral range. By operating the arc at currents such that the maximum emission coefficient is reached, the uncertainties associated with various plasma diagnostics and alignment imprecisions are minimized to the one-percent range. The results of a comparison with other available standard sources are consistent with the estimated 2σ uncertainty of $\pm 5\%$ in the hydrogen arc spectral radiance between 140 and 360 nm. This uncertainty is due mainly to the uncertainty in the measurement of the arc length. Below 140 nm the Lyman α Stark broadened wing becomes significant, and the estimated uncertainty in the hydrogen arc intensities increases to about $\pm 9\%$ at 130 nm and $\pm 14\%$ at 124 nm due mainly to uncertainties in the plasma line broadening theory. These results are also

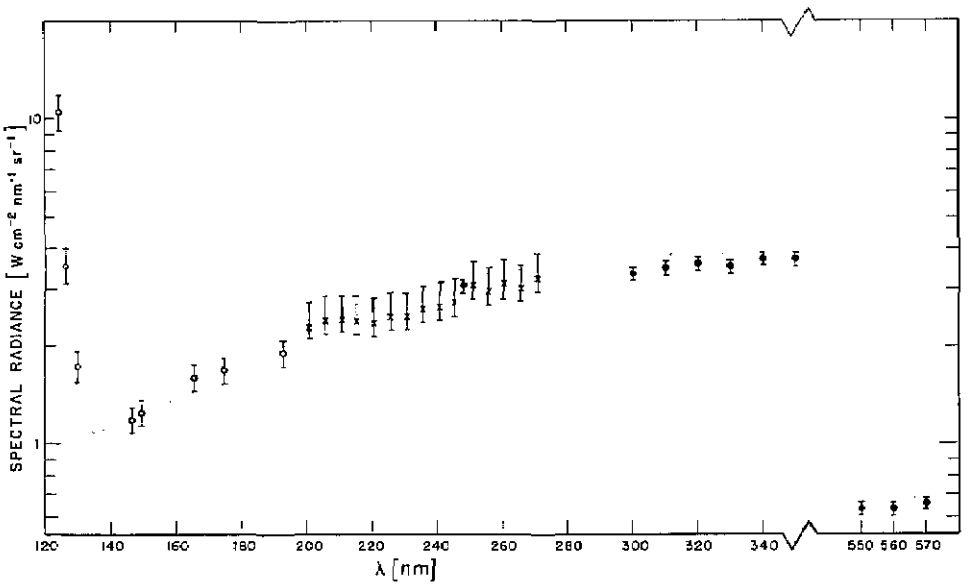

Figure 6. Maximum spectral radiance vs wavelength calculated for a 5.3-cm length hydrogen arc plasma in LTE at 1 atm pressure. The calculation is shown as a grid and represents the rms uncertainty due to uncertainties in the arc length (±5%) and the calculated emission coefficient (between 2% and 13%). The points are actual measurements of the spectral radiance calibrated either with a tungsten strip lamp (·), blackbody limited lines (o), or a low power hydrogen arc (×).

consistent with a comparison standard. Finally, all experimental comparison data confirm that the hydrogen arc spectral radiance is calculable throughout the 124–360 nm range without dependence on any other radiometric standard or plasma diagnostic technique. Therefore, the high power hydrogen arc is a true primary standard. A detailed description of the hydrogen arc is given elsewhere [4].

2.1.2 Blackbody Line Arc The short wavelength limit of the hydrogen arc at about 124 nm is determined by the onset of the Stark-broadened, optically thick Lyman line series of atomic hydrogen that dominates the spectrum between 94 and 124 nm. Since the short wavelength cutoff of magnesium fluoride windows which are used in many VUV instruments is at about 115 nm, it would be convenient to have a primary standard which covers the range 115 to 124 nm. This need has been met with the development of the blackbody line arc [11–13].

Blackbody radiances for a number of prominent ultraviolet spectral lines are determined in the following manner. A wall-stabilized steady-state arc source is operated at about 12,000 K in argon with small admixtures of oxygen, nitrogen, and carbon dioxide. The admixtures produce very strong emission for their principal resonance lines, which all happen to lie conveniently in the wavelength range from 115 to 250 nm. These extremely strong resonance lines reach the blackbody intensity limits even at very small concentrations of the elements in the plasma, i.e., they become "optically thick." More precisely, the central regions of these line profiles reach, for a small wavelength range of a few hundreths of a nanometer, the intensity a blackbody would have at the arc temperature. Thus, the arc represents, for a few narrow wavelength bands in the UV spectrum, a very high temperature blackbody. To utilize this arc as a standard source, the temperature must be accurately determined using standard plasma spectroscopic techniques including absolute radiometry in the visible region of the spectrum. Subsequently, using Planck's radiation law, absolute intensities are established for these narrow spectral bands and are utilized as calibration points. Calibrations at other wavelengths are usually found by interpolation.

This technique has been used in a number of experiments and has been found to be reliable, with uncertainties ranging from about 10% at 250 nm to about 25% at 115 nm. For general use, however, it has the significant deficiency that large areas of the far UV have to be covered by interpolation since very few blackbody limited lines are found outside the ranges 115 to 126 nm and 146 to 175 nm. Since we are primarily interested in the range 115 to 124 nm, this is no great handicap here.

The accuracy of the blackbody line method depends critically on the measurement of the arc temperature, which is applied in the Planck function to determine the intensity of the blackbody ceilings of the optically thick resonance lines. It has been estimated that no single spectroscopic method is sufficient to determine the temperature of such a plasma with small O_2, N_2, and CO_2 additions to within an uncertainty of $\pm 2\%$ [11]. This represents an uncertainty in the blackbody ceiling of about 10% at 250 nm and about 25% at 115 nm as was mentioned above. To reduce this uncertainty, it was recommended that several methods be applied, and the results averaged. However, a single method, which is thought to be superior, was adopted here to determine the blackbody temperature.

The blackbody ceiling of the C I emission line at 247.9 nm is measured with a UV-calibrated tungsten strip lamp. The uncertainty in the spectral radiance of the strip lamps calibrated by NBS at this wavelength is about 2%. The peak of the 247.9 nm C I line is actually calibrated in two steps: first, the continuum emitted by the arc mixture at 250 nm is measured and calibrated at low spectral resolution using the tungsten strip lamp and the air-path predisperser and monochromator; and second, the peak of the carbon line is calibrated with respect to this continuum using the VUV instrument at high resolution. The difference in the VUV system efficiencies between 247.9 and 250 nm is minimal but is measured with the hydrogen arc and taken into account. Care is also taken to ensure that the contribution of the line wing at 250 nm in the low resolution air system is negligible. For a 4.7 nm diameter arc at 60 A the axis temperature of the argon plasma with admixtures of N, C, O, and H was measured to be 11,900 K. A temperature uncertainty of ± 160 K is estimated due to an estimated rms uncertainty of about 6% in the blackbody intensity determination at 247.9 nm. This results in an uncertainty of 10% in the blackbody line radiances between 115 and 140 nm.

Besides the temperature of the plasma, the character of the blackbody limited lines is also critical. For example, if the boundary layers between the mixed plasma and the pure argon buffer are too thick, the radiation transfer may be complicated by the density and temperature gradients through the layers. Such conditions are more the rule than exception and are easily detected at high resolution as structure in the line peaks. However, by appropriate flow rate adjustments, this effect can be minimized so that the blackbody plateaus are essentially flat-topped. Referring to figure 6, we see that for a high power hydrogen arc the calibrated spectral radiances obtained using blackbody limited lines are consistent with the corresponding calculated quantities, as was noted in section 2.1.1.

2.2 Secondary Standards

2.2.1 Argon Mini-Arc

Physical Principles After development of the hydrogen arc as a primary standard of radiance in the VUV, it was realized that a simpler, portable, more easily operated, and lower powered transfer standard would be of great value. The hydrogen arc is complicated and difficult to operate, and requires a massive highly stable dc power source rated at 1200 V and 110 A. A secondary standard which could be compared with our primary standard and then transported to the user's laboratory was recognized as being essential.

The most widely used transfer standard at that time was the commercially available deuterium lamp. Although the deuterium lamp has attractive properties such as its relatively strong continuum, low power requirements, and small size, it also has limitations. First, its region of applicability as a radiometric standard is restricted to wavelengths above 165 nm due to the presence of a many-line molecular deuterium band system below 165 nm. Second, the lamp exhibits a variability related to the positioning of the discharge on the electrodes following each ignition. Finally, the deuterium lamp has aging characteristics which are not well known. At the least, this means that the lamp must be frequently recalibrated to ensure accuracy.

To meet the lack of adequate transfer standards in the far UV, the argon mini-arc was developed at NBS [14]. This source can be conveniently applied as a radiometric transfer standard without the limitations of the deuterium lamp. The wavelength range of the argon mini-arc overlaps the lower range of the tungsten strip lamp in the near UV and extends beyond the short wavelength limit of the low pressure deuterium lamp at 165 nm. The mini-arc was designed to fulfill, insofar as possible, the following goals: 1) an intense line-free continuous spectrum between 115 and 330 nm; 2) stability and reproducibility over many hours of operation; 3) light source and power supply both portable; 4) uniform output over a large solid angle; 5) radiant power output adjustable over a range of several decades; and 6) simple alignment and operation. We now proceed to discussions of the arc construction and operating characteristics.

Description of the Arc Figure 7 is a photograph of the arc source. The model described here was designed specifically for use as a secondary radiance standard and is different in some respects from arc sources previously designed for other purposes. It was developed after experimentation as the simplest model which meets the requirements listed above. Argon was chosen as the operating gas because of its suitability in providing a stable discharge and an intense, line-free UV continuum with minimal power requirements. In the photograph the arc is mated to a monochromator with a stainless steel bellows. Water cooling connections and a triple-tube manifold for supplying argon are also shown. The two vertical threaded posts on the top of the arc are the electrical connections to the anode and cathode. The arc is mounted on an adjustable table which allows precise translation and rotation about two axes. All sources utilized in the NBS VUV radiometry program are mounted on this type of table.

As shown in figure 8, which is drawn to scale, the arc source is constructed essentially of five copper plates separated by silicone rubber insulating rings and clamped together to form the device. The central plate forms a channel which guides and constricts the discharge. The plates adjacent to the central plate contain the anode, a 3.2-mm diameter thoriated tungsten rod pressed into its plate, and the cathode, also of tungsten but mounted so that it can be moved into and out of the arc channel. The cathode was made adjustable for ease in igniting the arc. All five plates are water-cooled with the water flowing inside each piece through holes drilled in the sides. These holes are seen in the photograph but not in the diagram. The arc constricting section is 6.3 mm thick with a 4.0 mm diameter hole. Diameters smaller than this were considered unacceptable since they caused a higher plasma temperature and significant Ar II line emission in the wavelength region of interest. Larger diameters were rejected since the radiant power for a given current decreased considerably. The arc plasma is observed end-on through the holes in the electrode pieces, and the radiation calibrated is that emitted along the arc axis and emerging through the magnesium fluoride window on the cathode side. This window is set back to avoid possible contamination from the discharge. The gas purity necessary to maintain arc stability and reproducibility of the continuum emission is ensured by operating with a continuous flow of argon.

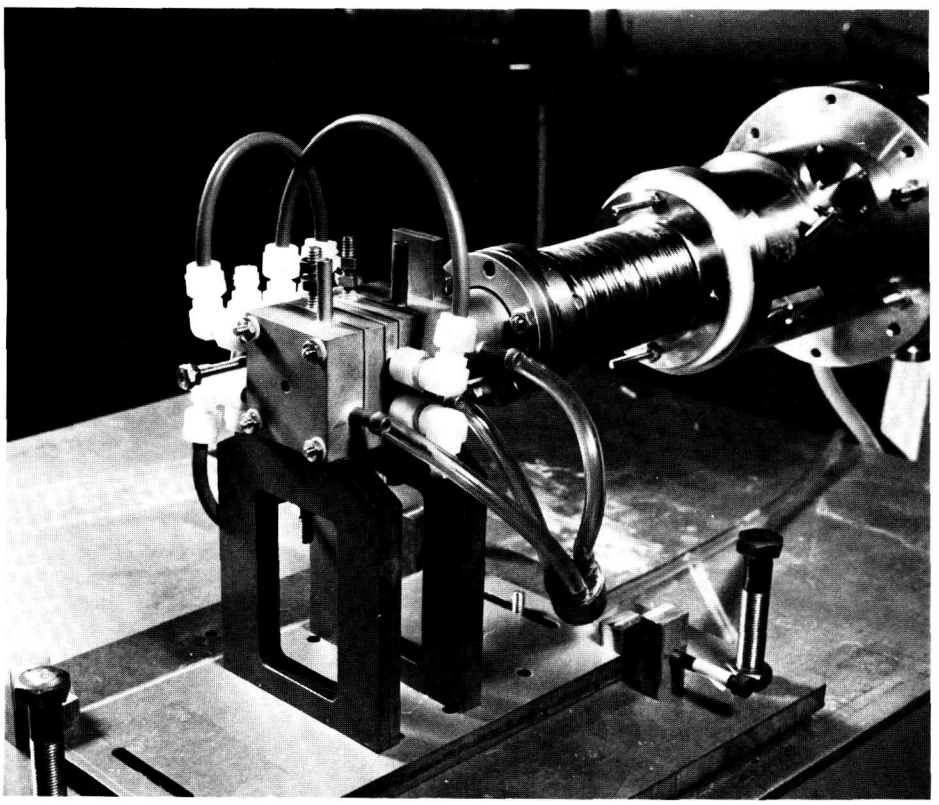

Figure 7. A photograph of the argon mini-arc mated to a monochromator.

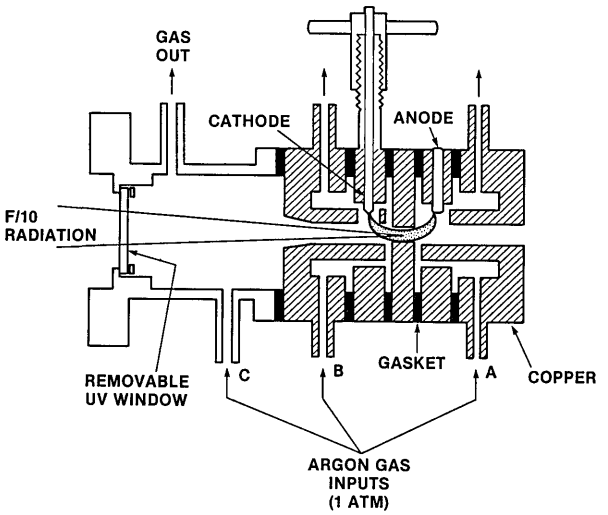

Figure 8. A schematic of the argon mini-arc light source.

Maintaining a high degree of argon purity within the arc chamber also minimizes the radiant power of atomic resonance lines in the spectrum which arise from small (ppm) concentrations of oxygen, nitrogen, carbon, and hydrogen. These elements are present due to air and water vapor in the arc chamber and gas handling system. The positions of the gas inlet and outlet ports are chosen to keep all sections of the arc chamber thoroughly purged. The argon is admitted to the inlet ports through plastic tubing connected to a flowmeter. Under the flow rate used here, the pressure in the chamber is unchanged from the ambient atmospheric pressure. The arc may be operated most conveniently with the outlet ports open and the data given below used to account for local and temporal differences in atmospheric pressure, if necessary.

Optical alignment can be performed by sighting with a telescope or laser beam down the arc axis. The distance for proper focus should be measured to the center of the middle copper piece.

The arc discharge is initiated by applying voltage between the electrodes and then inserting a tungsten rod, which is externally connected to the anode potential, until it touches the cathode protruding into the arc channel. The discharge is transferred from the tip of the rod to the anode as the rod is withdrawn. Finally, the cathode is withdrawn from the channel as shown in figure 8. Power for the discharge is furnished by a current regulated supply, the size of which is determined by the current required. For example, the power supply used in some of our experiments was a 1.2 kW, high efficiency switching regulator weighing only 10 kg. For starting the arc without difficulty, it was found necessary to use a ballast resistor of about 0.5 Ω in series and to apply a potential of at least 40 V. The arc can be started at currents above 10 A, and after ignition the resistor may be shorted out if desired. For currents above 10 A the voltage drop across the arc is nearly constant at 28 V.

Wall-stabilized arcs employed for end-on measurements usually are constructed of many constricting plates or disks, in order to obtain a nearly homogeneous plasma extending along the axis to the boundary regions near the electrodes at each end. These boundary regions emit a negligible part of the radiation emerging along the arc axis. The hydrogen and blackbody arcs which we use for primary radiance calibrations are necessarily of this type, since the lengths of the emitting plasma columns must be well defined. In such cases, however, the solid angle over which uniform radiation can be observed is small (f/200 is used for calibrations with the hydrogen and blackbody arcs) and not convenient for the calibration of many optical systems. For a transfer standard, on the other hand, the arc length does not need to be precisely known as long as it is a reproducible quantity. Thus, in order to provide a much greater solid angle, the argon mini-arc was made with only one constricting plate. Measurements show that this construction provides a rather large angular beam of radiation (f/10) having a practically uniform intensity distribution [14]. This should be considered an advantage even if one does not require such a large solid angle, since having the larger available angle makes the angular alignment of the mini-arc less critical.

Spectrum Figure 9 illustrates the spectral radiance of the argon mini-arc light source for two arc currents: 25.0 and 50.0 A. The continuous spectrum of the argon arc arises primarily from atomic recombination radiation. Near the short wavelength end the molecular continuum mentioned above contributes to some degree, and below 125 nm the increased output is from the wings of the argon resonance lines at 106.7 and 104.8 nm. Below the MgF_2 window cutoff, one should expect to have strong emission on the wings of the resonance lines with complete absorption at their centers. Below 80 nm there should be complete resonance continuum absorption by ground state argon atoms.

The spectral radiance was determined by direct comparison to the NBS wall-stabilized hydrogen arc [1] between 130 and 330 nm and to a plasma blackbody line radiator below 130 nm [1,3,11]. Data were taken with a spectral resolution of

0.01 nm. The temperature of the blackbody line radiator was determined to be 11,800±100 K by directly measuring the blackbody ceilings at 193, 174, 165, 149, and 146 nm, using the hydrogen arc as a primary standard of spectral radiance. With this temperature the radiant power of other blackbody limited lines emitted below 130 nm could then be calculated. For the calibration of longer wavelengths (>210 nm), the second-order spectrum from shorter wavelengths was eliminated by purging the small volume between the arc and the spectrometer with oxygen. Below 210 nm, argon was used as the purge gas.

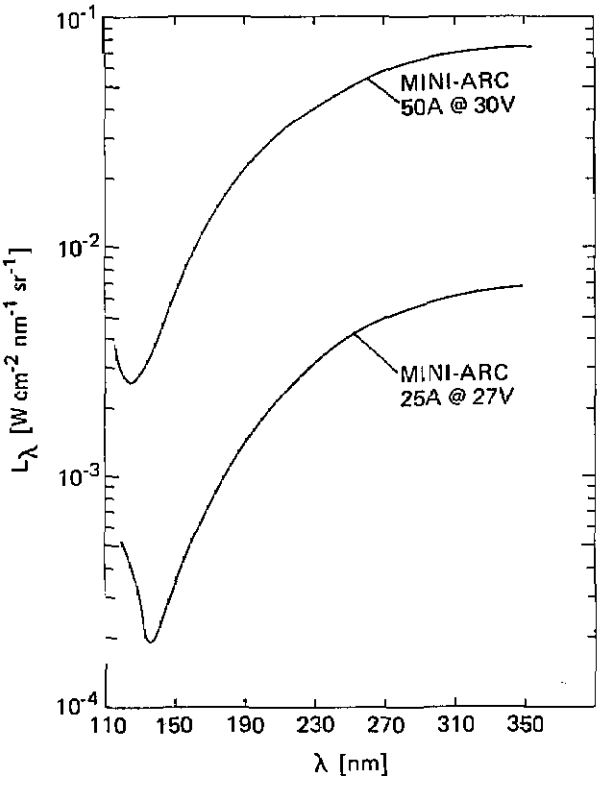

Figure 9. Spectral radiance as a function of wavelength for a mini-arc with an arc plate diameter of 4.0 mm operated at two different currents: 50.0 and 25.0 A.

The spectral radiance values illustrated in figure 9 and listed in table 2 apply to the plasma radiation emitted along the axis of the mini-arc which is imaged with a focusing mirror on a 0.30 mm diameter aperture (magnification = 1) at a solid angle f/200. The basic uncertainty in the spectral radiance is ±5% above 140 nm and ±10% below 140 nm due to uncertainties in the primary radiometric standards. Also included in table 2 for reference purposes is the measured transmission of the MgF_2 window used on the mini-arc. If one wishes to know the spectral radiance of the plasma itself, the figures in the table must be divided by the transmission. Known systematic deviations or uncertainties in the radiant power due to different operating or imaging conditions are described elsewhere [14].

Table 2. Spectral radiance as a function of wavelength for a 50.0-A argon mini-arc light source with an arc plate diameter of 4.0 mm[a]

λ(nm)	L_λ(mW cm^{-2} nm^{-1} sr^{-1})	T	λ(nm)	L_λ(mW cm^{-2} nm^{-1} sr^{-1})	T
330.5	70	0.945	198.0	26.6	0.900
325.5	70	0.943	192.5	24.0	0.900
320.5	69	0.942	191.0	23.5	0.894
315.5	69	0.942	186.0	20.8	0.891
310.5	68	0.941	181.0	18.4	0.883
305.5	67	0.940	176.0	16.1	0.873
300.5	66	0.939	173.5	15.0	0.870
295.5	64	0.939	170.0	13.6	0.860
290.5	63	0.938	166.5	11.8	0.850
285.5	62	0.938	165.0	11.1	0.848
280.5	60	0.938	162.0	9.9	0.840
275.5	58	0.938	159.5	9.3	0.826
270.5	57	0.937	157.0	8.3	0.810
265.5	55	0.937	155.0	7.8	0.798
260.5	54	0.937	153.5	7.3	0.785
255.5	52	0.935	151.0	6.5	0.765
250.5	50	0.933	148.5	5.9	0.740
245.5	48.1	0.932	147.0	5.4	0.724
240.5	45.2	0.931	144.0	4.73	0.700
235.5	43.3	0.928	139.5	3.81	0.672
230.5	40.9	0.925	135.0	3.38	0.655
225.5	39.1	0.922	129.5	2.77	0.662
220.5	36.3	0.920	127.0	2.65	0.642
215.5	34.6	0.917	123.5	2.54	0.626
210.5	32.4	0.914	118.5	2.77	0.597
205.5	30.3	0.910	116.0	3.34	0.530
200.5	27.9	0.900	114.5	3.74	0.439

[a] The measured transmission T of the arc window is also listed. The radiance of the plasma itself is obtained by calculating the quantity $L_\lambda T^{-1}$.

There are no Ar I lines in the spectrum between 114 and 330 nm. Below 200 nm there are several narrow Ar II lines and atomic nitrogen, carbon, and oxygen lines in the mini-arc spectrum due to air impurities in the argon gas (99.999% pure). In addition the hydrogen Lyman α line at 121.6 nm is present due to trace quantities of water vapor throughout the system. These impurity lines can be seen in figure 10 which is a photoelectric scan of the spectrum between 115 and 320 nm. The halfwidths of the lines are on the order of 0.01 nm, and the lines are well separated. Their presence has no significant influence on the ability to make absolute continuum measurements except when

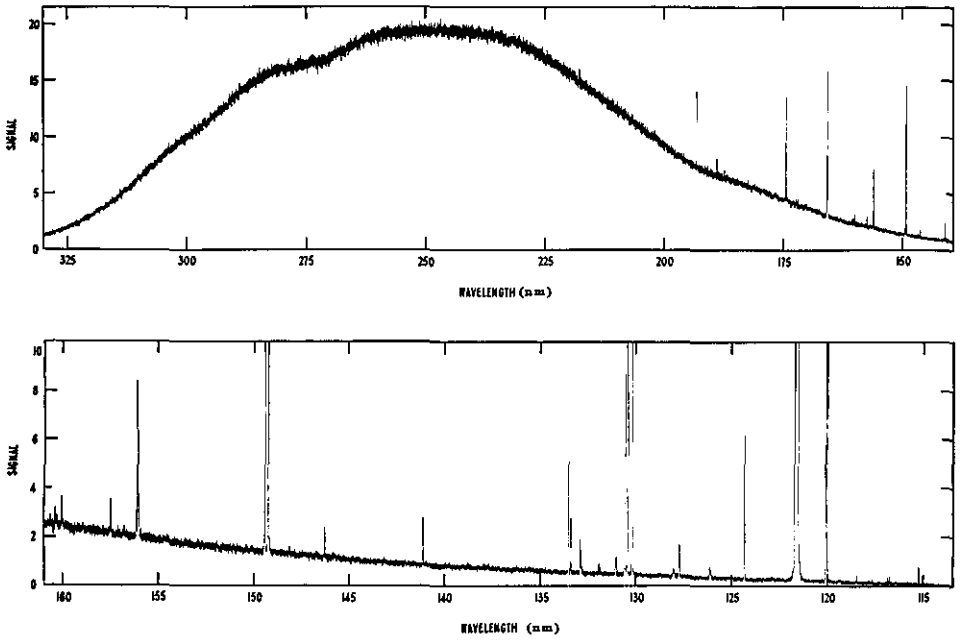

Figure 10. A photoelectric scan of the spectrum of the argon mini-arc between 115 and 320 nm, taken with a 0.01 nm spectral resolution and with a solar blind phototube detector.

extremely coarse wavelength resolution is used, as would be the case, for example, if the monochromator were replaced by relatively wideband filters. All lines observed in the spectrum are listed in table 3. From this list one may readily determine if, for a given wavelength and bandpass, one is free of lines. This precaution is necessary since the amount of trace impurities in the arc and the corresponding line intensities may vary somewhat from one system to another.

Figure 11 compares the spectrum of the mini-arc with several other light sources which have been applied as spectral radiance standards. Included in this figure is a representation of the spectra of the two primary standards, the hydrogen wall-stabilized arc and the blackbody line radiator, which were used to calibrate the mini-arc spectrum. The figure clearly illustrates the main advantages of the new transfer source. The mini-arc has substantially larger output and longer UV wavelength range than either the deuterium lamp or the tungsten strip lamp. Also, scattered visible light is not a significant factor, as it is when the tungsten lamp is used as a UV light source. The visible light from the argon arc is of the same order of magnitude as the near UV light, and there is less than a factor of 100 difference between the radiance at 110 and at 330 nm.

2.2.2 Argon Maxi Arc A recent advance in the arc standards program at NBS is the development of the argon maxi-arc. This source is essentially a high powered version of the mini-arc with three or four arc confining plates instead of one and power ratings of 5–10 kW instead of 1.5 kW. The maxi-arc with three plates has an irradiance approximately 30 times that of a mini-arc and was designed to enable calibrations to be performed at a level comparable to the solar irradiance in the near UV (250–350 nm). The discussion of the mini-arc given above generally applies also to maxi-arcs except for the powers and radiances. Figure 11 gives a comparison of the spectral radiance of the maxi-arc with that of several other UV primary and transfer standard sources. Several of these arcs have been supplied for use in calibration of space experiments.

2.2.3 Deuterium Arc Lamp

Introduction A source which has advantageous properties as a radiometric standard and is quite convenient to use is the molecular deuterium arc lamp [15]. This lamp has considerable UV radiant power, is light and compact, is low-powered (30 W), and with maximum radiant power at 190 nm has a very favorable ratio of UV to visible radiant power. This last fact is important in

Table 3. Survey of emission lines appearing in spectrum of mini-arc

λ(nm)	Identification	Radiance relative to continuum[a]
115.22	O I	1
116.79	N I	1
117.69	N I	0.3
118.94	C I	0.3
119.38	C I	1
119.99	N I	30
121.57	H I	100
124.33	N I	5
126.13	C I	2
127.75	C I	5
128.98	C I	1
130.22	O I	15
130.55	O I	10
131.07	N I	1
131.95	N I	0.5
132.93	C I	4
133.53	C II	8
135.58	C I	0.2
141.19	N I	0.7
143.19	C I	0.1
145.91	C I	0.1
146.33	C I	1
146.75	C I	0.1
148.18	C I	0.2
149.26	N I	4
149.47	N I	6
156.10	C I	4
157.50	Ar II	0.2
160.04	Ar II	0.2
160.35	Ar II	0.1
160.65	Ar II	0.05
165.72	C I	2
174.27	N I	1
174.53	N I	0.5
175.19	C I	0.1
187.31	Ar II	0.05
188.90	Ar II	0.1
193.09	C I	2
247.86	C I	0.05

[a] In column three are listed line radiances relative to the continuum, measured with 0.25-nm spectral resolution.

avoiding systematic errors due to visible scattered light effects when making measurements in the UV. Its disadvantages are that it is restricted to wavelengths above 165 nm due to the presence of a many-line molecular band system below 165 nm; it may exhibit a variability in the positioning of the discharge on the electrodes following each ignition; and its aging characteristics are not well known. On balance, however, the advantages of the deuterium lamp outweigh its disadvantages making it an essential component of any program of UV radiometry. The following discussion will describe the calibration of the deuterium lamp for spectral irradiance in the range 167–350 nm.

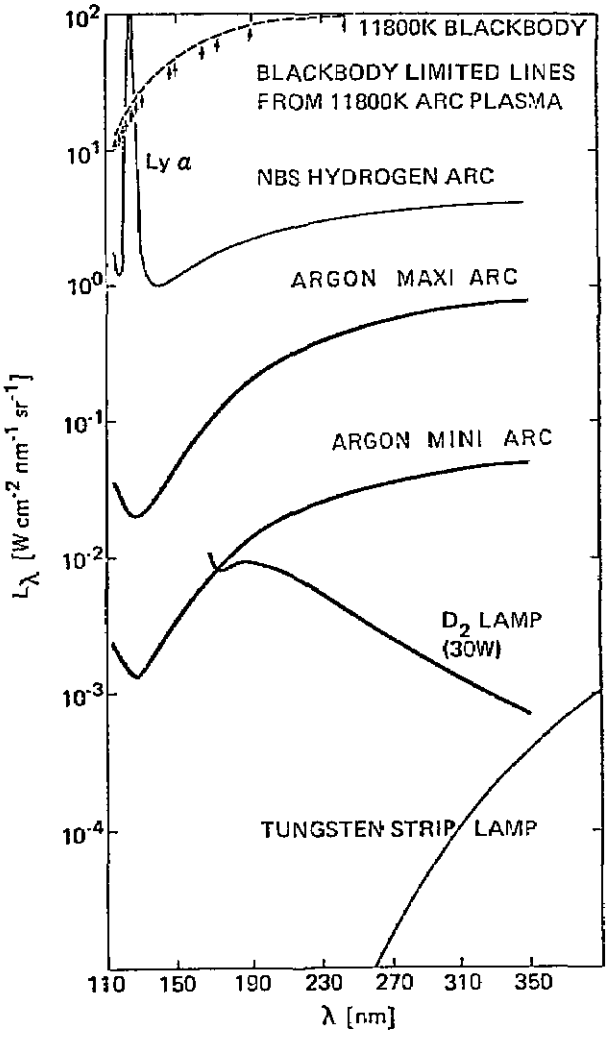

Figure 11. Comparison of the spectral radiance of several UV primary and transfer standard sources.

Discussion of the spectral radiance calibration of the deuterium lamp is not presented here since it is not a standard calibration service offered by NBS. However, this type of calibration can be requested under the category "Special Tests of Radiometric Devices in the Near and Vacuum Ultraviolet."

Description and Operation of the Lamp A schematic illustrating the operation of the deuterium lamp is shown in figure 12. In order to start the lamp, the cathode coil is first heated for 5 s by a dc power supply (10 V at 0.8 A) in order to provide some free electrons which facilitate initiating the discharge. When a voltage of about 400 V is applied to the lamp, an arc forms between cathode and anode in the general form of an L. Most of the UV light is generated at the constricting aperture (1-mm diameter in our case) located in front of the anode. The main dc power supply is a 500 V,

300-mA constant current supply, with 0.1% current regulation. A ballast resistor (1 kΩ, 100 W) is used in the anode circuit because most power supplies cannot react fast enough to maintain a stable arc with only the lamp in the circuit. After the arc is started, the voltage across the arc drops to about 100 V. At this point the heater current is switched off, and the lamp output stabilizes in 20 minutes or less. If the lamp is switched off, it should be allowed to cool back to room temperature before restarting.

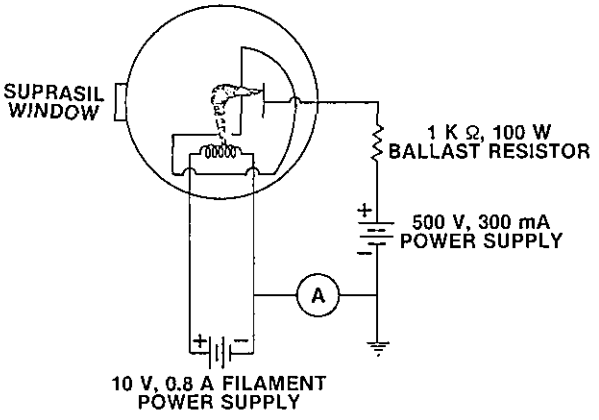

Figure 12. Schematic illustrating the operation of a deuterium lamp. The radiation is measured through the Suprasil window sealed to the quartz lamp envelope.

3. Calibration Methods

3.1 Radiance Calibrations

3.1.1 Introduction Spectral radiance, L_λ, is defined in the Introduction as the radiant power emitted by a source per area per solid angle per wavelength interval: $L_\lambda = [\mathrm{W\,cm^{-2}\,sr^{-1}\,nm^{-1}}]$. A calibration of radiance is performed by directly comparing the source to be calibrated with a standard radiance source. An optical system including lenses and/or mirrors is used to limit the geometrical quantities which are area and solid angle and to direct the radiation to a detector. A monochromator selects the wavelength band desired. First, one source is placed in position and signals are measured at the various wavelengths. This source is then replaced by the second source and the measurements are repeated. The radiance of the source to be calibrated is then obtained from the ratio of the signals times the radiance of the standard source. In general the signal obtained from a source is

$$S(\mathrm{A}) = \epsilon_\lambda\left(\frac{\mathrm{A}}{\mathrm{W}}\right)\cdot L_\lambda\left(\frac{\mathrm{W}}{\mathrm{cm^2\,sr\,nm}}\right)\cdot A\,(\mathrm{cm^2})\cdot\Omega(\mathrm{sr})\cdot\Delta\lambda(\mathrm{nm}), \tag{1}$$

where A is the area, Ω the solid angle, $\Delta\lambda$ the wavelength bandpass, L_λ the spectral radiance, and ϵ_λ the efficiency of the detection system. If subscript R refers to the standard source and subscript x refers to the one to be calibrated, then

$$\frac{S_x}{S_R} = \frac{\epsilon L_{\lambda,x}\cdot A_x\cdot\Omega_x\cdot\Delta\lambda_x}{\epsilon L_{\lambda,R}\cdot A_R\cdot\Omega_R\cdot\Delta\lambda_R} \tag{2}$$

If A, Ω, and $\Delta\lambda$ are identical for each source, then

$$L_{\lambda,x} = \left(\frac{S_x}{S_R}\right)\cdot L_{\lambda,R}\ . \tag{3}$$

3.1.2 Argon Arc The hydrogen arc primary standard is generally used to calibrate an argon arc. After measuring its signals, the hydrogen arc is removed and replaced with the arc to be calibrated. A telescope is used to align the argon arc, and once it is operating, a fine adjustment in position is accomplished by translating the arc both horizontally and vertically to maximize the signal. As with the hydrogen arc, there is a volume between the arc source and the vacuum window. This volume is purged with argon at a flow rate of 5 L/min. The purging must continue for at least 10 min before measurements are begun in order to sufficiently displace the air from this region. This flow rate is continued during the entire calibration. By monitoring the signal at 170 nm where air absorption is strong, the rise in signal during purging may be observed, and the time at which essentially all air is displaced can be determined. There are two cases to consider: 1) if the arc to be calibrated contains a window, the purge region is isolated from the arc, and any purge rate which is sufficient to maintain the region free of air may be used; and 2) if the arc to be calibrated is one without a window, the flow in the "purge" region is not independent of the arc, and the same flow arrangement must be used whenever the arc is used as a secondary standard. This is necessary because the flow rate in the purge region can have an effect on the arc operation and hence on the radiance of the arc. Once the argon arc is operating and the purge region is clear of all air, signals are measured for $124 < \lambda < 360$ nm, the range of the hydrogen arc. In addition to the wavelengths covered by the hydrogen arc, signals are also measured at shorter wavelengths extending

to 115 nm. In this region, however, there are numerous lines in the spectrum from minute air impurities. These lines are typically resonance lines and are extremely strong even at very low concentrations. The wavelengths at which the continuum is measured are selected to avoid interference from these relatively strong lines. Also, in order to avoid interference from the lines, the wavelength bandpass must be no greater than 0.2 nm (700 μm slits on the 3 m monochromator). The continuum from this short wavelength region is calibrated using a second primary standard, the blackbody line arc.

3.1.3 Blackbody Line Arc Another primary standard source, the blackbody line arc, is used to extend the calibration to wavelengths below 124 nm. This is also a wall-stabilized arc, operated with argon but including small admixtures of H, O, C, N, and Kr. These admixture elements furnish spectral lines which can be made to be *optically thick*, i.e., they reach a maximum radiance value at the wavelength of the line.

3.1.4 Tungsten Lamp Standard In the calibration of radiance one additional standard source, the tungsten strip lamp [10], is applied. The tungsten lamp is used for two reasons: 1) to increase the accuracy of the calibration, and 2) to extend the calibration to longer wavelengths. The wavelength ranges of the hydrogen arc and tungsten lamp overlap in the near UV region, and although the uncertainty in the radiance of the hydrogen arc is ±5%, tungsten lamps are calibrated for radiance with an uncertainty of ±2.3% in the near UV. Therefore, the calibration of a source extending to the near UV may be increased in accuracy by comparing it directly to the tungsten strip lamp. If this is done, a calibration using the hydrogen and blackbody line arcs is considered to furnish only the relative spectral distribution of the radiance of the unknown source. A calibration with the tungsten lamp at the long wavelength end of the range of the hydrogen arc then serves to set the absolute scale of the radiance.

3.1.5 Calibration of Argon Arcs Relative to an NBS Argon Arc For most calibrations the hydrogen arc and blackbody line arc are not employed, but rather calibrations are performed using a mini-arc (the NBS argon arc) as a transfer standard. The transfer standard is employed since calibrations with the hydrogen and blackbody arcs are much more difficult and time consuming than calibrations performed relative to an argon arc. Moreover, the comparison of two similar sources (two argon arcs) can be accomplished in reasonable time with less error than is involved in a calibration involving the hydrogen and blackbody line arcs. Therefore only a slight decrease in accuracy results from employing the transfer standard. The calibration of one argon arc relative to another proceeds similarly to the calibration of an argon arc relative to the hydrogen arc. The NBS argon arc is operated without a window using a purge rate of 5 L/min. The arc to be calibrated usually contains a window, and thus the calibration of the arc must include a separate measurement of its transmission.

3.1.6 Argon Mini-Arc Spectral Radiance Standard An argon mini-arc has been designed, tested, and operated as a transfer source of spectral radiance for the wavelength range from 114 to 330 nm. Calibration has been performed using two primary standard sources: the hydrogen arc from 130 to 330 nm and the blackbody line radiator from 114 to 130 nm. The mini-arc has the following principal features: 1) a steady-state reproducible source with dc power requirements of less than 1.5 kW; 2) an intense continuum which is line-free between 194 and 330 nm and which has only a few narrow and widely spaced impurity lines between 114 and 194 nm; 3) a uniform output over a solid angle as large as f/9; 4) negligible aging effects over at least a 24 hour period; and 5) uncertainties (2σ) in the absolute spectral radiance of 5.3% above 140 nm and 10.1% between 114 and 140 nm. The radiant power emitted by the mini-arc is influenced primarily by the arc diameter, the arc current, and the transmission of the UV window material.

3.2 Irradiance Calibrations

3.2.1 Establishment of Irradiance Scale: General Method Spectral irradiance is the radiant power incident upon a target area per area per wavelength band: $E = [\mathrm{W\ cm^{-2}\ nm^{-1}}]$. A source of radiation may serve as a standard source of irradiance by operating it at a given distance from the target area. If one had a radiance source with uniform radiance over its emitting area, the irradiance at a given distance from this source could be easily computed. In general however, radiance sources are non-homogeneous, and the radiance is known only for a small portion of the source, i.e., an area element which can be approximated to be homogeneous. Thus, the irradiance at some distance from the source can be determined only if radiation from outside the calibrated area is prevented from reaching the measurement system. This can be done by the use of optical imaging and/or collimating apertures. For applications in the VUV, the method

using collimating apertures [16] has proved to be more practical and is the basis for the measurements described here.

The collimating aperture method is as follows. A radiation source that is homogeneous over a certain emitting area and whose spectral radiance has been previously determined is situated a given distance from a monochromator. A pair of apertures, one at the entrance slit of the monochromator (the field aperture) and the other as close to the source as possible (the source aperture), is chosen so that only the radiation from the homogeneous portion of the source is measured. The spectral irradiance at the field aperture is given by the product of the known spectral radiance of the source and a geometric factor dependent on the aperture dimensions and their locations relative to the source. This geometric factor contains the information on the effective area of the emitting source, the solid angle of the radiation beam incident upon the field aperture, and the irradiated area.

In principle, these quantities can be determined by measurement. However, a direct determination of the geometric factor is unnecessary, as is shown by the following discussion. The response of a spectroradiometer as a function of wavelength to a suitably collimated radiance standard is essentially a measure of the system detection efficiency on a relative scale. If the same spectroradiometer is irradiated with an unknown source and the response is measured again, the spectral irradiance of the unknown source can be determined, also on a relative scale. Then, provided that the wavelength range of calibration extends to the visible or near-UV region in which standard sources of irradiance are available, the absolute spectral irradiance of the unknown source can be determined at one wavelength within the calibrated wavelength range. This absolute value can then be used to normalize the relative scale of irradiance to an absolute scale.

3.2.2 Argon Arc Calibrations Two types of sources are calibrated as irradiance standards, the argon mini-arc and the deuterium lamp. Calibration of an argon arc will be discussed first.

The light source used here as a standard of spectral radiance in the VUV and near UV is an argon mini-arc previously calibrated by the hydrogen arc. This source is used according to the method described above to calibrate a second mini-arc as an irradiance standard. The measurements in the VUV spectral range are performed using a SEYA monochromator. The above measurements determine the irradiance of the unknown source only on a relative scale. To obtain an absolute scale, the irradiance of the unknown source is compared in the near UV region to that of a calibrated tungsten-quartz-halogen irradiance standard [17]. This measurement is carried out on a double monochromator, with an integrating sphere used as its entrance aperture. For this measurement this setup has two advantages. First, the double monochromator greatly reduces scattered light which otherwise would be a serious problem for the quartz-halogen source. Second, the integrating sphere serves as a better method of rendering the signal insensitive to the direction of radiation from the source. This is important in comparing the small sized arc source with the much larger quartz-halogen source area.

The determinations of spectral irradiance are based on the assumptions that the system efficiencies of the measuring spectroradiometer are independent of the angle at which the radiation enters and that diffraction effects are not significant. Since the monochromator grating used must be assumed to have a nonuniform reflection efficiency, a diffuser located directly behind the field aperture is used to ensure that the first assumption is met. A magnesium fluoride window, ground on one side, was used as the diffusing element. Although it cannot be expected to be as good a diffuser as an integrating sphere, it was shown to be suitable, at least over a relatively small range of angles. For the argon mini-arc the uncertainty in the spectral irradiance that is due to the nonideal properties of the diffusing window can be as high as 6%.

The possible effects of diffraction must also be considered. For an extended homogeneous radiation source whose dimensions are large compared with the source aperture, it can be shown that Frauenhofer diffraction effects introduce no wavelength dependence and that the geometric factors are wavelength independent. This can be understood qualitatively by realizing that some percentage of the radiation from each radiating point does not pass through the field aperture because of diffraction. However, a complementary point can always be found in the domain of the extended homogeneous source that exactly makes up for such a loss. By substituting a different-sized aperture we have shown that the inhomogeneity of the mini-arc is insufficient to cause any measurable effects due to diffraction.

The vacuum spectroradiometer consists of a solar blind photomultiplier and a spectrometer with a 2-mm diameter field aperture. This aperture is

mounted on a MgF_2 diffusing window located 50 mm in front of the entrance slit. The diffuser was located some distance in front of the entrance slit so as not to overfill the grating and thereby increase the scattered light, which was less than 2% of the weakest signal. The mini-arc was located 50 cm from the field stop, and a 0.3 mm-diameter aperture placed 5 cm from the mini-arc center was used to restrict the size of the radiating area to about 0.5 mm in diameter. The 2σ uncertainty in the absolute spectral radiance of the mini-arc has been given above to be 5.3% between 140 and 330 nm.

The total uncertainty in the irradiance calibration of an argon mini-arc, including uncertainties in the primary source calibration and the transfer procedure, is estimated to be $\lesssim$10%. Although the arc emits radiation at shorter wavelengths than that shown in figure 13, the short wavelength limit is taken to be 140 nm because of the low signal obtained from the stopped-down mini-arc radiance standard at shorter wavelengths. The bandpass for the radiance-to-irradiance transfer here was set at 1 nm. Not shown in figure 13 are several lines in the argon arc spectrum that are due to residual gas impurities [14]. The irradiance of the mini-arc was put on an absolute scale by determining its absolute spectral irradiance at 280 nm, using a tungsten-quartz-halogen lamp as an irradiance standard. A separate spectroradiometer utilizing a $BaSO_4$-coated integrating sphere, a predispersing monochromator, and an analyzing spectrometer was used for this measurement. One measurement of this type is sufficient to determine the absolute irradiance at all wavelengths [16].

3.2.3 Deuterium Lamp Calibration Deuterium lamps are calibrated as spectral irradiance standards in the near UV range $200 \leqslant \lambda \leqslant 350$ nm by another calibration group in the Radiometric Physics Division of NBS. The lamps calibrated are of the side-on type. Prior to calibration they are potted in a base identical to that of the tungsten-quartz-halogen lamps. Our calibrations of such lamps usually consist of extending the spectral range in the vacuum UV down to 165 nm. The measurements are performed on the SEYA monochromator setup, using the same method as was described in the previous section for calibrating an argon arc as an irradiance source.

Briefly, a set of commercially available deuterium lamps was calibrated for spectral irradiance in the 167–350 nm spectral range. At 250 nm and above the spectral irradiance values were obtained using a tungsten-quartz-halogen lamp whose calibration is based on an NBS blackbody. Below 250 nm the relative spectral distribution of the deuterium lamps was determined through the use of an argon mini-arc spectral radiance transfer standard whose calibration is based upon the NBS wall-stabilized hydrogen arc. The absolute values assigned to the deuterium lamps were then obtained by normalizing to the spectral irradiance values at 250 nm and above. Confidence in this procedure was established by comparing the absolute spectral irradiance of the deuterium lamps as determined independently by the argon mini-arc radiance standard and the tungsten-quartz-halogen irradiance standard in the 250–330 nm range. The agreement was within 3%. The large UV flux and high stability of the mini-arc are the properties which make possible the calibration below 250 nm.

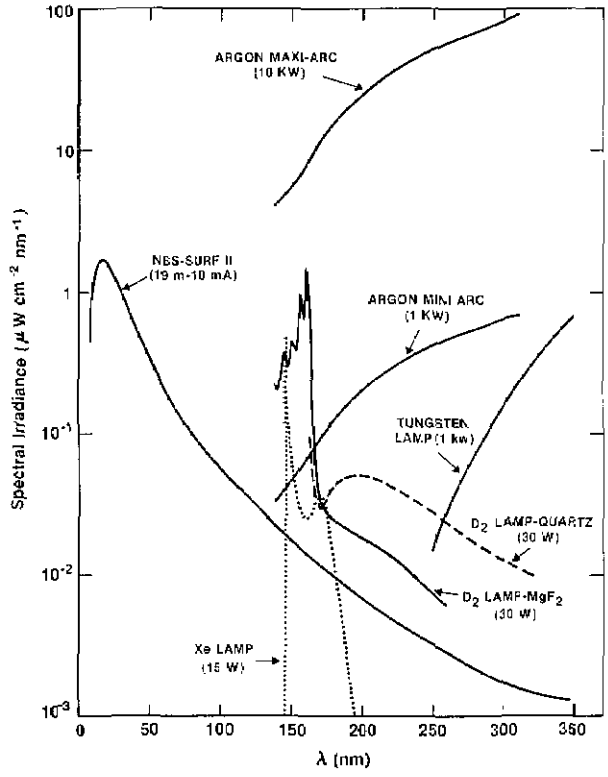

Figure 13. Absolute spectral irradiance measured as a function of wavelength at a distance of 50 cm from the field aperture for five different continuum sources with the indicated power requirements. The spectrum of the D_2 lamp with MgF_2 window below 170 nm, measured for a 1 nm bandpass, is a pseudo-continuum made up of blended lines. Shown for comparison purposes are spectra of the 250 MeV National Bureau of Standards synchrotron radiation facility, for a beam current of 10 mA and a field aperture distance of 19 m, and the tungsten-quartz-halogen lamp, for the standard 50-cm distance.

Since the deuterium lamps are aligned and potted in bipost bases identical to those used in mounting tungsten-quartz-halogen lamps, the two standards are interchangeable in a given optical system. Because the shapes of the spectral distributions of these lamps are so different, the presence of systematic errors in a measurement system may be detected by intercomparing the two sources. The spectral irradiance of the 30 W deuterium lamp is equal to that of the 1000 W quartz-halogen lamp at about 260 nm, 100 times stronger at 200 nm, and 100 times weaker at 350 nm.

The uncertainties in the absolute values of the deuterium lamp spectral irradiance are: 200 nm and above, 6%; 171 to 195 nm, 7%; and 170 nm and below, 10%. A major contribution to each uncertainty is the variability associated with the striking of the deuterium lamps. As a result all calibrated deuterium lamps supplied to customers by NBS are preselected for variabilities of 4% or less. For higher accuracy and confidence, one may take advantage of the result that the relative spectral distribution of the deuterium lamps is reproducible to within about 1%. Thus, the uncertainty may be reduced by renormalizing the absolute scale with a quartz-halogen lamp after each ignition to eliminate any variability in the strike. This procedure makes possible a reduction in the uncertainties of about 3%.

Additional work has shown that under certain conditions the deuterium lamp with an MgF_2 window may be used as a radiometric standard down to 115 nm [18]. This effort was directed at determining the circumstances under which portions of the many-line molecular spectrum below 167 nm can be used as a continuum.

Acknowledgments

This paper is a condensation of *NBS Measurement Services: Radiometric Standards in the Vacuum Ultraviolet*, NBS Special Publication 250–3. The NBS publication is an extensive treatment by the present authors of the radiometric calibration program carried out by the vacuum ultraviolet radiometry group in the Atomic and Plasma Radiation Division of the National Bureau of Standards. NBS Special Publication 250–3 is available from the Superintendent of Documents, U.S. Government Printing Office, Washington, DC 20402–9325.

The authors are grateful for the suggestions made by W. L. Wiese and J. R. Roberts. Also, the authors wish to acknowledge the continuing support of the VUV radiometry program at NBS by the NASA Solar and Heliospheric Branch. Most of the work described here was carried out under partial funding by this agency.

References

[1] Ott, W. R., Behringer, K., and Gieres, G., Vacuum ultraviolet radiometry with hydrogen arcs. 2: The high power arc as an absolute standard of spectral radiance from 124 nm to 360 nm, Appl. Opt. **14**, 2121–2128 (1975).

[2] Roberts, J. R., and Voigt, P. A., The calculated continuous emission of a LTE hydrogen plasma, J. Res. Natl. Bur. Stand. (U.S.) **75A**, 291–333 (1971).

[3] Ott, W. R., Fieffe-Prevost, P., and Wiese, W. L., VUV radiometry with hydrogen arcs. 1: Principle of the method and comparisons with blackbody calibrations from 1650 Å to 3600 Å, Appl. Opt. **12**, 1618–1629 (1973).

[4] Ott, W. R., and Wiese, W. L., Far ultraviolet spectral radiance calibrations at NBS, Opt. Eng. **12**, 86–94 (1973).

[5] Wiese, W. L., Electric arcs, in *Methods of Experimental Physics*, Bederson, B., and Fite, W. L., Eds. (Academic, New York, 1968), Vol. 7B, 307–353.

[6] Larenz, R. W., Über ein Verfahren zur Messung sehr hoher Temperaturen in nahezu durchlässigen Bogensäulen, Z. Phys. **129**, 327–342 (1951).

[7] Behringer, K., Präzisionmessungen am Spektrum des Wasserstoffplasmas, Z. Phys. **246**, 333–347 (1971).

[8] Kepple, P. C., Improved stark profile calculations for the first four members of the hydrogen Lyman and Balmer series, Dept. of Physics and Astronomy, Univ. of Maryland, Report No. 831 (1968).

[9] Maecker, H., and Steinberger, S., Weiterentwicklung der Kaskaden-bogenkammer für hohe Leistungen, Z. Angew. Phys. **23**, 456–458 (1967).

[10] Walker, J. H., Saunders, R. D., and Hattenburg, A. T., *NBS Measurement Services: Spectral Radiance Calibrations*, Natl. Bur. Stand. (U.S.) Spec. Publ. **250–1** (January 1987).

[11] Boldt, G., Das thermische Plasma als Intensitätsnormalstrahler im Wellenlängenbereich von 1100 bis 3100 Å, Space Sci. Rev. **11**, 728–772 (1970).

[12] Morris, J. C., and Garrison, R. L., A radiation standard for the vacuum ultraviolet, J. Quant. Spectrosc. Radiat. Transfer **9**, 1407–1418 (1969).

[13] Stuck, D., and Wende, B., Photometric comparison between two calculable vacuum ultraviolet standard radiation sources: synchrotron radiation and plasma-blackbody radiation, J. Opt. Soc. Amer. **62**, 96–100 (1972).

[14] Bridges, J. M., and Ott, W. R., Vacuum ultraviolet radiometry. 3: The argon mini-arc as a new secondary standard of spectral radiance, Appl. Opt. **16**, 367–376 (1977).

[15] Saunders, R. D., Ott, W. R., and Bridges, J. M., Spectral irradiance standard for the ultraviolet: the deuterium lamp, Appl. Opt. **17**, 593–600 (1978).

[16] Ott, W. R., Bridges, J. M., and Klose, J. Z., Vacuum-ultraviolet spectral-irradiance calibrations: method and applications, Opt. Lett. **5**, 225–227 (1980).

[17] Walker, J. H., Saunders, R. D., Jackson, J. K., and McSparron, D. A., *NBS Measurement Services: Spectral Irradiance Calibrations*, Natl. Bur. Stand. (U.S.) Spec. Publ. **250–20** (1987).

[18] Klose, J. Z., Bridges, J. M., and Ott, W. R., The use of deuterium lamps as radiometric standards between 115 nm and 350 nm, Extended Abstracts of the VI International Conference on Vacuum Ultraviolet Radiation Physics. Charlottesville, VA, III-52 (June 1980).

Appendix. NBS Calibration Services in the Near and Vacuum Ultraviolet

1. Spectral Irradiance Standard, Argon Mini-Arc (140–330 nm), SP 250 No. 40010S (7.6B)

An argon mini-arc supplied by the customer is calibrated for spectral irradiance at 10 nm intervals in the wavelength region 140–330 nm. Absolute values are obtained by comparing the radiative output with laboratory standards of both spectral irradiance and spectral radiance. The spectral irradiance measurement is made at a distance of 50 cm from the field stop. Uncertainties (2σ) are estimated to be less than $\pm 10\%$ in the wavelength region 140–200 nm and within $\pm 6\%$ in the wavelength region 200–330 nm. A measurement of the spectral transmission of the arc window is included in order that the calibration be independent of possible window deterioration or damage.

2. Spectral Radiance Standard, Argon Mini-Arc (115–330 nm), SP 250 No. 40020S (7.6C)

The spectral radiance of argon mini-arc radiation sources is determined to within a 2σ uncertainty of less than 6% over the wavelength range 140–330 nm and 11% over the wavelength range 115–140 nm. The calibrated area of the 4 mm diameter radiation source is the central 0.3 mm diameter region. Typical values of the spectral radiance are: at 250 nm, $L_\lambda = 30$ mW cm^{-2} nm^{-1} sr^{-1}; and at 150 nm, $L_\lambda = 3$ mW cm^{-2} nm^{-1} sr^{-1}. The transmission of the demountable MgF_2 lamp window and that of an additional MgF_2 window are determined individually so that the user may check periodically for possible long term variations.

3. Spectral Irradiance Standard, Deuterium Arc Lamp (165–200 nm), SP 250 No. 40030S (7.6D)

The lamp is calibrated at 10 wavelengths from 165 to 200 nm at a distance of 50 cm. Its spectral irradiances are about 0.05 μW cm^{-2} nm^{-1} at 165 nm, 0.03 μW cm^{-2} nm^{-1} at 170 nm, and 0.05 μW cm^{-2} nm^{-1} at 200 nm. The approximate 2σ uncertainty relative to SI units is estimated to be less than 10%. The lamp is normally supplied by NBS and requires 300 mA at about 100 V.

4. Special Tests of Radiometric Devices in the Near and Vacuum Ultraviolet, SP 250 No. 40040S (7.6A)

Tests of customer supplied radiometric devices not included above are performed at the direction of the customer.

Volume 93, Number 1, January-February 1988
Journal of Research of the National Bureau of Standards

Grid Plate Calibration at the National Bureau of Standards

Volume 93 Number 1 January–February 1988

Theodore D. Doiron

National Bureau of Standards
Gaithersburg, MD 20899

Grid plates are calibrated by a completely automated high precision measuring machine which uses a computer vision system to detect and locate the grid marks. The system routinely calibrates plates of up to 600×600 millimeters with accuracies of 0.5 micrometers. Descriptions of the system components, level of performance and tests of the absolute accuracy of the calibrations are presented.

Key words: calibration; geometry correction; grid plate; measuring machine; metrology; two dimensional metrology.

Accepted: October 2, 1987

1. Introduction

With the increasing use of video based dimensional measuring machines, there is a corresponding growth in the need for two-dimensional artifacts to use as calibration standards. Since the major uses for these systems range from measuring semiconductor geometry over a few square millimeters to photogrammetry and PC board inspections over a square meter, a system for calibrating such standards must have both high accuracy and a large dimensional range. The grid plates discussed in this paper are generally glass plates with some type of symmetric grid mark plated on the glass surface. The simplest type is a glass plate with a square grid of 20 μm wide chrome lines spaced every one or two centimeters. However, the variety of materials and grid marks is large, ranging to metal plates with randomly drilled holes.

This note is designed to describe the theory, operation, and performance of the NBS automated grid plate calibration system. This system uses a computer controlled coordinate measuring machine and a computer based video system to detect and record the positions of the grid marks on grid plates up to 600 mm square. The normal calibration procedure is to measure the position of each grid mark on a plate in a pattern which repeatedly measures a few of the points several times distributed throughout the run to gather process control data on the calibration repeatability and drift. The run is then repeated. The plate is turned 90 degrees and measured twice again. This process of collecting redundant data provides enough information to give the positions on the grid marks, statistical information for realistic error estimates, and process control data about the measurement system.

The description of the system is organized into six sections: the coordinate measuring machine, the video imaging system, the measurement procedure, the data analysis, the system accuracy, and the outlook for upgrading the calibration performance.

2. Coordinate Measuring Machine

2.1 Hardware

The machine used for grid plate calibrations is a Moore Special Tool Company five-axis coordinate measuring machine[1]. It has a fixed bridge type geometry with a measuring volume of 1200×600×250 mm. The machine has been extensively studied and is described in detail in [1] and [2].

The machine, shown in figure 1, has very accurate lead screws and guideways. To increase the accuracy even further, each axis was retrofitted with a laser interferometer which allows resolution of displacements of less than 0.02 μm. The laser interferometer receivers and corner cubes were placed on metrology frames attached to the table, Y slide, and on top of the Z spindle. The X motion is provided by a table which travels on twin V roller bearing ways. The Y axis moves on twin V roller bearings on a fixed bridge. The total travel is 1200 mm in the X direction and 600 mm in the Y direction.

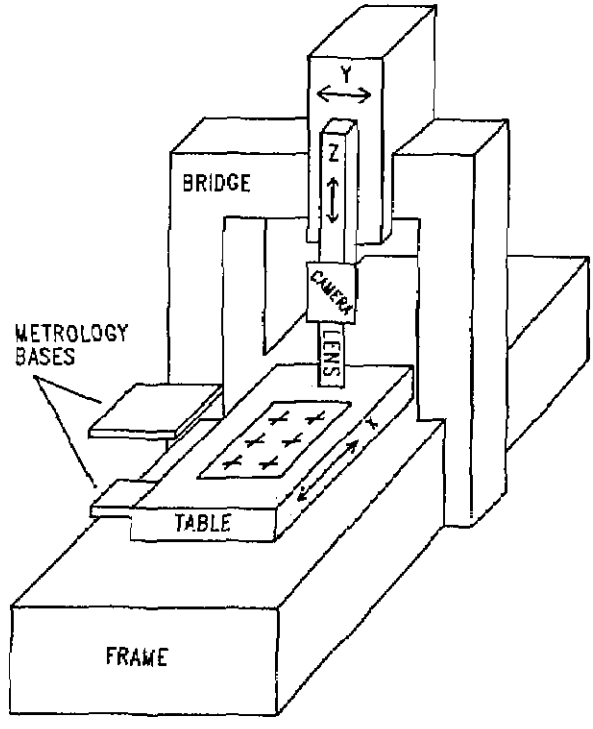

Figure 1. Diagram of coordinate measuring machine. The metrology bases support the laser interferometer systems. The error map relates the measured position of the bottom of the Z axis to the true position in an ideal reference frame.

[1] Certain commercial equipment, instruments, or materials are identified in this paper in order to adequately specify the experimental procedure. Such identification does not imply the recommendation or endorsement by the National Bureau of Standards, nor does it imply that the materials or equipment are necessarily the best available for the purpose.

The geometric errors of the machine are quite small for a machine of this size. In order to obtain the maximum accuracy possible from the machine, a systematic study of the errors inherent in the machine was made.

While no attempt is made to correct for the small geometric errors in the machine motion during a measurement, software algorithms have been developed to correct the raw data for all of the known rigid body errors in the machine motion. A model of the machine was developed which included all of the rigid body systematic geometric errors, including the pitch, yaw, roll, and straightness of each axis. From very precise and repeated measurements of these errors an error map was developed which, when used with the model of the machine, could correct any measurement to an accuracy near the level of the repeatability of the machine.

The error map was measured at each of 1950 equally spaced points in the measurement volume and the standard deviations of the measured errors were found to be quite small; about 0.01 second of arc for the angular error and 0.02 μm for the straightness errors. Examples of the error diagrams obtained are shown in figure 2.

Many of the maps are smooth, as in figure 2(a). Even though the error map is measured at 2-inch intervals, a linear interpolation of the map provides an adequate measure of the error for points between measured points. Some of the errors are more complex, as in figure 2(b). It is obvious that there is structure to the errors between the calibration points which would result in small local systematic errors of up to 0.05 μm. Since these interpolation errors in one cell of the calibration grid are uncorrelated with those of other cells, multiple measurements placing the grid at different places on the table will reduce the error by averaging.

The only significant systematic error which could not be adequately modeled is that due to the table bending. The machine moves on twin V cross section roller bearings. Because of small irregularities in the parallelism of the ways, the table is pinched slightly as it moves from one end of travel to the other. The table response is to bend upward in the middle, when unloaded, by as much as 2.5 μm. Since this is not a rigid body motion it is difficult to include the associated errors in the

model. However, because of the large number of correction parameters used in the model, some compensation is made in the fitting process and the residual error is small. The problem is serious only because the table bending depends on the weight and position of the piece being measured. For ball plates, which can be 50 to 200 kg, this is a serious problem as the error map might shift; for grid plates which weigh up to 1 kg the problem is minimal.

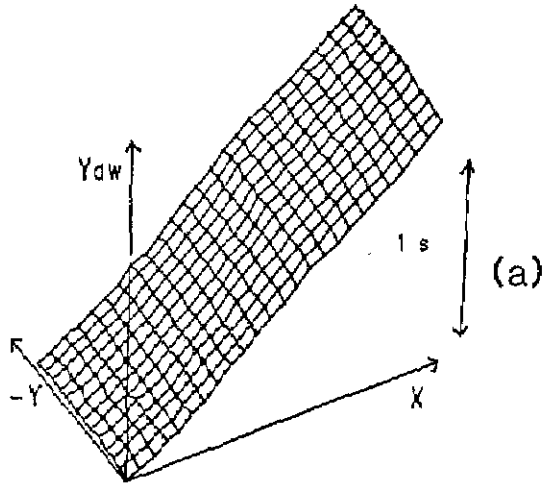

Yaw of X table motion

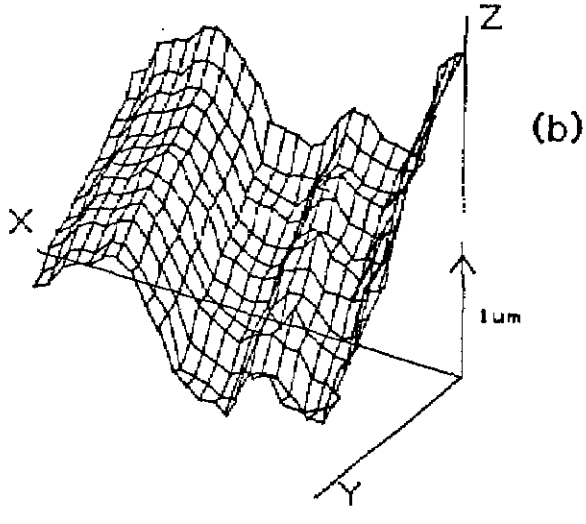

Z straightness of X table motion

Figure 2. Typical error maps for coordinate measuring machine. The repeatability of the data is more than an order of magnitude smaller than the measured errors.

Each time a calibration is made with the machine, the machine model and error map are used. By taking redundant data, as explained in section 4, any change in the error map will be apparent from the data analysis. Over the years since the original calibration was made, no significant change in the error map has been found.

2.2 Environmental Control

The machine environment, that is, temperature, air pressure and humidity, affect measurement accuracy. While the highest quality grid plates are made from quartz, which has a very small thermal expansion coefficient, the machine is made of steel, and the effects of environmental changes on the measuring machine geometry are important. Besides maintaining the room temperature as nearly constant as possible, as many heat sources as possible have been controlled. For example:

a. Each step motor has a temperature control system which circulates chilled water in tubing attached to the motor housing if the temperature rises above a preset temperature;

b. The room has indirect lighting to prevent shadows;

c. The measurement is completely automated so that no human heat source need be present near the machine after the run has begun;

d. Ten thermocouples, placed at strategic locations on the machine, measure the thermal profile of the machine as the calibrations are made to check on the actual thermal stability of the machine frame;

e. Generally, the machine is run through a warm-up cycle for 2 to 6 hours to assure that thermal equilibrium is reached before the measurement run is begun.

The air temperature, pressure, and humidity are also important to the length scales of the machine. Since the interferometers measure in terms of the laser wavelength in air, the index of refraction of the air is important. Most laser measurement systems have available sensors which automatically make corrections, but in order to maintain the

highest level of measurement assurance we measure the temperature, pressure and humidity independently and calculate the index of refraction from the formula of Jones [3].

The room stability is quite good over long periods of time, within 0.2 °C, but since the room is not separately thermostated, occasional temperature excursions occur. An example is shown in figure 3.

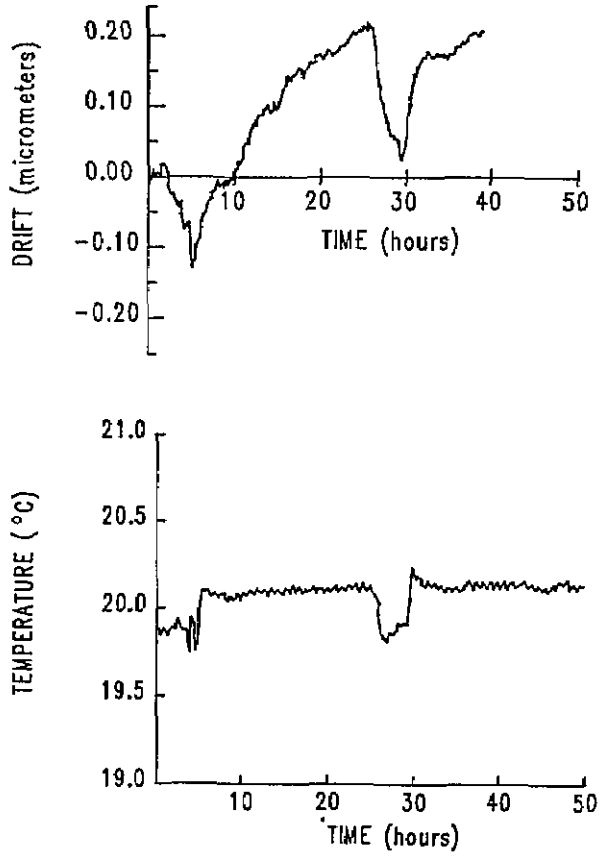

Figure 3. Room temperature and Y coordinate of the bottom of the Z axis as functions of time, showing machine response to change in room temperature.

The top graph shows the Y direction motion of the bottom of the Z axis in response to the air temperature change shown in the bottom graph. The thermal time constant of the machine is over 2 hours, and four to six time constants are needed before the temperature stability is adequate for a calibration.

The temperatures of the air, grid plate, and machine are recorded at least every hour during the measurement to detect thermal problems. Because of the difficulty of developing a thermal model of the machine which would allow correction of the data for temperature changes, the machine thermal profile data is used only as a "go/no go" test for the calibration. If the machine thermal profile has been insufficiently stable during a particular measurement, that measurement is repeated. Even under the best conditions there is some small drift in the system over the 1 to 3 hours of a typical measurement. To compensate for some of this drift the measurement algorithm has at least one reference point which is repeated periodically during the run to provide a practical measure of the machine drift. Details of this technique are provided in section 4.

3. Video Imaging System

A high-resolution television camera (vidicon) equipped with a commercial microscope system mounted on the Z axis of the machine is used to observe the marks (usually crosses) on the grid plate. A block diagram of the system is shown in figure 4.

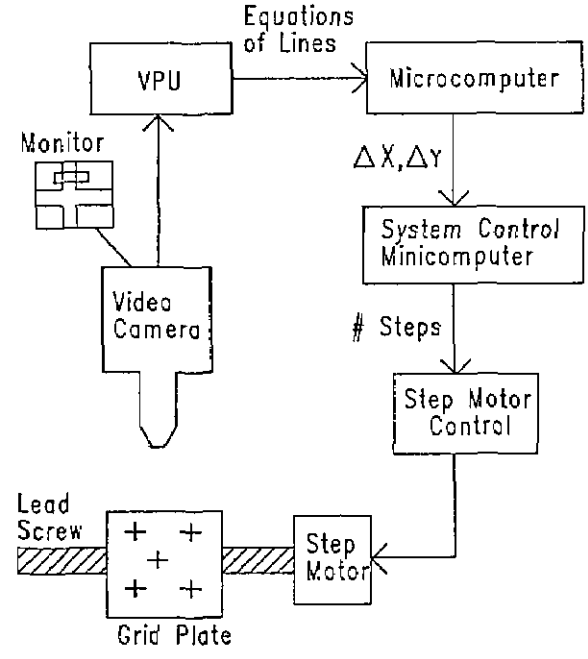

Figure 4. Block diagram of video system feedback loop. The VPU finds the slope and intercept of each edge of the grid mark arms, using windows as shown on the monitor. The microcomputer functions as a smart interface and transfers position offset data to the system controller. The system controller moves the camera to the center of the grid mark.

The commercial video processor currently used is a simple edge detector. The output from a high resolution vidicon is fed into a processor and digitized into a 400×500 picture element (pixel) grid. The signal is compared with a user chosen intensity threshold, and on each line the positions of the first

and last threshold crossings (dark to light or light to dark) are recorded in the system memory.

The raw data, or the results of any of a number of functions of the raw data performed in the processors firmware, can be output to a remote computer. Among the functions used for our measurements, the most important are:

Windowing—Any rectangular portion of the video image field can be used for analysis, ignoring the rest of the picture. By using windows, irrelevant lines and noisy areas of the picture can be avoided, allowing unambiguous analysis of the video data.

Centroid—The centroid of black or white pixels can be calculated. For symmetric grid marks such as crosses, Xs, and circles the centroid is used as a fast measure of the correction needed to move the mark close to the center of the screen.

Linear fit to an edge—A line can be fit to either the leading edge (first threshold crossing) data or the trailing edge data in any window. Thus, if the windows are chosen to include only one edge of a grid mark, the slope and intercept of the line can be obtained.

There are several ways to define the center of the grid mark. Among the possibilities are the centroid of the grid mark, the centroid of the edges of the grid mark, and various fits to features of the mark. For most marks, which are crosses, we have chosen to fit a straight line to a section of the two edges of each of the four arms of the cross. Generally, an edge fit which avoids the actual intersections of the lines provides the most accurate calibrations, particularly for lower quality grids which have various irregularities at the line intersections. As shown in figure 5, there are a number of defects which can cause problems; such as dirt, which is removable, and chips and stray marks, which are not.

We use the centroid of the intersections of the eight lines as the center position. The difference between the calculated center of the grid mark and the center of the video display is used by the computer system to move the X and Y carriages until the camera is directly over the center of the mark as indicated by a null reading.

This procedure eliminates the need for precise calibration of the vision system. Since all of the grid marks are nearly identical, and the marks are brought to the same position and orientation in the video field, many systematic errors in the camera system are irrelevant. For example, since the image is symmetric, lowering or raising the threshold changes the width of the lines, but the apparent center is not displaced. Also, any small geometric distortion in the system optics does not affect the relative positions of the grid marks.

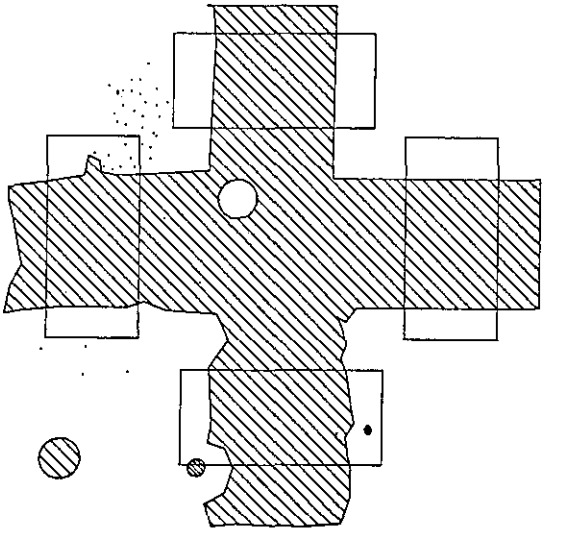

Figure 5. Composite grid mark showing placement of video windows and typical grid mark irregularities. The small dots represent video noise and dust.

Repeatability of the system is quite good. Multiple measurements of the center of a single grid mark gives a standard deviation of the calculated center coordinates of less than 1 pixel as shown in figure 6. For high quality grids with linewidths of 10 to 20 μm, precision is commonly 0.2 to 0.4 pixels, and is nearly independent of the magnification of the microscope up to about 0.2 μm per pixel. At higher magnification diffraction effects become important.

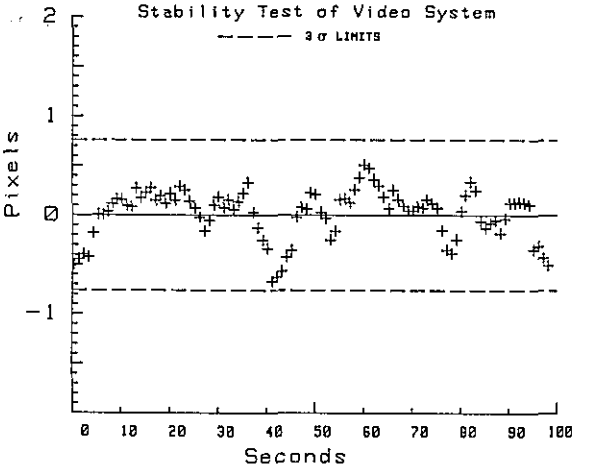

Figure 6. Stability and repeatability of the video system. The precision is relatively independent of the microscope magnification until diffraction from the edges becomes dominant.

One problem which has not yet resolved is that the algorithm for defining the center corresponds to that of a human operator only if the grid mark is smooth, sharp and free from defects. A human operator would ignore irregularities in the edge of the line. The current program uses these stray points as well as the edge points of the grid mark, a procedure which will produce calibrations with systematic differences from those of a human operator. Photoelectric microscopes have been used on many line centering systems [4,5] and are thought to provide a response close to that of a human observer. However, because of the large number of points used in the algorithm (over 1000) and the window placements, the lines must be quite defective to produce significant errors.

A number of other methods for defining the grid mark center have been tried, including algorithms using the centroid of the line rather than edge fits. Methods which use points on the interior of the lines, such as the centroid function, are less vulnerable to noise in the video signal but have lower precision than edge methods. Methods using multiple windows and various tests for edge irregularities can be used, but the amount of time needed for each intersection becomes much larger. Because of the increased time needed for the measurement, the gain in accuracy in the center measurement is usually canceled by random error due the variability of the room temperature. Plates which do not have consistent and well formed marks are assigned higher values of uncertainty.

For the highest quality grid plates, magnification is limited by diffraction; the edges of the lines become indistinct. This limit is reached for magnifications of more than 0.15 μm per pixel. The effect of higher magnification is that the standard deviation of the measured coordinates becomes larger and cancels the gain in magnification. For most grid plates the optical magnification used is limited by practical considerations rather than limits due to diffraction or optical aberrations. The rules of thumb used to select the magnification depend on both the performance of the system and the characteristics of the grid plates calibrated in the past.

1. Geometric irregularities; e.g., widening or necking of the lines, chipped edges due to wear, or dirt are very frequent at the intersection of the two lines which make up the grid mark. Because of this a square area of two to three times the line diameter on a side centered on the grid mark center is avoided.
2. When the fit is done to the edges of the grid mark, there are two requirements for the fit. The first is that enough of the line is sampled to get a true picture of the line edge geometry. The second is that the fit must be accurate enough to be extrapolated to the center of the line to find the center.

Using these rules for 20 μm lines (the most common size), magnification of approximately 0.5 μm per pixel is used. For smaller lines more magnification, up to 0.15 μm per pixel is used. The largest line encountered has been 250 μm, and magnification of 2 μm per pixel was necessary. At this low magnification the precision of the centering algorithm was seriously affected.

4. Measurement Procedure

The measurement procedure and data analysis are designed to implement the principles of multiple redundancy and temporal modeling. There have been a number of schemes proposed [1,5–7]; the scheme currently implemented is that of Hocken and Borchardt [2]. An overview of the calibration is shown in figure 7.

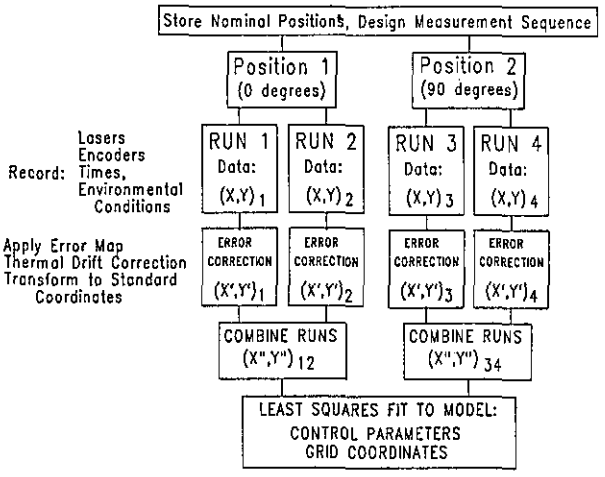

Figure 7. Overview of grid plate calibration system.

The first step is to make up a measurement pattern, i.e., the order in which the points are to be measured. The program GRIDPLT controls the machine and records the coordinates, environmental factors, and the time at which each measurement is made. The raw data is then corrected for the known geometric errors of the machine by SHOWER2D. Thermal drift corrections, if needed, are also made in this program. Finally, the two runs in each orientation are combined and the data fit to the calibration model by ALBE3. This program reports the coordinates of the grid marks,

the process control parameters, and an estimate of the calibration uncertainty. Each of these steps is explained in detail in the rest of this section.

The model of the measurement system must include both the coordinates of the grid marks as well as all of the known systematic errors. For example, a grid plate model for the simplest case, three grid marks, might contain as parameters the true coordinates of the points, an angular correction for a possible error in the X and Y axis squareness, and a scale error for differences in the X and Y length scales. This case is shown in figure 8.

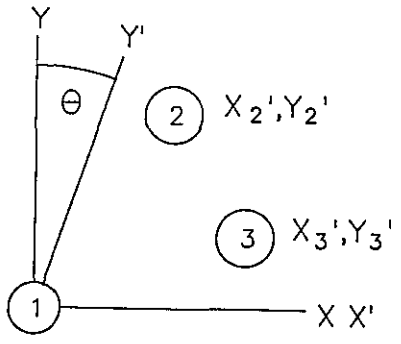

PARAMETERS (6)	DATA (8)
X2,Y2,X3,Y3,Θ,Δ	X2',Y2',X3',Y3' ROTATED X2",Y2",X3",Y3"

Figure 8. Simple model for three-point grid plate. In two runs, eight independent data points are taken. Since the model has six parameters, a best fit to the model can be made.

The true coordinates are in the ideal system X and Y. The machine coordinate system X', Y' is characterized by a possible difference in scale, Δ, and the deviation of the axes from orthogonality, Θ. Since the actual errors in the machine are small, a linear model is adequate.

The machine coordinates are set so that point 1 is the origin. If the coordinates of the points are measured in the machine coordinates, ($X2'$, $Y2'$) and ($X3'$, $Y3'$), and again with the plate rotated 90 degrees, ($X2''$, $Y2''$) and ($X3''$, $Y3''$), we have a total of eight data values. Since the model has only six parameters the model can be solved. Obviously for real grid plates with 12 to 130 points the number of redundant points is very large.

In actual practice, the plate is measured four times, twice in one orientation and twice after rotating the plate 90 degrees. The two repeat runs are averaged to increase the precision of the coordinates. Each individual run has a number of repeated points which allow any drift in the machine coordinate system to be measured. A sample calibration pattern is shown in figure 9.

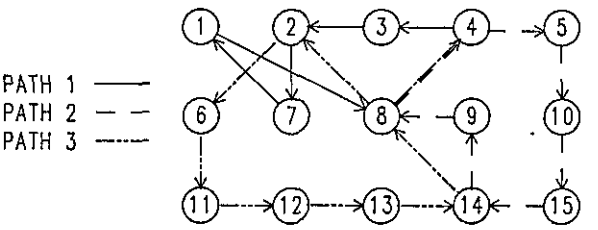

Figure 9. Typical calibration pattern. The complete design is path 1 followed by path 2 followed by path 3. Point 8 is the primary reference for measuring the drift in the machine geometry. The other repeat points are used to check the repeatability of the system.

Notice that point 8 is taken several times during each run. The drift in the coordinates of point 8 is a measure of the drift in the machine coordinate system. To monitor the drift, the point must be taken at a frequency large with respect to the inverse time constant of the machine thermal relaxation. For most grids, one point measurement takes 2 to 3 minutes, and the repeat point is taken every five to 10 points to give a frequency of three to four times an hour. The thermal relaxation time is about 2 hours as mentioned in section 1.

At each point the coordinates and the time of the measurement are recorded. The currently used algorithm takes the change in the coordinates of the repeat point, assumes the change is linear in time, and applies a scaled correction to all of the points taken between the two measurements of the repeat point. A typical drift pattern is shown in figure 10.

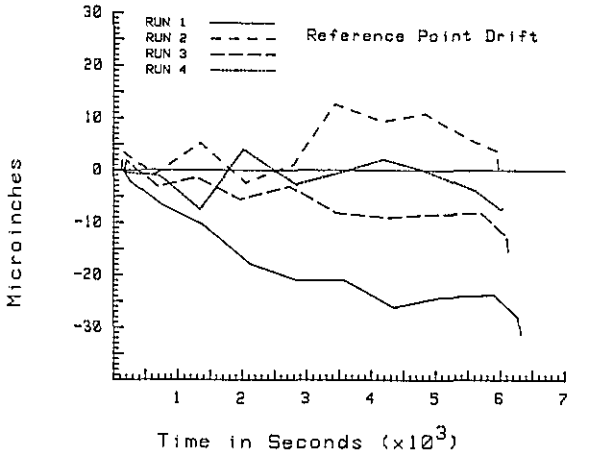

Figure 10. Time dependence of reference position during a typical calibration. Note that the longer the machine has been running the more stable the geometry becomes. Run 1 was preceded by a 2-hour warmup, and each run took about 1 hour.

Runs 2 and 4 are done directly after runs 1 and 3, respectively, and therefore have a longer effective warmup time. If the plate is turned directly after run 2, then runs 3 and 4 both have a long effective warmup. This usually leads to smaller drift corrections for runs 2 and 4, and sometimes 3 as shown in the figure 10.

Since the primary repeat point data is corrected for drift it has no apparent uncertainty in position. The standard deviations of the other repeat points from their average positions are pooled to get a quick measure of the repeatability of the run. If the repeat points are widely separated in time and space, this standard deviation is usually very close to the pooled standard deviation found when the two runs from one orientation are combined.

Using the technique of multiple redundancy in the data collection, (i.e., multiple readings of certain points in each run, plus multiple runs in multiple orientations), there is enough information to determine all of the model parameters. Since these parameters include both the coordinates of the grid marks and measures of the known systematic errors of the measurement system, each calibration provides measurement assurance data. With this constant monitoring of the major systematic errors, it is not necessary to make frequent measurements of our control grid plate to assess system performance.

The procedure also provides a measure of the unmodeled systematic errors since any errors which are not identical for both axes will increase the apparent random error of the calibration. In fact, the standard deviation of the combined four runs is generally about 0.03 μm larger than that of the individual runs, implying small residual unmodeled systematic errors.

5. Performance

There are two important aspects of performance which have been studied; the precision and accuracy reported by the data analysis, and the true accuracy with respect to the national length standard.

About 50 plates calibrated with the system and the results have been very dependent on the quality of the grid. Table 1 shows the performance parameters for some of the plates run in the last 2 years. The uncertainty column gives the uncertainty derived from the final model fit of the combined data from the four runs. Since the analysis treats any unmodeled systematic error as a random error, and the uncertainty is taken as three times the apparent random error, this error estimate over estimates the true error.

Table 1. Performance parameters.

Calibration	# pts	Size of plate (mm)	Total uncertainty (μm)
E0079	67	200×200	0.64
M2470	133	230×230	0.80
M2463	121	200×200	0.67
M0001	13	200×200	0.36
M0002	13	100×100	0.74
M2340	12	170×100	0.48
M2341	12	170×100	0.70
JSB01	81	115×115	0.33
JSB24	45	120×120	0.45
M2607A	25	600×600	1.12
M2569	25	600×600	0.84

The last plates M2607A and M2569 are plates with 250 μm wide lines. After the four runs of the standard calibration scheme the uncertainty was over 2 μm, a result of the loss of precision inherent in the low magnification. Since the repeatability of the video system is near 1 pixel (3 σ) over a large range of magnifications, lower magnification leads to lower precision in setting the camera over the grid. For normal magnifications, the uncertainty is limited primarily by the accuracy of the coordinate measuring machine, 0.3 to 0.6 μm depending on the thermal behavior of the room during the measurements. Only for very low magnifications is the video system the main source of uncertainty. For these plates the calibration was run again and the data combined. This reduced the random component of the error to an acceptable size.

The overall experience with the system shows that the uncertainty in the calibration is not strongly dependent on the size of the plate, number of points or the size of the grid line. When plates have over 100 points the length of the run becomes long (over 4 hours), and thermal drift becomes a problem. For lines over 40 μm wide there is loss of precision in the video centering, but more runs can reduce the error. Plates over 600 mm on a side cannot be calibrated with the normal analysis software because the machine has only 600 mm of travel in the Y direction. For plates over 300 mm square there is an increase in run time due to the speed of the machine, 200 mm/min, which can allow thermal problems to affect the calibration repeatability.

The best quality grid plates which have been calibrated, JSB01 and JSB24, were calibrated as a test of the absolute accuracy of the system. The plates were first calibrated on the NBS linescale interferometer, a one-dimensional machine which is

capable of calibrating any linescale less than one meter in length. The system is described in detail elsewhere [6,8]. Any line of grid marks on a grid plate of the type used here, less than 15 cm on a side, can be calibrated with uncertainties of less than 0.02 μm. Since this accuracy is nearly an order of magnitude better than the Moore 5 grid plate system, the lines on a grid calibrated on the linescale can be treated as primary length standards. The grids were then recalibrated using the grid plate system.

One change in the normal grid plate software was made for these tests. Since the linescale is a one-dimensional instrument, only two arms of the grid marks are measured. For example, in the grid mark of figure 5, the linescale interferometer would use only the top line of the grid marks for the calibration in one direction, and the right line when the plate was turned to do the orthogonal direction. This measurement will be the same only if all of the grid marks have the same orientation to the measurement axis. In order to prevent any systematic errors due to irregularities in the alignment of the crosses, the video system was programmed to measure only the same two arms of the grid marks that were used by the linescale. Since the grid plate software demands that both arms of the grid mark be on the screen at the same time only a 40 μm length of the line could be used in the fit. Since the linescale used up to 100 μm there might be very small systematic errors due to edge deformities in the edge section not measured by the video system. This effect was not investigated.

To compare the calibrations, the distance between every two points on each line was calculated. For example, for line one of plate one there are nine grid marks one half inch apart. From this line there are eight half inch subintervals, 7 one inch subintervals, 6 one and one half inch subintervals, 5 two inch subintervals, etc. The differences between the grid plate system and the linescale calibrations were averaged by subinterval length and the pooled standard deviation from the average was found for each length. The results are given in tables 2 and 3.

The grid plate analysis program reported a pooled uncertainty of 0.33 μm for plate JSB01. The deviation of the coordinates from the linescale calibration yielded a three times pooled standard deviation of 0.035 μm, a good agreement with the analysis program result.

The same comparison for plate JSB24 found the analysis program uncertainty to be 0.45 μm and the comparison with the linescale calibration gave a 3 σ of 0.38 μm. Both of these results show that the grid plate analysis results are valid estimates of the absolute uncertainty of the calibration.

Table 2. Plate JSB01

Interval length (inches)	Average difference (mm)		Pooled standard deviation (μm)
	X	Y	
0.5	0.01	0.01	0.09
1.0	0.02	0.01	0.09
1.5	0.04	0.04	0.10
2.0	0.06	0.06	0.08
2.5	0.07	0.07	0.08
3.0	0.08	0.07	0.07
3.5	0.08	0.06	0.06
4.0	0.06	0.05	0.05

Table 3. Plate JSB24

Interval length (mm)	Average difference (mm)		Pooled standard deviation (μm)
	X	Y	
20	−0.01	0.02	0.22
40	0.06	0.09	0.31
60	0.12	0.11	0.24
80	0.04	0.13	0.25
100	0.03	0.19	0.24
120	0.02	0.20	0.26

The length dependence of the errors are shown in figure 11. The systematic length dependent part of the error is different for the two plates. The most reasonable explanation of this effect is a result of the small scale errors in the machine geometry. Since the error map interpolates between the data at 2 inch intervals, nonlinear errors in the machine with characteristic length of less than 2 inches will not be corrected. This hypothesis is supported by fact that the characters of the error curves are different. Since the two plates were calibrated at different positions on the machine table, if the small scale errors not contained in the error map are the determining factor the error curves should vary with position on the table. Had the error curves been very similar an error source independent of the small scale geometric errors of the machine, for example the laser wavelength corrections or temperature scale, would be suspect.

It is possible to reduce this source of error by measuring the plate in random positions on the table, thereby averaging out the geometric errors. From tables 2 and 3 it can be seen that the random errors as estimated by the three times the pooled standard deviation are somewhat larger than the

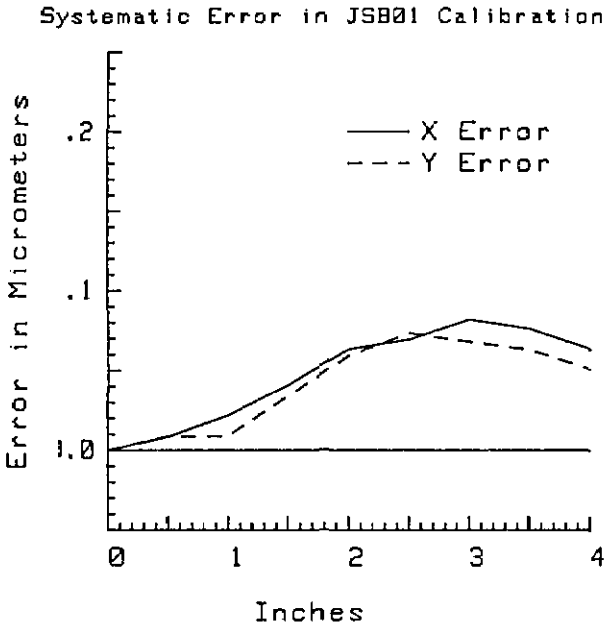

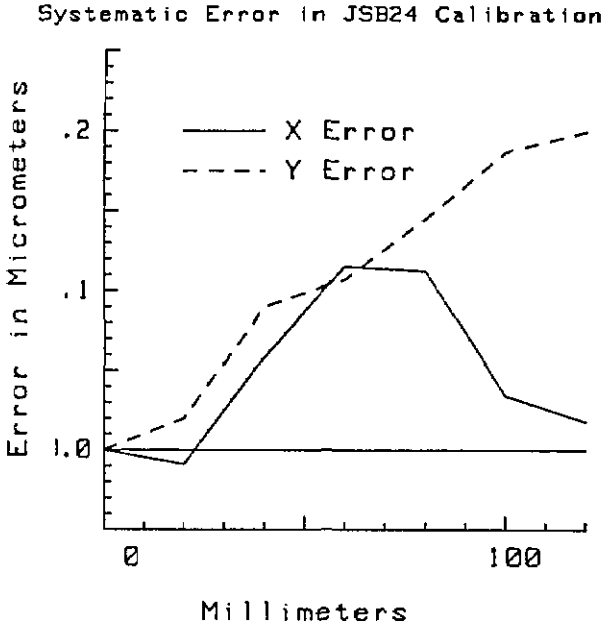

Figure 11. Systematic error in the calibration of two grid plates. These plots show the average difference between the two-dimensional grid plate system and the linescale interferometer measurements.

systematic errors as determined by the comparison to the linescale interferometer data, some gain might be made.

6. Outlook

Given the current performance level of the machine and the known limitations of the calibration method, there are a number of changes which would improve the accuracy and uncertainty of the grid plate calibrations.

The video system, under best conditions, has a reproducibility of about 0.02 μm (1 σ). This level has been found for a number of small grid plate runs, where the thermal properties of the machine were very stable and the calibration run limited to 10 to 15 minutes. Increasing the speed of the machine motion, the video processing, and the thermal stability of the system could make this precision routine for most grid plates of less than 6 inches square.

If the error map were perfect, combining runs with different orientations or positions on the table would not increase the measured random error. The unmodeled systematic error in the machine, measured by the difference between the pooled standard deviations of the runs in the same orientation and the pooled standard deviation found when all of the runs combined, is generally 0.03 to 0.05 μm. This error is probably irreducible without physical changes in the machine.

Currently under study are plans to upgrade the performance of the machine by a major refit of the control system and improvement of the way geometry to reduce the nonrigid body motions of the machine. With added speed and small improvements in the thermal stability of the room, it may be possible to produce calibrations routinely at a level closer to the combination of the minimum errors of the separate system components, about 0.15 μm.

7. Acknowledgment

I would like to thank Mr. John Beers for the use of his linescale interferometer calibration, and Dr. Tyler Estler for permission to use his stability data in figure 3.

About the author: Theodore D. Doiron serves with the Precision Engineering Division in the Center for Manufacturing Engineering, NBS.

References

[1] Hocken, R. J., and Borchardt, B. R., On Characterizing Measuring Machine Geometry, Natl. Bur. Stand. (U.S.) NBSIR 79-1752 (1979).
[2] Hocken, R. J., Simpson, J., Borchardt, B., Lazar, J., Reeve, C., and Stein, P., Three Dimensional Metrology, Ann. CIRP 26 (1977).
[3] Estler, W. Tyler, High-accuracy displacement interferometry in air, Appl. Optics 24, 808–815 (1985).
[4] Beers, J. S., and Lee, Kang B., Interferometric measurement of length scales at the National Bureau of Standards, Precis. Eng. 4, 205–214 (1982).
[5] Loewen, E. G., and Burns, R. H., An Interferometric Scale and Grid Comparator, Ann. CIRP 19, 597–602 (1971).
[6] Reeve, C., A Method of Calibrating a Two Dimensional Reference Plates, Natl. Bur. Stand. (U.S.) NBSIR 74-532 (1979).
[7] Raugh, M. R., Absolute two-dimensional sub-micron metrology for electron beam lithography, Precis. Eng. 7, 3–14 (1985).
[8] Doiron, T., The Calibration of Gridplates at the National Bureau of Standards, Proc. Int. Symp. Metrology and Quality Control in Production, Tokyo (1984).

Volume 93, Number 1, January-February 1988
Journal of Research of the National Bureau of Standards

Phase Meter Calibration at NBS

Volume 93 Number 1 January-February 1988

Raymond S. Turgel

National Bureau of Standards
Gaithersburg, MD 20899

To provide a phase meter calibration service, a phase angle calibration standard has been developed at NBS. This standard is a signal generator with two sinusoidal outputs and uses direct digital synthesis to generate the signals. The phase angle between the two sinusoids is determined by the input parameters in the calculation of the sets of digital values from which the analog output is synthesized. An auto-zero compensation mode corrects for residual phase differences in the two output channels. The phase resolution is better than 0.002° over a frequency range from 2 Hz to 5 kHz and 0.005° from 5 to 50 kHz. Phase meter calibration data are fitted to a linear model from which appropriate corrections for the phase meter readings can be derived. Statistical treatment of the data provides an estimate of the uncertainty of the corrected phase meter readings relative to the phase angle calibration standard.

Key words: calibration; calibration uncertainty; direct digital synthesis; phase angle; phase angle standard; phase meter.

Accepted: September 9, 1987

Introduction

Phase angle is the quantity that describes the time relationship between waveforms of two ac signals of the same frequency. Phase meters that measure this angle have a wide range of applications in industry and the laboratory. In electric generating stations phase meters are used to check the distribution circuits; in navigational equipment, measuring the phase angle provides a method of determining the bearing with respect to a ground coordinate system; in industry, many positional displacements are monitored by determining the electrical phase angle, and phase shift is an important design parameter of electronic amplifiers and other circuitry. While developments of phase meters have moved along with progress in instrumentation technology, until recently, accurate phase meter calibration had to contend with more traditional and rather time consuming procedures, requiring many steps to make a single measurement.

Phase Meter Calibration

To establish a precision phase meter calibration service at NBS, it was concluded that refinement of traditional methods did not seem to offer possibilities for the desired significant improvement. To improve the state of the art, a new approach was needed. In an ideal calibration arrangement, the meter to be calibrated is connected directly to a calibrator which can be set for the appropriate test conditions. The meter output is then compared to the value furnished by the calibrator (standard). In many cases this simple set-up cannot be realized in practice, but for the phase meter calibration the aim has been to approach this simple concept as closely as possible.

For the precision calibration of a phase meter, two sinusoidal signals of the same frequency are needed that have very low distortion and are displaced by a very stable, precisely known phase angle. The low distortion sinusoidal test signal is

desirable because the phase angle, strictly speaking, is defined only if the two waveforms are identical, and it is extremely difficult to ascertain the exact equality, in both amplitude and relative phase, of the components of complex waveforms. Thus, in practice, precision phase measurements are meaningful only for signals with low distortion. Various designs of phase meters discriminate against harmonics in different ways, so that a distorted signal may yield measurement results that differ from one type of meter to another, a condition which is clearly unacceptable for a general calibration service.

Principle of the Phase Angle Calibration Standard

With the above consideration in mind, the test signal requirement can best be fulfilled by a special high purity, dual-channel signal source and some highly accurate means to determine the phase angle between the two outputs. Prior experience with digital signal processing circuitry indicated that application of digital techniques to analog measurements would provide advantages that could not easily be achieved by purely analog methods. By combining the inherent stability and predictable precision of digital calculations with digital-to-analog converters, it is possible to generate the desired pair of pure sinusoidal waveforms necessary for the calibration of a phase meter and, at the same time, determine the phase angle with the desired accuracy.

The output of the dual-channel signal generator is provided by a pair of fast digital-to-analog converters that translate numerical input data into analog output voltages. The required numerical values for each waveform are calculated point-by-point, using a high-speed microprocessor, and then converted into corresponding analog output voltages. The resulting discrete output voltages form a stepped waveform which is then passed through smoothing filters and amplified to provide a sinusoidal signal. This method of direct digital synthesis is analogous to graphical construction of functions by plotting them point-by-point.

The desired phase relationship of the two output signals is achieved by carrying out the digital-to-analog conversion of each point on one waveform simultaneously with the conversion of a corresponding point on the other waveform (see fig. 1). Since each waveform is uniquely determined by the set of calculated numerical values that make up the sample points, the waveforms can be displaced relative to one another to yield the desired phase angle, by choosing appropriate parameters for the calculations. Hence, the phase angle is essentially determined by a mathematical algorithm and is, therefore, accurately known and drift free. When generated by this method, the phase angle is not affected by the limitations and problems associated with analog phase shifters which are dependent on the stability of their electronic components and the operating frequency. Additional advantages of direct digital synthesis are the excellent repeatability, stability, and low distortion of the waveforms.

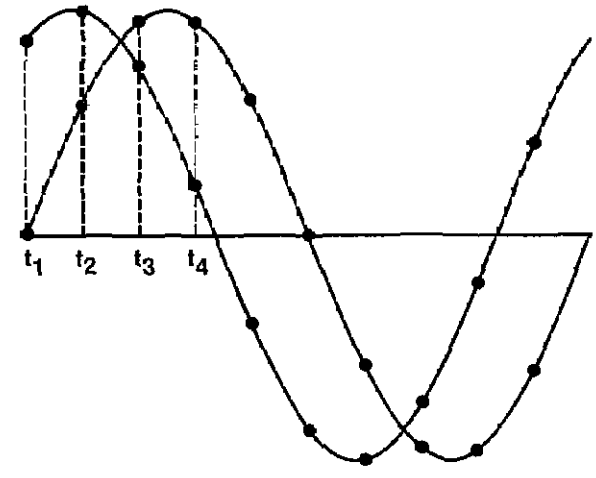

Figure 1. Waveform synthesis with uniform sampling.

Phase Standard Prototype

Based on the principles of signal generation outlined above, NBS built three prototypes of a phase angle calibration standard, one for its own use, the others for the Department of Defense. The construction and circuits of the NBS Phase Angle Standard are described in detail in the literature [1–4]. The standard uses two embedded microprocessors (see fig. 2), a high-speed, bit-slice microprocessor to generate the waveforms and a second conventional microprocessor to control the rest of the system, performing functions such as setting the desired test parameters (phase angle, frequency, and amplitude in each channel), as well as performing auxiliary functions associated with a parameter display, error correction, and communication with the IEEE-488 instrumentation bus.

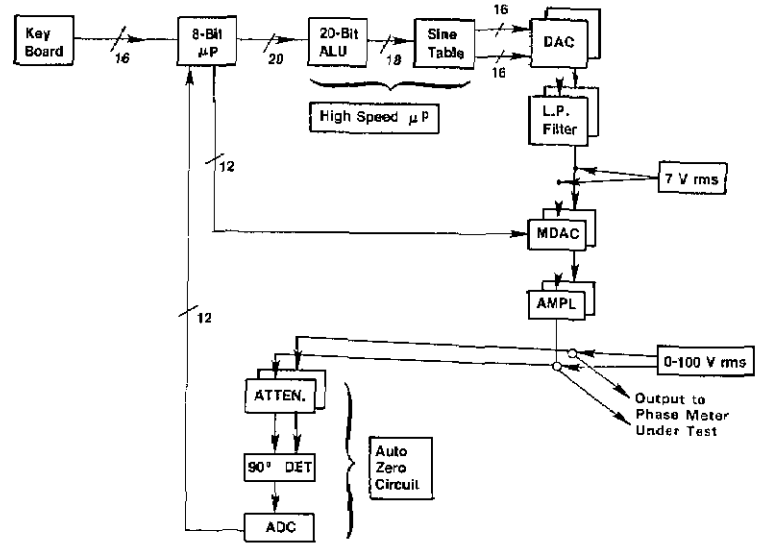

Figure 2. Functional block diagram of NBS phase standard.

Waveform Generation

All calculations connected with the direct digital synthesis of the two output waveforms is carried out in a bit-slice, 20-bit wide microprocessor. Twenty bits (including a sign bit as most significant bit and a guard bit as least significant bit) are needed to obtain slightly better than 0.002° resolution in phase angle over a ±999.999° span. The location along the time axis, t_i, of each sample point on the waveform can be expressed as an equivalent phase angle relative to the positive-going zero crossing of the sinusoid (see fig. 1). These angles are calculated by successively adding a constant angular increment (equivalent to uniform sampling in time) to some selected starting value. The size of the angular increment is determined by the number of sample points per waveform.

At each point, the instantaneous amplitude is computed using the sine function with the corresponding equivalent angle as argument. A special hardware module provides these angle-to-sine conversions, with 16-bit output resolution, in less than 400 nanoseconds, which allows all computations to be carried out in real time for signal frequencies up to 5 kHz. For signal frequencies from 5 to 50 kHz, where the number of samples for each period of the waveform never exceeds 512, sets of numerical data for the two waveforms are calculated only once for each change of frequency or phase angle and are then stored in memory. From memory, the sample data can be transferred rapidly, at rates from two to four million per second, to 12-bit, high-speed analog-to-digital converters.

The number of sample points per waveform is chosen so that the rate at which the numerical data are converted into corresponding voltages remains in a band from 200 to 400 kHz for output frequencies up to 5 kHz and in a band from 2 to 4 MHz above 5 kHz. With these choices a single low-pass filter for the 16-bit (low-frequency) channel and a single low-pass filter for the 12-bit (high-frequency) channel is sufficient for all output frequencies. To provide acceptable waveform purity the minimum number of samples is 64 (at 5 and 50 kHz, respectively). To keep within the constraints of the conversion rate, the number of samples is doubled when the output frequency selected is halved. Thus, at 2 Hz the waveform is reconstructed using 131072 ($=64\times2^{11}$) samples. The large number of sample points results in excellent spectral purity, but makes storing the set of data uneconomical and thus requires real-time computation.

Frequency Selection

The frequency band of the phase standard extends from 2 to 50 kHz, adjustable in steps of 1 Hz for frequencies up to 5 kHz and adjustable in steps of 10 Hz from 5 to 50 kHz. Operationally, the two frequency ranges differ, although the difference is essentially transparent to the user. In the lower range data computed in real-time are applied to 16-bit digital-to-analog converters, and in the upper range, as explained above, stored data are applied to higher speed 12-bit converters. In either case

the timing pulse that transfers the data to the converters is obtained from a frequency synthesizer which is independent of the microprocessor clock. This method permits synchronization of the output signal with an external source. The frequency and phase information entered through the keyboard or via the IEEE-488 bus, is transferred to the waveform generating computer at the beginning of every cycle of the output signal, thus providing almost instantaneous response. Reinitializing the waveform generating computation at the beginning of every cycle of the output also prevents spurious errors from being propagated for more than one cycle.

Amplitude Control

Phase meters are often used with signals of unequal amplitudes at the two inputs. It is therefore desirable to be able to test and calibrate them under those conditions. The phase angle standard uses programmable attenuators ahead of amplifiers which are capable of supplying a seven-volt rms output. For voltages up to 100 volts, an additional internal, fixed-gain amplifier is switched into the circuit. The amplitude of each output channel is independently controllable. For those phase meters requiring current inputs, auxiliary transconductance amplifiers [5] capable of supplying up to five amperes can be connected externally.

Automatic Phase Compensation (Auto-Zero)

An important feature needed to assure the accuracy of the NBS phase angle calibration standard is an automated procedure that checks the output phase angle and corrects for small residual differential phase offsets. These phase offsets arise because, in practice, the amplifier and filter circuits in the two output channels, although carefully matched, cannot be made to be truly identical. Using circuitry internal to the phase angle standard, the procedure establishes a true 90° phase angle as a reference, compares it to the nominal 90° phase angle of the output signals, and, in several iterations, calculates and applies a phase angle correction to the waveform generating processor.

The method is based on a quadrature phase detector circuit [6] which has a voltage output proportional to the cosine of the phase angle between the two inputs and which is nominally zero when the input signals are exactly 90° out of phase. To eliminate any errors that might be introduced by the phase director itself, during every iteration measurements are made at +90° and −90° and again with the signal channels interchanged. This set of four measurements compensates for dc offsets as well as phase offsets in the detector, effectively making it behave like an ideal component.

The final value of the correction is stored in the memory of the microprocessor and is then automatically applied to any selected phase angle settings used for the calibration of the phase meter. The auto-zero compensation needs to be redetermined every time the amplitude of either channel is changed, or if the frequency is shifted between ranges (see below). Within each frequency range, the compensation is adjusted by interpolation.

Accuracy

In an ideal phase angle standard there is a one-to-one correspondence between the phase angle of the output signals and the setting of the standard. In the actual implementation of the standard, there will be departures from this ideal relationship. These departures can be attributed to several causes, some of which are predictable, while others are subject to the random effects of noise.

One of the predictable effects is the rounding error. The keyboard entry of the phase angle is in decimal form, in steps of 0.001°, while the internal calculations are carried out in a binary number system with an equivalent resolution of 0.00137...°. Therefore, not every keyboard setting corresponds to a unique binary value for the angle. Furthermore, at the upper limit of the frequency range, when using 12-bit converters and 64 sample points per waveform, it can be shown [4] that the phase angle resolution of the output signals, which is theoretically possible under these conditions, is closer to 0.005°.

Another contributing factor to the departure from the ideal model of the phase standard is the difference between the actual and theoretical response characteristics of the particular digital-to-analog converters used. Non-linearities in these characteristics result in slight waveform distortions which degrade the accuracy of the phase angle. Although, by measuring the converter response carefully, it might be possible to evaluate the error at any particular phase angle, the number of calculations would be too large to make this practical as a general approach. Instead, an estimate of the limits of the departure from linearity of the

relationship between output phase angle and setting of the standard can be obtained by a limited series of measurements. From these an estimate of the uncertainty in the assignment of the phase angle of the output of the standard can be derived.

One of the random factors that influence the phase standard accuracy is a residual phase offset that remains after the auto-zero procedure attempts to compensate for offsets due to small mismatches in the amplifiers and filter characteristics. The determination of the value of this auto-zero correction by the system is dependent on feedback to the signal generating processor of numerical data from the results of repeated measurements with the quadrature detector. Since each measurement is affected by noise in the system, the auto-zero compensation may not settle to the same endpoint every time, and it therefore introduces some random uncertainty into the value of the phase angle. The magnitude of that uncertainty depends on the amplitudes of the signal as well as on the frequency.

At frequencies below 1 kHz the corrections are relatively small, only slightly larger than the angular resolution of the standard. With increased frequency, all of the effects are more pronounced. A fuller discussion is given in [2] and [4]. Specifications shown in table 1 are based on experimentally determined accuracies of the three prototype phase standards built at NBS.

Table 1. Performance specifications based on measurements of NBS prototypes

Phase Angle:	
Range	−999.999 to +999.999 degrees
Resolution	0.0014 degrees (1 part in 2^{18})
Systematic uncertainty (equal amplitude)	
at 60 Hz	0.003 degrees
at 400 Hz	0.004 degrees
at 5 kHz	0.008 degrees
at 15 kHz	0.016 degrees
at 30 kHz	0.027 degrees
at 50 kHz	0.040 degrees
Systematic uncertainty (amplitude ratio 7:1)	
at 60 Hz	0.004 degrees
at 400 Hz	0.006 degrees
at 5 kHz	0.011 degrees
at 50 kHz	0.080 degrees
Output frequency:	
Range	2 Hz to 50 kHz
Resolution	1 Hz up to 5 kHz; 10 Hz above 5 kHz
Accuracy	0.06%
Stability	1 ppm
Output amplitude:	
Effective range	0.5 to 100.0 V rms
Resolution	steps of approx. 2 mV, up to 7 V steps of approx. 24 mV, 7 to 100 V
Accuracy	0.1%
dc offset voltage	< 0.5 mV for outputs to 7 V rms < 5 mV for outputs 7 to 100 V rms

Accuracy Verification

An important part of any reference standard is the verification of its own accuracy. To understand what is involved in the case of a phase angle standard, one has to consider the "three-dimensional measurement space" that encompasses phase angles, frequencies, and amplitudes. There is an infinity of possible test points that obviously cannot all be covered. The two main parameters that need checking on various ranges are the linearity and the offset compensation.

Of these, the offset compensation is most readily measured. A bridge circuit can be constructed in which the two signal generating channels of the standard, which have a common ground terminal, are configured as two arms of the bridge and two suitable impedances, connected in series across from one output terminal of the standard to the other, comprise the other two arms. A null detector is then connected from the junction of the two impedances to the ground terminal of the standard. Since two of the arms are active (and coherent) signal sources, no other supply is needed. To improve the signal-to-noise ratio the detector is tuned to the operating frequency. For the lower frequency range, the impedances consist of the windings of an inductive divider, and for the higher frequency range two three-terminal, variable air capacitors are used.

To balance the bridge both the ratio of the external impedances and the relative phase of the two output signals from the phase angle standard must be adjusted. The angular offset from the nominal 180° is the phase error of the standard. Additionally, the quadrature phase error of the standard can be checked with an external quadrature detector using a method similar to that of the auto-zero procedure.

Linearity tests can be carried out by a variety of procedures. In the vicinity of 90° and near the 180°-point, using the quadrature detector or the bridge circuit, respectively, off-null voltage readings on the detector should be proportional to the angular deviation from 90° or 180°. This holds true as long as the angular deviation is small enough so that the sine of the (deviation) angle is equal to the angle (in radians), within the required accuracy. A more general but very time consuming method, applicable at any phase angle, makes use of a fixed ($\simeq 1°$) and a variable phase (0° to 360°) shifter inserted into one arm of a 180° bridge. At various phase angles, the bridge is first balanced with only the variable phase shifter in the circuit. Then, with both the fixed and the variable phase shifters in the circuit, the incremental phase adjustment of the standard needed to rebalance the bridge is determined. A somewhat simpler version of this method makes use of the independent phase adjustment of the two output channels, instead of added phase shifters, to obtain bridge balances with one channel set at a phase angle ϕ (relative to an internal reference common to both channels) and the other channel at $(\phi + 180° + \delta)$, where δ represents the linearity error. Detailed discussions can be found in references [3] and [4].

Phase Meter Calibration

Using the NBS phase angle standard, phase meter calibrations can be carried out with significant savings in time and effort even in the manual mode. To make full use of its potential, however, the calibration system should be operated from an instrument controller (computer) via the instrumentation (IEEE-488) bus.

For its phase meter calibration service, NBS has developed a phase meter calibration program that combines automatiac control of the phase standard with statistical analysis of the calibrations results. The projected service will be described in an NBS Special Publication which is in preparation [7].

The phase meter is directly connected to the phase standard if the meter ranges match the output capability of the standard (0.5 to 100 volts rms, 2 to 50 kHz). If higher voltages (240 volts rms) or currents (0.05 to 5 amperes) are required, special auxiliary amplifiers with known phase offsets are added. On every selected range, phase angle test points are selected by the operator. Experience has shown that satisfactory accuracy can be obtained with 12 test points covering the span from 0° to 360°.

The program then proceeds with the calibration measurements by setting the phase angle standard to the desired value. To minimize the effect of time dependent drifts, the order of the test points (including repeat measurements) is randomized, and when the sequence is completed, every selected phase angle will have been measured at least four times. The phase meter reading can be entered manually through the controller keyboard, or if provided for, automatically via the IEEE-488 bus. All data are stored on magnetic disk or tape.

Parameters derived from the replicate calibration readings make possible a statistical test of whether the phase meter characteristic can be represented by a linear relationship, or is significantly

non-linear. Further statistical tests establish whether the modeled linear response characteristic significantly differs from the ideal. On the basis of this statistical evaluation, suitable calibration corrections can then be assigned to bring the meter readings into agreement with the standard [8].

The modeled response characteristic (calibration curve) derived from the statistical treatment of the calibration data, generally provides a better basis for computing the corrections than that obtained by simply averaging data from each test point. The NBS Calibration Report provides full information on the computation for the corrected values, as well as some statistical background.

Other Applications of the Phase Angle Standard

Because of its excellent phase and waveform stability, the phase standard has found applications not immediately related to its phase meter calibration function, and it has formed the basis for further specialized instrumentation development. For instance, with auxiliary voltage and current amplifiers, the phase standard can be used as a stable, easily adjustable signal source for checking wattmeters and watthour meters [9,10]. It can also be used to test various signal analyzers that need a phase-variable reference. In another application, the special properties of the two-signal, phase-variable source provided by the standard have resulted in the development of new techniques and new configurations for ac impedance bridge measurements.

Trends in Precision Measurement Instrumentation

In recent years, developments in precision instrumentation have shifted the burden of making successful measurements more and more from man to machine. Instead of relying entirely on personal skills and conscientiousness of the experimenter, the execution of the task has been transferred to the software of a system using external instrument controllers and embedded microprocessors. In line with this trend, the responsibility for the ultimate accuracy has shifted, at least in part, from the person performing the measurement to the instrument designer and software engineer who devise the measurement process. The aim in this development has been to eliminate the tedium of repetitive manual operations and prevent associated fatigue induced errors. At the same time, the overall efficiency and accuracy can be improved by refinements in the measurement process.

However, this increased reliance on the instrumentation is sound only if the instruments perform flawlessly, since the skilled judgement of the experimenter ostensibly has been replaced by the automated process. To assure continued success in meeting the objective of accuracy in measurements when using automated systems, greater importance must be given to the activities which support the instrumentation. Calibration is one of these support activities, assuring that the results obtained conform to accepted measurement standards and that the instrument is functioning properly.

Traditionally, calibration has been a very labor-intensive activity. In many areas, particularly those where the volume of calibrations is high, older manual laboratory methods have already been successfully replaced by automated electronics; for instance, the replacement of volt boxes and potentiometers by electronic voltage standards for voltage calibration. In other areas, where the economic pressure is perhaps less pronounced, innovations in calibration of phase meters is one of those areas.

About the author: Raymond S. Turgel is a physicist in the Electrosystems Division of the NBS Center for Electronics and Electrical Engineering.

References

[1] Turgel, R. S., Oldham, N. M., Stenbakken, G. N., and Kibalo, T. H., NBS Phase Angle Calibration Standard, Natl. Bur. Stand. (U.S.) Tech. Note 1144 (July 1981).
[2] Turgel, R. S., NBS 50 kHz Phase Angle Calibration Standard, Natl. Bur. Stand. (U.S.) Tech. Note 1220 (Apr. 1986).
[3] Turgel, R. S., and Oldham, N. M., High-Precision Audio-Frequency Phase Calibration Standard, IEEE Transactions on Instrumentation and Measurement IM-27, No. 4, 460–464 (Dec. 1978).
[4] Turgel, R. S., A Precision Phase Angle Calibration Standard for Frequencies up to 50 kHz, IEEE Transactions on Instrumentation and Measurement IM-34, No. 4, 509–516 (Dec. 1985).
[5] Laug, O. B., A Wideband Transconductance Amplifier for Current Calibrations, IEEE Transactions on Instrumentation and Measurement IM-34, No. 4, 639-643 (Dec. 1985).
[6] Marzetta, L. A., A High Performance Phase-Sensitive Detector, IEEE Transactions on Instrumentation and Measurement IM-27, No. 4, 460–464 (Dec. 1978).
[7] Turgel, R. S., Mulrow, J. M., and Vecchia, D. F., NBS Phase Angle Calibration Services, Natl. Bur. Stand. (U.S.) Spec. Publ., in preparation.

[8] Turgel, R. S., and Vecchia, D. F., Precision Calibration of Phase Meters, IEEE Transactions on Instrumentation and Measurement IM-36, No. 4, 918–922 (Dec. 1987).
[9] Oldham, N. M., Power Calibration Standard Based on Digitally Synthesized Sinewaves, IEEE Trans. Power Appar. Syst. PAS-104, No. 11, 3117–3121 (Nov. 1985).
[10] Oldham, N. M., and Turgel, R. S., A Power Factor Using Digital Waveform Generation, IEEE Trans. Power Appar. Syst. PAS-100, No. 11, 4435–4438 (Nov. 1981).

Volume 93, Number 1, January–February 1988
Journal of Research of the National Bureau of Standards

The Application of Flame Spread Theory to Predict Material Performance

Volume 93 Number 1 January–February 1988

J. G. Quintiere

National Bureau of Standards
Gaithersburg, MD 20899

A review is presented of recent work which attempts to apply flame spread theories to a wide range of materials. The approach is based on using the theories to develop correlations from material data. The data are derived from small scale tests and are expressed in terms of "properties." Various radiant heating apparatus are discussed, and a wide range of results are presented. The focus of the application is fire spread on walls.

Key words: flame spread; heat transfer; ignition; material properties; small scale fire tests; thermal radiation.

Accepted: July 23, 1987

Introduction

There are many different tests for assessing the flammability of materials. In most cases these tests are for the purpose of evaluating interior finish materials and products, particularly wall and ceiling applications. In general, all of the tests express their results in terms of some observations or measurements. These are then used to derive a relative ranking scale on which to evaluate materials. Unfortunately, the bases of these ranking scales are arbitrary, and therefore results from one test do not necessarily agree with another. Each test measures some combination or aspect of flammability; namely, ignition, flame spread, and energy release. But none attempts to relate their measured test results to theories of ignition, spread or combustion. Consequently, the test results are limited in their use, but often widely applied.

This practice is in sharp contrast to the evaluation of material performance in other fields. If we are interested in the heat transfer characteristics of materials, we seek their thermal properties. If we are interested in the strength of materials, we would seek their modulus of elasticity and yield stress. Then we would seek to understand how the material is to be used and analyze that configuration based on the principles of heat transfer or structural analysis. If the materials were complex in form, we would expect the property data to be "effective" since the engineering analysis we would use would most likely be based on a model for simple homogeneous materials. For example, a measured thermal conductivity of a foam material would represent all the underlying heat transfer processes in the foam. Its measured thermal conductivity would not be that of the pure material or the entrapped air in the foamed material, but it would be an "effective" value based on Fourier's law of heat conduction applied to the foam. Obviously, the effects on a material in a fire are more complex than this. But by using simple theories based on scientific analysis, we should be able to derive and utilize "effective" property data in an analogous fashion.

In this presentation, "simple" theories for ignition and flame spread will be examined in order to elucidate appropriate material properties for these phenomena. The theoretical equations will serve to provide a basis for analyzing test results for the

materials. Experimental correlations for a particular ignition or flame spread process, when based on theory, would then yield values for the parameters of the theory. As long as these parameters remain reasonably constant over an appropriate range of conditions, or correspond to true material properties ideally, we can consider them to be "effective" property values for the processes of ignition and flame spread. In this way, we seek to develop test procedures to measure "effective material fire properties." Furthermore, when combined with theory, these properties can be used over a wide range of fire conditions for predicting aspects of ignition and flame spread.

The principal focus for much of the work has been on fire spread over wall materials. Hence the materials are vertically oriented. The relationship to ignition and spread on horizontal materials will be examined under limited circumstances. Only piloted ignition was considered since it will be shown to bear directly on flame spread. Lateral (or horizontal) flame spread data were considered under conditions of natural convection for many materials under a wide range of radiant heating. For some materials, results were compared to downward flame spread under the same heating conditions. A special apparatus was used to measure flame height and heat transfer relevant to upward flame spread. These results were then used to examine aspects of upward flame spread on two different materials—polymethylmethacrylate (PMMA) and Douglas fir particle board.

Theoretical Aspects

A theoretical basis is sought that is simple in application, yet sufficient for predicting a material's performance. The theory should be consistent with more fundamental analyses. We could turn directly to results in the literature on fundamental aspects of flame spread, but these generally ignore the effects of external heating. Since most materials require external heating (under normal oxygen conditions) to enable flame spread, this will be a necessary part of a test to derive flame spread data.

Without a loss in generality of the end results, a thermal theory of flame spread (and ignition) will be considered. The diagram in figure 1 shows a flame spreading over the surface in the x-direction. The flame is depicted as if it is being blown by a wind. The fuel is burned out over region x_b, pyrolyzing over region $x_p - x_b$, and no degradation or vaporization occurs for $x > x_p$. The tip of the flame is given by x_f and the surface ahead of the pyrolyzing region receives most of the flame heat transfer over this region $(x_f - x_p)$. The initial temperature is given by T_∞ and the pyrolysis front x_p is defined by the position where the temperature achieves the ignition temperature (T_{ig}) on the surface.

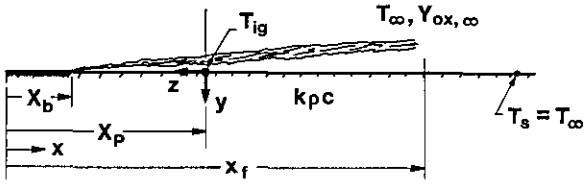

Figure 1. Model for flame spread.

For steady flame spread without external heating it is usually common to define a new coordinate system moving with x_p. With external heat transfer it is better to consider a fixed position x and only one-dimensional conduction in the y-direction. The latter approach will be taken. Also we will consider that the heat flux from the flame $\dot{q}_f''$ is constant and uniform over the time period Δt before x_p reaches the position x; and that the flame spread velocity $V_p = dx_p/dt$ is also constant in this period. Furthermore, Δt is defined to be equal to $(x_f - x_p)/V_p$ where the flame heat flux is applied only over the region $x_f - x_p$. It will turn out that the general form of the result derived under these conditions will be equivalent with analyses for both wind-aided or opposed flow flame spread conditions. The distinction will lie in how we interpret $\dot{q}_f''$ and $x_f - x_p$. Also since it will turn out that V_p will generally vary with time, the assumptions just imposed can be regarded as quasisteady in that at any position $x = x_p$, the velocity is considered constant in its vicinity.

Let us consider the case of a semi-infinite solid. This will result in the thermally-thick case which can be shown to apply to most common organic solids $(k/\rho c \sim O(10^{-3}) cm^2/s)$ in applications of construction. This follows since the depth of heating due to the flame (or for conditions of ignition) would be O(2) to O(5)mm so that materials of thicknesses greater than this, or of a combined thickness with a substrate material greater than this, would apply to the semi-infinite result. The problem can then be posed as follows:

at position x,

$$y = 0, \quad -k\frac{\partial T}{\partial y} = \dot{q}''(x,t) + h(T - T_\infty) \tag{1}$$

$$y \to \infty, \quad T = T_\infty \tag{2}$$

$$t=0,\ T=T_\infty \tag{3}$$

where $\dot{q}''(x,t)=\dot{q}_f''+\dot{q}_e''$. (4)

The flame heat flux is defined as described above, and $\dot{q}_e''$ can be a function of x and t. The governing equation is given as

$$\frac{\partial T}{\partial t}=\frac{k}{\rho c}\frac{\partial^2 T}{\partial y^2}, \tag{5}$$

where k, ρ, and c are the conductivity, density and specific heat, respectively. This can be solved for the stated conditions. The heat loss, although expressed in a linearized form where the coefficient h is constant can be thought of physically as a radiative surface loss under wind-aided conditions or both a radiative and convective loss under opposed flow conditions. A solution to this problem was developed previously [1]. By examining the solution for the surface temperature at $y=0$ and imposing the condition that the pyrolysis front reaches x (i.e., $x=x_p$) when $T=T_{ig}$, it can be shown that

$$T_{ig}-T_\infty=\frac{\dot{q}_f''}{h}(1-\exp\beta\ \mathrm{erfc}\sqrt{\beta}) + \int_0^\tau \frac{\dot{q}_e''(x_p,\tau')}{h}\left[\frac{1}{\sqrt{\pi(\tau-\tau')}} - \exp(\tau-\tau')\mathrm{erfc}\sqrt{(\tau-\tau')}\right]d\tau', \tag{6}$$

where $\tau=\frac{h^2 t}{k\rho c}$, (7)

and $\beta=\frac{h^2}{k\rho c}\frac{(x_f-x_p)}{V_p}$. (8)

This result implies that the required temperature rise for flame spread at $x=x_p$ needs to be composed of a contribution from the flame ($\dot{q}_f''$) and a contribution from the surroundings ($\dot{q}_e''$). For the special case where $\dot{q}_e''$ is only a function of x, and where β is small, or equivalently heat losses are ignored or are unimportant with respect to the flame heating component, it can be shown that

$$T_{ig}-T_\infty=\frac{2\dot{q}_f''\sqrt{(x_f-x_p)}}{\sqrt{\pi\, k\rho c\, V_p}} + \frac{\dot{q}_e''(x_p)}{h}(1-\exp(\tau)\,\mathrm{erfc}\sqrt{\tau}). \tag{9}$$

This will be the governing equation for flame spread. It can be rearranged to express V_p explicitly as follows

$$V_p=\frac{(\dot{q}_f'')^2(x_f-x_p)}{\frac{\pi}{4}k\rho c\,(T_{ig}-T_s)^2}, \tag{10}$$

where $T_s-T_\infty\equiv\frac{\dot{q}_s''(x_p)}{h}[1-\exp(\tau)\mathrm{erfc}\sqrt{\tau}]$, (11)

or T_s-T_∞ is the temperature rise due to the external heating.

For the case of pure ignition with a pilot that serves to ignite the flammable mixture, but imparts no heat to the solid itself, a thermal model would yield similar results. Indeed, it follows directly from eq (11) that for radiative ignition

$$T_{ig}-T_\infty=\frac{\dot{q}_e''}{h}[1-\exp(\tau)\mathrm{erfc}\sqrt{\tau}], \tag{12}$$

where the minimum heat flux for ignition would be $\dot{q}_{0,ig}''\equiv h(T_{ig}-T_\infty)$.

These results provide a framework for identifying specific ingredients one needs in order to predict flame spread or radiative ignition for materials. From eq (10) it is seen that the material "properties" $k\rho c$ and T_{ig} need to be determined. The quantity $k\rho c$ may be available for some materials, but it will depend on temperature and consequently values at normal atmospheric temperature will not directly apply. Moreover, it should be noted that both k and c tend to increase generally for solids with temperature. Also $k\rho c$ expresses the heat loss aspect of the solid and the thermal model ignores any pyrolysis effect, so that $k\rho c$ as used here must also represent some heat loss due to pyrolysis. Hence $k\rho c$ is an effective property.

The ignition temperature represents the surface temperature required to produce a flammable mixture just at the lower flammable limit for the flow and flame or ignition conditions under consideration. Under similar flow (or mixing) conditions we would expect the ignition temperature to be roughly a constant for a given material over the range of heating conditions relevant here of roughly 1 to 6 W/cm^2. Although it is difficult to measure the surface temperature at ignition, it is possible to infer an (effective) ignition temperature by determining experimentally the critical radiative heat flux for piloted ignition, i.e.,

$$\dot{q}_{0,ig}''=h_c(T_{ig}-T_\infty)+\sigma(T_{ig}^4-T_\infty^4)\equiv h(T_{ig}-T_\infty), \tag{13}$$

where here a black surface has been assumed, and the convective coefficient h_c explicitly represents the effect of the specific flow or orientation conditions of the process. An ignition temperature as determined in this way is the one required by the thermal models given above for both ignition and flame spread.

Finally, the parameters $\dot{q}_f''$ and $x_f - x_p$ represent the flame heat flux and flame length (extension beyond the pyrolysis zone). These are not properties in the obvious sense. We need to examine these more closely for specific cases of flame spread.

Ignition

We have utilized a device [2,3] which imposes a constant and uniform heat flux over a vertically mounted sample. The sample is backed by an inert insulating material and a pilot flame acts above the sample adjacent to a contiguous wall. This is shown in figure 2. The sample face is approximately 10×15 cm high.

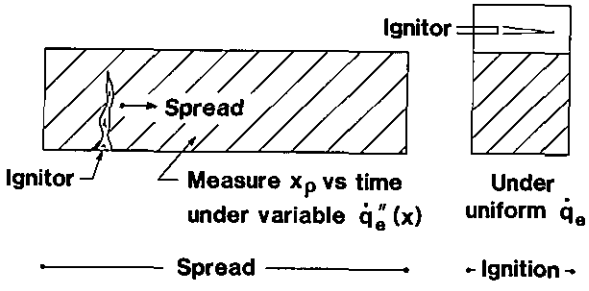

Figure 2. Schematic of apparatus to measure ignition and lateral flame spread.

By conducting experiments at various levels of $\dot{q}_e''$ the times to ignite can be determined. Also, by bracketing, the critical ignition flux can be determined. It has been found that for many materials [2,3], these experimental results can be correlated by the following relationship:

$$\frac{\dot{q}_{0,ig}''}{\dot{q}_e''} = F(t) = \begin{pmatrix} b\sqrt{t}, & t \leqslant t^* \\ 1, & t \geqslant t^* \end{pmatrix}. \tag{14}$$

The function $F(t)$ is the empirically determined counterpart to $[1-\exp(\tau)\mathrm{erfc}\sqrt{\tau}]$ of eqs (11) and (12). Since eqs (11) and (12) were the result of a solution based on linearized heat loss, $F(t)$ should be considered the result for the actual heat loss experienced with the non-linear radiative loss especially. It has been surprising but fortuitous that the simple functional form of eq (14) has been satisfactory in many varied and complex materials. As t or $\tau \to \infty$, $1-\exp(\tau)\mathrm{erfc}\sqrt{\tau}$ approaches 1 so that t^* in $F(t)$ can be regarded as a time to reach equilibrium or steady state in the material. Also as t or $\tau \to 0$, $1-\exp(\tau)\mathrm{erfc}\sqrt{\tau}$ approaches $2h\sqrt{t}/\sqrt{\pi k\rho c}$. Hence since $F(t)$ follows this behavior for $t \leqslant t^*$, it follows that

$$b = \frac{2h}{\sqrt{\pi k\rho c}}. \tag{15}$$

Thus, $k\rho c$ can be derived. The ignition data analysis yields the two effective properties, $k\rho c$ and T_{ig}, for a material. These should be applicable for both ignition and flame spread.

Some examples of results [3] are shown in figures 3a and 3b. These results were obtained in a vertical orientation in a device for which h_c was determined to be 15 W/m^2-K under conditions of natural convection [2,3]. From eq (13) the derived ignition temperature for the polycarbonate sample (fig. 3a) was found to be 528 °C and for the carpet of figure 3b a value of 412 °C was determined. Of course, accuracy cannot be assured to three significant figures. Our experience has ranged from values as low as 280 °C for a form of polymethylmethacrylate (PMMA) to 620 °C for a fire retarded plywood. Most materials seem to fall in a range of 350 to 450 °C. Comparison with measured values of surface temperature have been done on a limited basis with encouraging results. The measurement technique used has been described by Atreya et al. [4]. Figure 4 shows results for ignition in a vertical orientation for Douglas fir particle board. This illustrates typical results under direct flame heating ($\dot{Q}_b'$) from a line burner diffusion flame at the base of the sample as well as by radiant heating with a pilot flame.

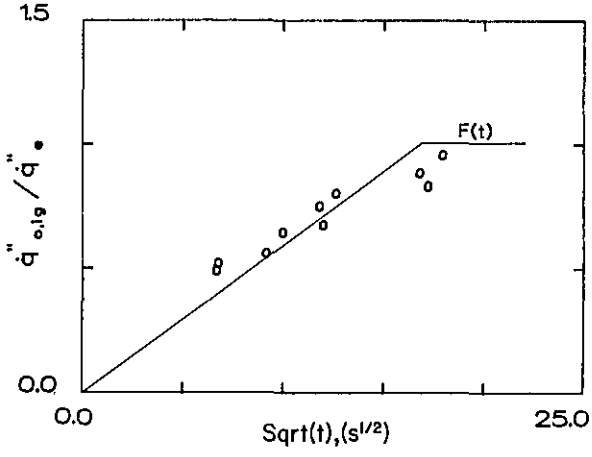

Figure 3a. Pilot ignition results under radiative heating—polycarbonate, $\dot{q}_{0,ig}'' = 3.0$ W/cm^2.

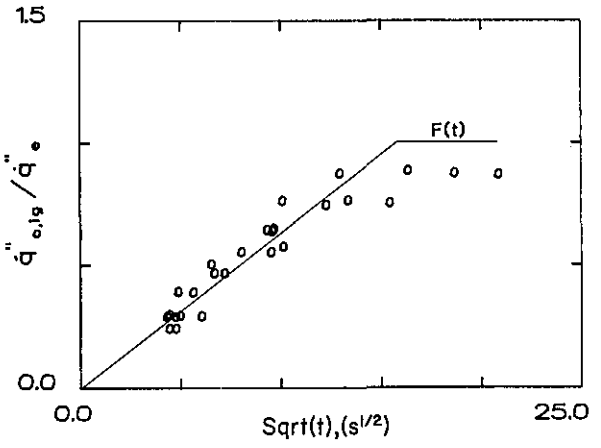

Figure 3b. Pilot ignition results under radiative heating—carpet, $\dot{q}''_{0,ig} = 1.8$ W/cm^2.

Table 1. Comparison of measured and derived ignition temperatures under radiative heating

Material	Radiative heating (W/cm^2)	Measured, T_{ig} (°C)	Derived, T_{ig} (°C)
Particle board	2.0–6.3	290–380	382
PMMA	1.6–4.6	285–330	378

The corresponding derived values for $k\rho c$ compared to values found in the literature at normal atmospheric temperatures (20–25 °C) tend to be always higher. This is shown in table 2 for the same materials.

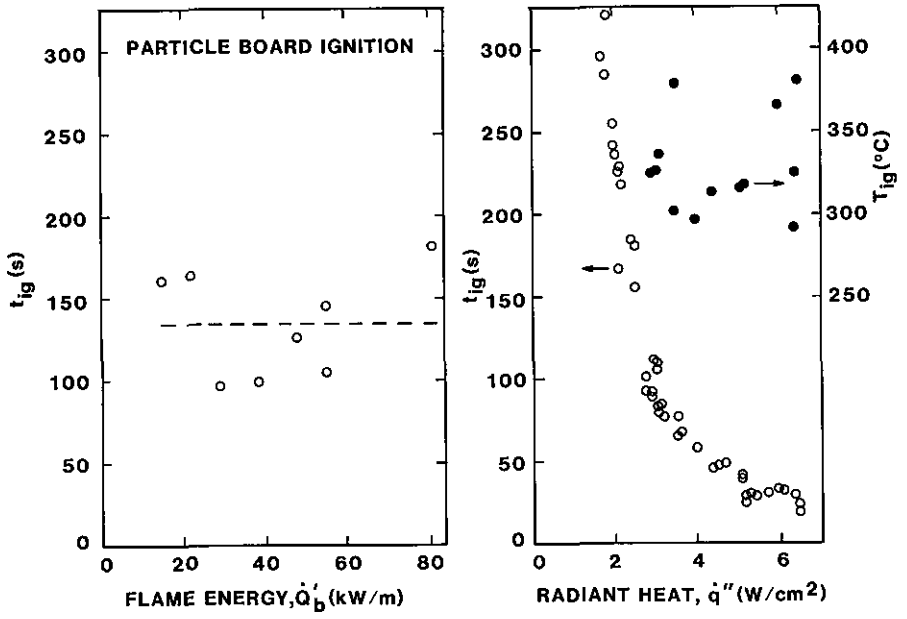

Figure 4. Flame and piloted radiative ignition of Douglas fir particle board in a vertical orientation.

It should be mentioned that the wood shown here and all other samples were tested under laboratory temperature and humidity that remained fairly constant at 20 °C and 50% RH so that changes in results due to wide variations in moisture content have been minimized. Table 1 summarizes how these measured T_{ig} values compare with the inferred T_{ig} as derived from $\dot{q}''_{0,ig}$ and eq (13). In figure 4 the surface temperatures measured at a fixed radiant heat flux have been plotted. Results are also shown for PMMA determined similarly.

Table 2. Comparison of derived and literature values of $k\rho c$

Material	Derived value (kW/m^{2}K)^{2}s	Literature value (25 °C) (kW/m^{2}K)^{2}s
PMMA	1.02	0.66
Particle board	0.93	0.14

These results might be explained in terms of $k\rho c$ increasing with temperature and by overestimating the T_{ig} with then influences h in eq (15). These variations in $k\rho c$ and T_{ig} should be considered acceptable for assessing ignition and subsequently flame spread when the empirical procedure is compared to the difficulty of measuring T_{ig} directly especially for complex materials.

Opposed Flow Flame Spread

Many investigators have studied the theoretical and fundamental aspects of flame spread on a surface in a direction opposite to a directed flow of the environment [5–10]. This is generally referred to as opposed flow flame spread. The opposed flow may be induced by the spreading flame itself due to buoyancy effects. This would be the case for downward or lateral spread on a wall or horizontal axisymmetric spread on a floor. The natural convection velocities should not vary greatly for small fire conditions and for typical flame temperatures can be estimated at O(10) cm/s [6].

The solution derived by deRis [6] under steady conditions with consideration of the gas phase and solid fuel phase in two dimensions can be given as

$$V_p = V_g \frac{(k\rho c)_g}{k\rho c}\left(\frac{T_f - T_{ig}}{T_{ig} - T_s}\right)^2. \tag{16}$$

Here V_g is the opposed flow velocity, T_f is the flame temperature, and the subscript g denotes properties of the gas phase. Recently Wichman [10] has developed an alternative model which has included effects of finite kinetics in the gas phase. This analysis changes the exponent in eq (16) from 2 to 2.5 and primarily modifies the value of V_p by a function of a Damköhler number which brings into play needed kinetic data for the fuel. Roughly, if chemical kinetic effects are unimportant then eq (16) is adequate, but if kinetics are important then the actual flame spread speed is lower than that given by eq (16). These results have been shown experimentally for thick (PMMA) and thin (paper) fuels over a wide range of flows (V_g), gravitational fields, and oxygen concentrations [5,7,9,10].

The problem with applying eq (16) in general is the ability to determine the flame temperature for a complex material experiencing opposed flow flame spread. In comparing eq (16) with eq (10) we see that the numerator suggests another "property" that could be sought for specific conditions of opposed flow spread. Here we consider lateral flame spread on a wall in the apparatus illustrated in figure 2 [1–3]. By applying a variable decreasing external radiant heat flux with distance from the ignitor, the flame will spread according to the local surface temperature (T_s). The data can ultimately be correlated by the relationship:

$$V_p = \frac{\Phi}{k\rho c (T_{ig} - T_s)^2}, \tag{17}$$

where Φ is now a new material flame spread "property." It should be a constant for a particular material under conditions of a fixed V_g and a fixed ambient oxygen concentration. Thus under natural convection conditions in air we developed values for Φ [2,3]. The results for lateral spread were also found in agreement for downward spread and horizontal axisymmetric spread [4] indicating the opposed flow velocities were similar. This suggests that Φ values derived under lateral spread could also apply to downward (provided melting is not significant) or horizontal spread under natural convection conditions.

If one accepts eq (16) as correct where T_f is the actual flame temperature, then this value of T_f can be computed from the data for Φ. For the orientation of lateral spread apparatus if can be argued that natural convection prevails and V_g is weakly dependent on material through T_f. Selecting $T_f = 2080$ °C for purposes of estimating V_g, gives 0.11 m/s [3,6]. Therefore, from eqs (16) and (17)

$$T_f = T_{ig} + \left(\frac{\Phi}{V_g (k\rho c)_g}\right)^{1/2}. \tag{18}$$

In order to estimate T_f, $(k\rho c)_g$ is taken for air at normal temperature to be 3.3×10^{-5} $(kW/m^2\text{-}K)^2 s$, and V_g is taken as 0.11 m/s for natural convection conditions.

The procedure for determining Φ requires several steps. Equation (17) can be rewritten making use of eqs (11)-(15). This results in

$$V_p(t)^{-1/2} = \left(\frac{h^2 \Phi}{k\rho c}\right)^{-1/2} [\dot{q}''_{0,ig} - \dot{q}''_e F(t)]. \tag{19}$$

Here t refers to the time the pyrolysis front is at a position x and is the time over which $\dot{q}''_e$ has acted at that same position. The empirically derived results from ignition, $F(t)$, allows us to account for the varying surface temperature over distance x and time t. This technique has been successful in correlating a wide range of materials over a heat flux range of 0.2 to 5 W/cm^2 with a wide range of heating times as well [3]. Some illustrative results are shown in figures 5a and 5b. The velocity was determined by analyzing the record of pyrolysis

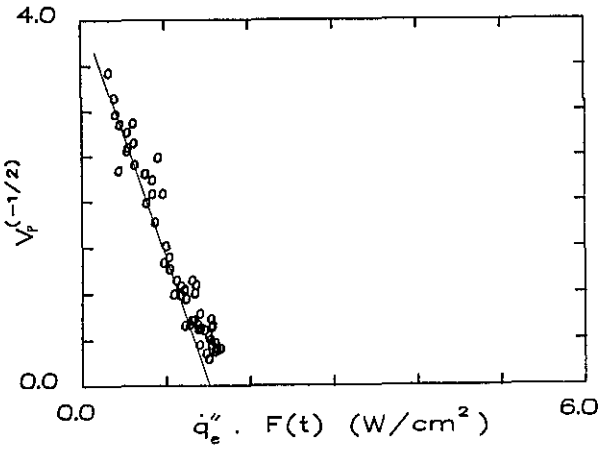

Figure 5a. Correlations of lateral flame spread—asphalt shingle.

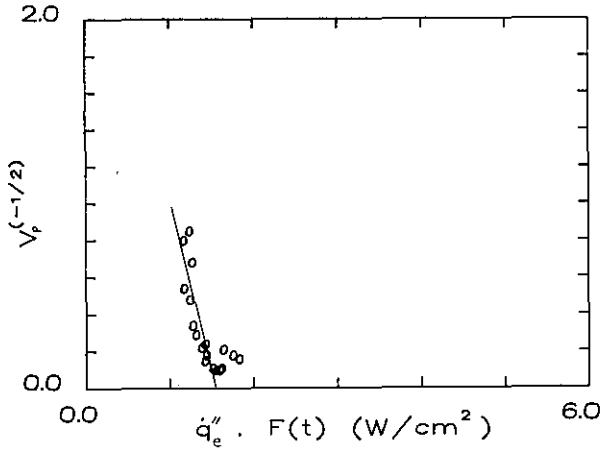

Figure 5b. Correlations of lateral flame spread—wool carpet #2 (untreated).

front as a function of time. The lines have been drawn by weighing the data points over the center of the data. This is done for two reasons. V_p is not accurately determined as $\dot{q}_e''F(t)$ approaches the intercept $\dot{q}_{0,ig}''$; and at the other extreme, extinction effects tend to cause some scatter and curvature in the results. It is interesting to note that this correlation provides a way to determine $\dot{q}_{0,ig}''$ independent of the ignition procedure of bracketing. Results for these two materials are summarized in table 3. Generally results for Φ have ranged from approximately 1 to 15 $(kW)^2/m^3$ whereas a value of $O(10)(kW)^2/m^3$ could be estimated from eq (16) using a theoretical flame temperature and a characteristic velocity for natural convection of approximately 10 cm/s. Also shown in table 3 are minimum temperatures for spread ($T_{s,min}$) below which no propagation is observed. This cannot be explained theoretically, but must be governed by heat losses and chemical kinetic effects as the surface temperature decreases. The flame spread correlations of figures 5a and 5b show this lower limit for $\dot{q}_e''F(t)$ from which a corresponding temperature can be computed from eqs (11) and (14), i.e.

$$T_{s,min} - T_\infty = \frac{1}{h}[\dot{q}_e''F(t)]_{\text{lower limit}}, \tag{20}$$

and where h is evaluated at $T_{s,min}$ by eq (13). Values of $T_{s,min}$ range widely. For example, PMMA will allow lateral spread for normal ambient temperatures, while for Douglas fir particle board $T_{s,min}=275$ °C, and for a fire retarded plywood $T_{s,min}=T_{ig}=620$ °C so that no lateral flame spread was found to be possible.

Table 3. Illustrative results for lateral flame spread

Material	$\dot{q}_{0,ig}''$ (ignition data) W/cm²	T_{ig} °C	$\dot{q}_{0,ig}''$ (spread data) W/cm²	Φ $(kW)^2/m^3$	T_f °C	$T_{s,min}$ °C
Asphalt shingle	1.5	378	1.6	5.4	1590	140
Wool carpet #2 (untreated)	2.0	435	1.6	7.3	1850	335
Wool carpet #2 (treated)	2.2	455	1.6	0.89	950	365
PMMA (G)	1.5	378	1.6	14.4	2370	<90

It is interesting to examine the flame temperature values computed from eq (18). These must be interpreted as not precise flame temperature values, but as approximate indications of the effective flame temperature. The treated wool carpet compared to the untreated version in table 3 suggests that the biggest impact of the "treatment" is in the gas phase on T_f since the ignition temperature and other properties are not essentially affected. Thus, the test data offer the potential for discerning between gas-phase and solid-phase reductions in flame spread mechanisms for a given material and its additives. This is speculative, but perhaps worthy of further study.

Upward Flame Spread

Upward flame spread is a particular form of wind-aided flame spread in which the flow veloc-

ity in the direction of flame spread is induced by the buoyancy effect of the flame itself. Limited results exist for upward flame spread. Generally, it is found that V_p is proportional to $(x_p - x_b)^n$ where n tends to vary from 0.5 to 1. Furthermore the burnout front (x_b) must also be determined. Some examples in the literature give $n=0.5$ to 0.7 for turbulent conditions over thin textile materials [11], $n=3/4$ for the thin case and $n=1/2$ for the thick fuel case both under laminar conditions [12], and for thick PMMA under turbulent conditions n was approximately equal to 1 [13].

The theoretical model given by eq (10) has been developed by an alternative analysis by Sibulkin and Kim [14] and has been employed in some recent studies [15–17]. This result lends itself to application to materials particularly if we accept the results already determined for $k\rho c$ and T_{ig}. Hence we need to seek relationships for $\dot{q}_f''$ and $x_f - x_p$ in terms of material properties. Some progress has been made in this respect.

The flame heights x_f have been measured for line diffusion flames of methane and for irradiated wall mounted materials contiguous to a vertical wall. These wall flame heights have been shown under normal ambient air conditions to only depend on the energy release rate per unit wall width for the particular fuel ($\dot{Q}_b'$) [15,17,18]. The results developed by Delichatsios [18] for turbulent conditions is given below:

$$x_f = 4.65\left(\frac{\dot{Q}_b'}{C_p T_\infty \rho_\infty \sqrt{g}}\right)^{2/3}, \tag{21}$$

where c_p, T_∞, ρ_∞ are for normal air and g is the acceleration due to gravity. All of the fuel chemical properties are contained in $\dot{Q}_b'$. In general, under spreading conditions where burnout is occurring, x_f in eq (21) should be replaced by $x_f - x_b$. For $(x_f - x_b) < 10$ cm the flow is likely to be laminar and eq (21) will not apply, but clearly it will be most applicable to realistic conditions except at incipient spread.

For conditions of constant flame heating $\dot{q}_f''$ over x_p to x_f and zero for $x > x_f$, we can write

$$V_p = \frac{x_f - x_p}{t_f}, \tag{22}$$

where $t_f = \dfrac{\pi\, k\rho c (T_{ig} - T_s)^2}{4(\dot{q}_f'')^2}$

is a characteristic flame spread time. It was shown by Saito et al. [16] that the application of a modified eq (21) with eq (22) leads to an accelerating result for x_p provided

$$t_f < \frac{\pi (K \dot{Q}_b'')^2}{4} t_b, \tag{23}$$

where $x_f - x_b = K\dot{Q}_b'$ is the linear form of eq (21) and t_b is a characteristic burning time associated with a nominal average energy release rate per unit area $\dot{Q}_b'$ taken as constant over this time. Hence if the energy release rate per unit area is too small or the burning time is too small, eq (23) will not be satisfied and the spread will instead decelerate and terminate. This behavior is independent of the ignition source that got the process started. Although $\dot{Q}_b'$ cannot be regarded as properties, such data are available for at least small samples in combustion calorimeters under conditions of external heating [19]. It is well known that most thermally thick materials will not burn in air unless they receive heat from an external source, e.g., radiant panel. In addition, upward spread will not occur and be sustained (accelerate) unless t_f satisfies a relationship of the form of eq (23) which depends directly on t_b and $\dot{Q}_b''$.

Let us now examine the quantity t_f. Presuming we have developed the properties $k\rho c$ and T_{ig}, we now need to know $\dot{q}_f''$. From figure 4, the flaming ignition in comparison with the pure radiative ignition suggests a level of the flame heat flux to be equivalent to roughly 2 to 3 W/cm^2. This appears to be independent of the size of the wall flame at least from 20 to 80 kW/m. Indeed this has been the case for wall flames measured for line fuel sources of methane and propane [17,20], a wide variety of materials 0.3 m high irradiated from 1.5 to 3.7 W/cm^2 [15], and liquid fuel soaked wicks [21]. All of these tend to suggest a universal result independent of the fuel in a plot of $\dot{q}_f''$ with x/x_f. A compilation of these results is shown in figure 6. This is the flux above the pyrolysis zone for a burning material. It is striking that the flux in the flame region can be estimated as 2.5 ± 0.5 W/cm^2 and falls rapidly at $x > x_f$.

These data apply for $0.3 \leqslant x_f \leqslant 1.4$ m. We expect for larger flame heights or very sooty fuels that flame radiation effects may distort these results. However over the range of conditions tested it appears that some compensation of radiation and convection is being accommodated to make $\dot{q}_f''$ nearly constant over the flame region. It is interesting to note that the flame heat transfer in the pyrolysis region of a 3.56 m high PMMA wall fire leads to a heat flux of as high as 4.4 W/cm^2 [22]. Whereas a laminar flame could yield a maximum of 5 W/cm^2

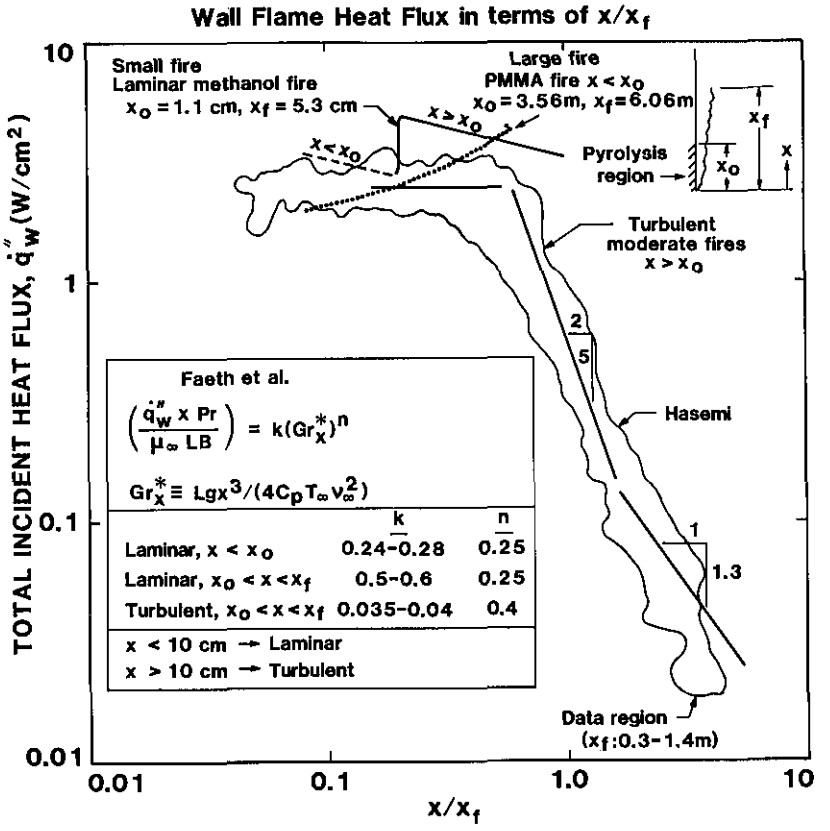

Figure 6. Flame heat flux distribution for wall fires.

just outside the pyrolysis zone. (This was calculated from the work of Faeth and co-workers [21].) Hence a laminar wall flame would propagate more easily than a turbulent flame, and a large flame would enhance propagation due to an increase in flame radiation

It is interesting to examine the characteristics of two materials: PMMA and particle board as described in tables 1 and 2. Let us assume that the flame heat flux in the pyrolysis wall region is the same as the value just above, namely 25 kW/m^2. Also let us consider steady burning so that the burning rate per unit area can be estimated by

$$\dot{m}''_b = \frac{\dot{q}''_f + \dot{q}''_e - \dot{q}''_{0,ig}}{L}, \tag{24}$$

where L is the heat of gasification, and the rate of energy release per unit area is

$$\dot{Q}''_b = \dot{m}''_b \, \Delta H, \tag{25}$$

where ΔH is the heat of combustion. For the case of $\dot{q}''_e = 0$ and $T_s = 20$ °C we estimate whether flame propagation is possible. This is shown in table 3 where the property values were taken from tables 1 and 2 and reference [15]. The burning times t_b were taken from our experience with the specific material examined [15]. The value K was based on a linearized flame height relationship; $K \approx 0.01$ m^2/kW for $x_f = 1$ m.

The results from table 4 suggest the wood material will not propagate while the PMMA easily leads to an accelerating flame spread. These results have been confirmed by experiments on these same materials [16]. Indeed, only by increasing T_s with external heating has led to reducing t_f and propagation for the wood [23]. Clearly this analysis has been highly approximate, and its refinement should be based on experimental results. Recent experimental results for this particle board have shown that it is possible to have flame spread under external heating conditions as low as $\dot{q}''_e = 0.42$ W/cm^2 and corresponding T_s values of roughly 100 °C. This is lower than the analysis in table 4 would suggest. But, at least, the trend and framework given by eq (22) appears valid.

Table 4. Examination of upward spread potential

Material	t_b (s)	L (kJ/g)	ΔH (kJ/g)	$\dot{Q}''_b$ (kW/m^2)	t_f (s)	$(\pi/4)(K\dot{Q}''_b)^2 t_b$ (s)
Particle board	400.	4.5	12.	23.	153.	16.
PMMA	1400.	1.8	26.	116.	161.	1468.

Conclusions

A summary of work has been presented which attempts to develop a procedure for determining property data for flame spread. The procedure appears to work for a wide variety of materials for the case of lateral flame spread on vertical walls. these effective properties are listed as follows:

1. $k\rho c$, which is a measure of the rate of temperature rise for a material;

2. T_{ig}, which is a measure of the temperature at which the material is volatized sufficiently to form a flammable mixture in air; and

3. Φ, which is a measure of the flame heat transfer under conditions of opposed flow natural convection in air.

For the case of upward flame spread on a vertical surface, some of these same properties apply. But now the flame heat transfer is a function of time which depends on the energy release rate and burning time of the material. Moreover not just the rate of upward flame spread is governed by these additional characteristics, but they also control whether spread will accelerate and be sustained. Some results have been discussed to illustrate this aspect of upward flame spread. More study is needed to generalize these results into a complete measurable set of properties for predicting upward spread.

About the author: J. G. Quintiere is a mechanical engineer and chief of the Fire Science and Engineering Division of the NBS Center for Fire Research.

References

[1] Quintiere, J. G., Fire Mater. **5**, 52 (1981).
[2] Quintiere, J. G., and Harkleroad, M., Fire Safety Science and Engineering, ed. by Harmathy, T. Z., pp. 239–267, Amer. Society for Testing and Materials, ASTM STP 882 (1985).
[3] Quintiere, J. G., and Harkleroad, M., New Concepts for Measuring Flame Spread Properties, Natl. Bur. Stand. (U.S.) NBSIR 84-2943 (Nov. 1984).
[4] Atreya, A., Carpenter, C., and Harkleroad, M., Effect of Sample Orientation on Piloted Ignition and Flame Spread. Int. Assoc. for Fire Safety Science. Fire Safety Science Proceedings. 1st Int. Symposium. October 7–11, 1985. Grant, C. E., and Pagni, P. J., Editors, Gaithersburg, MD, Hemisphere Publishing Corp., NY, 97 (1985).
[5] Fernandez-Pello, A. C., and Hirano, T., Combust. Sci. Technol. **32**, 1 (1983).
[6] deRis, J. N., 12th Symp. (Int.) on Combustion, The Combustion Institute, Pittsburgh, PA, 241 (1969).
[7] Altenkirch, R. A., Eichhorn, R., and Shang, P. C., Combust. Flame **37**, 71 (1980).
[8] Magee, R. S., and McAlevy, R. F., III, J. Fire Flammability **2**, 271 (1971).
[9] Fernandez-Pello, A. C., Ray, S. R., and Glassman, I., 18th Symp. (Int.) on Combustion, The Combustion Institute, Pittsburgh, PA, 579 (1981).
[10] Wichman, I. S., Combust. Sci. Technol. **40**, 223 (1984).
[11] Markstein, G. H., and deRis, J., 14th Symp. (Int.) on Combustion, The Combustion Institute, Pittsburgh, PA, 1085 (1973).
[12] Fernandez-Pello, A. C., Combust. Flame **31**, 135 (1978).
[13] Orloff, L., deRis, J., and Markstein, G. H., 15th Symp. (Int.) on Combustion, The Combustion Institute, Pittsburgh, PA, 183 (1975).
[14] Sibulkin, M., and Kim, J., Combust. Sci. Technol. **17**, 39 (1977).
[15] Quintiere, J., Harkleroad, M., and Hasemi, Y., Combust. Sci. Technol. **48**, 191 (1986).
[16] Saito, K., Quintiere, J., and Williams, F. A., Upward Turbulent Flame Spread. Int. Assoc. for Fire Safety Science. Fire Safety Science Proceedings. 1st Int. Symposium. October 7–11, 1985. Grant, C. E., and Pagni, P. J., Editors, Gaithersburg, MD, Hemisphere Publishing Corp., NY, 75 (1985).
[17] Hasemi, Y., Thermal Modeling of Upward Wall Flame Spread, 1st Int. Symposium. October 7–11, 1985. Grant, C. E., and Pagni, P. J., Editors, Gaithersburg, MD, Hemisphere Publishing Corp., NY, 87 (1985).
[18] Delichatsios, M. A., Flame Heights in Turbulent Wall Fires with Significant Flame Radiation. Combust. Sci. Technol. **39**, 195 (1984).
[19] Babrauskas, V., Fire Mater. **8**, 81 (1984).
[20] Kulkarni, A., Quintiere, J., and Harkleroad, M., Heat Feedback and Flame Height Measurements on Burning Vertical Surfaces. Combustion Institute/Eastern States Section. Chemical and Physical Processes in Combustion. Fall Technical Meeting, November 8–10, 1983, Providence, RI.
[21] Ahmad, T., and Faeth, G. M., 17th Symp. (Int.) on Combustion, The Combustion Institute, 1149–1160 (1979).
[22] Orloff, L., Modak, A. T., and Alpert, R. L., Sixteenth Symposium on Combustion, 1345 (1976).
[23] Saito, K., Williams, F. A., Wichman, I., and Quintiere, J., Upward Turbulent Flame Spread on Wood Under External Radiation, 1987 ASME/AIChE National Heat Transfer for Conference, Pittsburgh, PA (1987).

Volume 93, Number 1, January–February 1988
Journal of Research of the National Bureau of Standards

Conferences / Events

COMPUTER SECURITY CONFERENCE
A Report on the Tenth National Computer Security Conference, Baltimore, MD, September 21–24, 1987

The National Bureau of Standards (NBS) Institute for Computer Sciences and Technology (ICST) and Department of Defense (DOD) National Computer Security Center (NCSC) jointly sponsored the Tenth National Computer Security Conference, September 21–24, 1987. Previously this annual conference was held at the NBS. Over the last several years attendance increased dramatically, and for the first time the conference was held at the Baltimore Convention Center. Attendance exceeded 1,600, making this computer security conference the largest ever held.

About the Conference

The conference program was organized around the theme, "Computer Security – From Principles to Practices." The topics covered included research, new vendor products, technical, management, administrative, and educational aspects of computer security. Many of the papers presented at this conference addressed topics that will support the defense community, yet other issues such as ethics in computer security, privacy, risk management, contingency planning, and education were addressed and were of value to business and the civil sector of the government. Sessions addressing these topics were well attended.

There was a high interest in network security and several technical papers described the work on the Secure Data Network System (SDNS). The SDNS project was initiated last year by the National Security Agency (NSA) with the NBS, the Defense Communications Agency (DCA), and 12 communications and computer companies. Within the framework of the SDNS program, government and industry have joined to make products available that will support security services for distributed data processing networks.

The presentations were organized into two parallel tracks, one of which addressed managerial computer security issues and the other technical issues. A third track with occasional special sessions was also provided. This arrangement allowed participants a wide choice of topics from which to choose. The last day of the conference provided an opportunity for attendees to organize and participate in special interest groups.

For the first time, a unique "Poster Session" was offered. This session provided an opportunity for participants to speak for 2 minutes on any computer security related subject. Many speakers participated enthusiastically. As a result, the poster session will be included in next year's program.

Speakers represented computer industry leaders, computer security practitioners, and researchers from the United States and abroad. Brief summaries of a few specific contributions follow.

Opening the Conference

ICST Director James Burrows and NCSC Director Patrick Gallagher welcomed the conference participants. In his talk Burrows stressed the

improving network security as use of networks grows. Burrows spoke of how ICST initiated a program in the late 1970s to meet user needs to interconnect different manufacturers' equipment and systems in distributed data processing networks. The Open Systems Interconnection (OSI) standards development has been carried out by national and international committees with ICST assistance. Burrows further stated that the NBS Workshop for Implementors of OSI was organized in 1983 to start a cooperative effort with industry to build compatible commercial products. Burrows stressed that the improved connectivity brought about by OSI must be accompanied by essential protective measures. He encouraged industry and government to identify their requirements for protocols that will support security services in open systems. Burrows stated that NBS will continue its work with NSA to assure compatibility and proper performance of protocols.

Gallagher also discussed the importance of network security. He announced a recent publication produced by the NCSC, "Trusted Network Interpretation." This document, referred to as the "Red Book," was developed to provide a standard to manufacturers and users on the security features and assurance levels that are needed in commercial network products. Gallagher further discussed how the NCSC works closely with U.S. computer manufacturers encouraging the building of "trust" into the hardware and software of computer systems. He further stated that the "Orange Book" (formally, *Trusted Computer System Evaluation Criteria)*, which established a set of basic requirements and evaluation classes for assessing the effectiveness of security controls built into computer systems, continues to be the cornerstone for the Center's evaluation program. Gallagher called for continued cooperative efforts of the government, industry, and academe to build trust into computer systems.

The keynote speaker was U.S. Representative Dave McCurdy (D-Oklahoma). Rep. McCurdy chairs the House Subcommittee on Transportation, Aviation and Materials, which has jurisdiction for communications research and development. It is from this basis, McCurdy explained, that the Subcommittee began an in-depth examination of the issues in computer and communications security and privacy within the Federal government. Hearings before the Transportation Subcommittee revealed that computer security in the Federal government needed improvement. This led to the introduction of legislation that became known as HR 145, The Computer Security Act of 1987. McCurdy explained that the bill starts not only from the premise that computer security in the Federal government needs improvement but that it can benefit from stronger centralized leadership. The bill assigns responsibility for protecting unclassified government computer information to NBS and the protection of classified information to the NSA. Rep. McCurdy reported that HR 145 passed the House and the next step is consideration by the Senate. He called on industry and Federal agencies to continue building on technology to strengthen computer security in the government. He emphasized that the technical capabilities and assistance of both the NCSC and NBS are essential to meeting national computer security goals.

Network Security

Dennis Branstad, NBS Computer Science Fellow, presented a tutorial on the Open Systems Interconnection (OSI) computer network architecture. Branstad explained that the security services being developed for OSI will assure that data being transmitted from one OSI system to another will be protected against modification, disclosure, replay, and undetected loss. He described the seven-layered OSI communications model connecting hosts in star configurations, LANs and LAN bridges, ring configurations, and gateways. Cryptographic procedures were also discussed.

Several technical papers highlighted the work on the SDNS project. This project, as presented by Gary Tater, NCSC, focuses on designing the next generation of secure computer communications network and product specifications to be implemented for applications utilizing both public and private data networks. Tater explained that one of the primary goals of the program is to assist and encourage industry in developing a wide variety of cost-effective communications products and systems that meet OSI standards. Tater reported that the project is advancing well and predicted it would result in data security protocols and products by 1990.

Insider Threat

A panel addressed the issue of "insider threats." Allan Clyde, a Washington businessman, explained that managing the risks arising from insiders on sensitive computer systems is growing in importance.

Clyde reviewed the work being done in the field and proposed a system of analysis to identify suspicious events. This method would perform continuous capture and encryption of all keystrokes for each user. Clyde concluded that full-system surveillance can be achieved cost-effectively with high performance products that do not represent an excessive burden to the system.

James Anderson, a computer security consultant, contends that surveillance is not effective since a user with a high degree of expertise can operate below the surveillance level. He asserted that systems certified at the B2 and B3 levels circumvented the need for surveillance. Another panelist, Priscilla Regan, U.S. Congress Office of Technology Assessment, stated that surveillance could mean an invasion of privacy. She proposed that deterrence mechanisms be used instead of surveillance and that if used, surveillance not be concealed. This panel discussion clearly demonstrated there are no perfect solutions to the insider threat problem.

Computer Viruses

In addition to the insider threat problem, potential solutions to other kinds of threats were discussed. Howard Israel, NCSC, theorized that any protection mechanism used to detect a Trojan Horse threat will work to detect a computer virus as well. Israel pointed out that a virus attack generally causes more damage than a Trojan Horse because more computers or more computer programs are involved in a virus attack. During this presentation, Israel reviewed several virus research activities. He concluded that a well-defined security policy used in conjunction with trusted software can provide reasonable protection against virus and Trojan Horse attacks.

Risk Assessment

Robin Moses, UK Central Computer and Telecommunications Agency (CCTA), and Rodney Clark, BIS Applied Systems LTD, jointly presented a risk analysis methodology, called CRAMM, developed for use in the United Kingdom. CRAMM is designed for the novice risk analyst and combines a baseline "code of good management practices" with a qualitative risk analysis method. CRAMM is threat oriented and emphasizes consequential as well as direct losses. A questionnaire with scales of 1–10 is used to evaluate the vulnerabilities and risks in the system.

Sylvan Pinsky, Senior Scientist for the Office of Research and Development, NCSC, discussed current efforts by the Federal government in the area of computer risk management. Pinsky announced the cooperative efforts of NBS and NCSC in establishing a Risk Management Laboratory. Pinsky highlighted that the primary goal of the laboratory will be to conduct research in risk management techniques and methodologies and to transfer the results of that research to government and private sector organizations. Another related activity being considered is to assist agencies in the selection and use of commercial risk management software. The laboratory, which will be located at NBS, may also provide a clearinghouse for information on risk analysis and management for the Federal government.

Contingency Planning

A special session on contingency planning provided lively discussions on developing computer contingency plans. Ray Pardo, Bechtel Eastern Power Corporation, presented a "fast track" approach (6 months to a year) for implementing a contingency plan. Fast track, as described by Pardo, is targeted toward developing a workable and tested contingency plan for truly critical applications and for a specific range of contingencies. Pardo discussed the advantages of the fast track approach and outlined a method for implementing the plan. Pardo emphasized that unlike other contingency planning methodologies where the benefits of the plan are delayed for 1 to 2 years, "fast track" quickly reaches the crucial testing phase.

Thomas Judd, Federal Reserve System Contingency Processing Center, discussed innovative strategies for returning to "business as usual" for those critical organizations that affect the entire society, i.e., utilities, securities firms, and military command and control. Judd suggested that contingency planning be extended beyond the "cook book" approach. His fundamental belief is that the ability to return to normalcy lies in the commitment of senior management, and that the planning, testing, and training remain dynamic to the degree that it matches the changing business environment.

Training and Awareness

Several papers addressed the importance of computer security training and awareness. Elizabeth Markey, U.S. Department of State, described the approach her organization has taken to train their personnel to counter risks that threaten the organization's computer systems. Markey explained that a series of carefully structured systems security seminars and briefings are held for all levels of personnel, including managers, line security personnel, and users. Markey described a 2-hour briefing that is presented to Executive Directors; a 4-day seminar for Regional Security Officers; and a 1- to 2-hour briefing for all new employees.

Eliot Sohmer, NCSC, described the computer security curriculum being developed there. The course is modular and addresses both non-technical and technical issues. Not unlike the training and awareness program developed by Department of State, NCSC's training plan is designed to meet the needs of various categories of personnel ranging from product evaluators to research and development specialists to clerical and administrative assistants. It is planned that each training module will be videotaped and will be available to other government agencies, universities, and vendors.

DOD Computer Security Research and Development Programs

A panel summarized the progress and plans for research and development in the Federal government in the areas of secure architectures, data base management systems (DBMS), networks, modeling and verification, and aids to evaluation.

Data Base Management Security

A joint paper "Data Integrity vs Data Security," by Rhonda Henning and Swen Walker, NCSC, summarized past and current thoughts on these two subjects. Henning pointed out that the presence of a trusted operating system does not guarantee that the DBMS can be used to share information in a trusted way. She stated that the integrity concerns were not sufficiently addressed by conventional secrecy policies. Henning reviewed several integrity policy alternatives concluding that few have actually proven successful in operational environments. She recommended that each application be examined to determine which integrity policy best fits its requirements. Henning further suggested that a combination of integrity policies may be more appropriate.

Social Issues and Ethics

Two papers addressed social issues and ethics in computer security. Dorothy Denning presented a joint paper she wrote with Peter Neumann and Donn Parker, SRI International. Denning examined the social aspects of computer security with respect to the computerized monitoring technologies being developed. She spoke of how many users respond negatively to computer security because they view it as interfering with their productivity and in some cases a violation of their rights. She said these problems stem from a misalignment of the concerns and values of management with those of their employees on the effects of security policies and mechanisms. She believes that the use of security surveillance of computer users could increase this misalignment. Denning recommended that threat monitoring techniques be carefully applied to preserve the rights of privacy and freedom from intrusion and should avoid creating an atmosphere that leads to employee suspicion and dissatisfaction. She further stated that while monitoring user's activities is necessary for accountability and detection of irregularities, threat monitoring must be done with informed consent. Denning also suggested that organizations align their security policies with computer users outside the organization. She suggested setting up a computer system somewhere in the world which offered programming games with prizes and recognition of winners. The purpose is to provide more healthy outlets for the non-malicious hacker. Denning concluded that it is vital that the technological and social considerations be balanced so that serious problems may be avoided.

Marlene Campbell, Murray State University, discussed the need to bring ethics into the classroom and the workplace. Campbell emphasized the need to train our young people in the ethics of protecting our computer systems. She illustrated through several examples that a lack of ethics is a cause of computer crime. Campbell concluded that while security mechanisms and laws are provided to temper the activities of computer users, the truly binding controls rest with the professional ethics of each user.

Hacker Problem

Ken McLeod, a former Arizona sheriff who was involved in numerous computer fraud cases and is now a consultant on computer crime issues, provided a dramatic finale to the conference. McLeod presented videos of criminal interrogations and a "hacker" at work. His presentation provided a vivid understanding of the malicious hacker problem.

For More Information

Proceedings from this conference are available upon request. You may write or call Irene Isaac, NBS, ICST, Building 225, Room B266, Gaithersburg, MD 20899; (301) 975-3360.

The following documents may be ordered from the NCSC:

1. *Proceedings, 10th National Computer Security Conference*, 21–24 September 1987.
2. *Department of Defense Trusted Computer System Evaluation Criteria*, DOD 5200.28-STD, December 1985.
3. *Trusted Network Interpretation of the Trusted Computer System Evaluation Criteria*, NCSC-TG-005, Version 1, 31 July 1987.

Irene E. Isaac
Institute for Computer Sciences and Technology
National Bureau of Standards
Gaithersburg, MD 20899

Calendar

April 10–15, 1988
RESONANCE IONIZATION SPECTROSCOPY AND ITS APPLICATIONS (RIS '88)

Location: National Bureau of Standards
Gaithersburg, MD

The RIS '88 Symposium is a major focal point for presenting the results of multidisciplinary research involving resonance ionization phenomena and related laser applications. The program will consist of posters, contributed and invited papers, and plenary lectures on the following topics: (1) Photophysics and Spectroscopy, (2) Resonance Ionization Mass Spectrometry (RIMS), (3) Molecular Resonance Ionization Spectroscopy, (4) Noble Gas Atom Counting, (5) Analysis of Materials and Surfaces, (6) Medical and Environmental Application, (7) Optical Sources, (8) Atom Reservoirs and Sampling, (9) Physics Applications—including Elementary Particles and Nuclear Processes, (10) Chemical Applications—including Diffusion, Reaction Rates, and Clustering.

This Symposium is organized by an International Advisory Group through an appointed Program Committee and is sponsored by the Department of Energy, the University of Tennessee, the National Bureau of Standards, the International Union of Pure and Applied Physics, EG&G, and Battelle Northwest Laboratories.

Contact: Thomas B. Lucatorto, A243 Physics Building, National Bureau of Standards, Gaithersburg, MD 20899, 301/975-3734.

April 13–15, 1988
4th INTERNATIONAL CONFERENCE ON METROLOGY AND PROPERTIES OF ENGINEERING SURFACES

Location: National Bureau of Standards
Gaithersburg, MD

Metrology and properties of engineering surfaces have continued to assume great importance to both the practicing engineer and the researcher. In recent years, industry has gained increased awareness of the importance of surface preparation techniques. This international conference is the 4th in a series of meetings on the subject of metrology and properties of engineering surfaces which have been held every 3 years since 1976. The main topics to be discussed at this meeting will be: the application of new surface techniques in industry, the development of new tactile instruments, the development of new techniques for the optical measurement of engineering surfaces, the compilation and analysis of data for specific manufacturing processes, and the relationships between surface generation and practical performance. This conference is sponsored by the National Bureau of Standards, Coventry Polytechnic, and Whitestone Business Communications.

Contact: Professor K. J. Stout, Coventry Polytechnic, Department of Manufacturing Systems, Priory Street, Conventry CV1 5FB, England, 0203 24166, ext. 278; or Dr. T. V. Vorburger, A117 Metrology Building, National Bureau of Standards, Gaithersburg, MD 20899, 301/975-3493.

April 21–22, 1988
WORKSHOP ON MICROSTRUCTURE AND MACROMOLECULAR RESEARCH WITH COLD NEUTRONS

Location: National Bureau of Standards
Gaithersburg, MD

In order to inform and involve the community of scientific researchers at an early stage in the development of the Cold Neutron Research Facility (CNRF), NBS is hosting a series of workshops which will each focus on a major area of cold neutron research. This workshop on "Microstructure and Macromolecular Research with Cold Neutrons" will focus on scientific opportunities in the study of submicron structures in materials, including macromolecular structures in polymers and biomaterials, which arise from experimental techniques which take special advantage of cold neutron.

Technical talks by invited speakers will review current work in a variety of disciplines and discuss future extensions utilizing cold neutrons. Specific instruments and techniques related to characterizing submicron structures in materials will also be discussed. An important part of the workshop will be the active participation of the attendees in assessing the capabilities of and the need for various types of instrumentation for the CNRF. The work-

shop will thus afford potential users a unique opportunity to explore the capabilities of the CNRF and to guide its development.

The meeting is sponsored by the National Bureau of Standards.

Contact: Charles J. Glinka, B106 Reactor Building, National Bureau of Standards, Gaithersburg, MD 20899, 301/975-6242.

June 20–23, 1988

10th SYMPOSIUM ON THERMOPHYSICAL PROPERTIES

Location: National Bureau of Standards
Gaithersburg, MD

A Call for Papers has been issued for this symposium, the 10th in a well-established series of conferences on thermophysical properties. The symposium is concerned with theoretical, experimental, and applied aspects of thermophysical properties for gases, liquids, and solids. Appropriate topics to be included in the symposium include Thermodynamic Properties, Transport Properties, and Data Correlation. Special topics to be included in the symposium are Properties of New Materials, Properties of Gaseous and Liquid Mixtures, New Developments in Experimental Techniques, and Interpretation of Experimental Data in Terms of New Theoretical Developments. Prospective authors are requested to submit a 200–300 word abstract before December 1, 1987. The content of the abstract will be the basis for acceptance of the paper for presentation at the symposium. If the paper is accepted for presentation, then full papers should be submitted by June 23, 1988.

Contact: Dr. A. Cezairliyan, Rm. 124 Hazards Building, National Bureau of Standards, Gaithersburg, MD 20899, 301/975-5931; or Dr. J. V. Sengers, Institute for Physical Science and Technology, University of Maryland, College Park, MD 20742, 301/454-4117.